

UNIVERSITY OF CRETE
DEPARTMENT OF MATERIALS SCIENCE AND
TECHNOLOGY

**THEORETICAL STUDY OF TRANSITION–METAL
DICHALCOGENIDES AT LOW DIMENSIONS**



Daphne Davelou

Doctoral Dissertation

Heraklion, July 2019

UNIVERSITY OF CRETE
DEPARTMENT OF MATERIALS SCIENCE AND TECHNOLOGY
THEORETICAL STUDY OF TRANSITION–METAL DICHALCOGENIDES
AT LOW DIMENSIONS

PhD Candidate:
Daphne Davelou

Thesis Supervisor:
Associate Professor Ioannis N. Remediakis¹

Thesis Committee:
Associate Professor George Kioseoglou¹
Associate Professor George Kopidakis¹
Associate Professor Gerasimos Armatas¹
Associate Professor Vangelis Harmandaris²
Professor George E. Froudakis³
Professor Nikos Katsarakis⁴

¹Department of Materials Science and Technology, University of Crete

²Department of Mathematics and Applied Mathematics,
University of Crete

³Department of Chemistry, University of Crete

⁴Department of Electrical Engineering and Computer Engineering,
Hellenic Mediterranean University

Abstract

The isolation of graphene and other materials of atomic width caused intense interest in two – dimensional (2D) crystals. In the family of 2D materials, which is continuously growing, special place is held by the transition metal dichalcogenides MX_2 where $\text{M}=\text{Mo}$ or W and $\text{X}=\text{S}, \text{Se}, \text{Te}$, materials that are widely used in catalysis or as lubricants. Transition metal dichalcogenides, have been extensively studied due to the fact that they form a huge variety of structures, such as fullerenes, nanotubes, nanoribbons etc, while at the same time they present a huge field of applications from opto–electronics (for example in photovoltaics) to complex chemical reactions, such as water splitting, and biomedical applications such as drug delivery.

In this PhD thesis we study the electronic properties of quasi one – dimensional nanostructures of TMDs. We begin by studying model S structures in the tight – binding approximation, in order to obtain insight into the electronic structure of S compounds. With Density Functional Theory as implemented by the open – source grid based projector augmented wave method (GPAW), we perform ab – initio calculations for the stability and electronic properties such as the edge energy, the density of states and the bandstructure. We find that MoS_2 , MoSe_2 , WS_2 and WSe_2 nanoribbons present metallic states localized at the edges, which present a 2D band gap crossing, similar to topological insulators. From the wavefunctions at the edge we examine the physics of the metallic states according to Shockley theory and we find that the broken periodicity due to the edge formation is responsible for the electron localization.

Finally, with the introduction of defects such as oxygen atoms and hydroxyl radicals in our structures, we study a more realistic behavior of our materials when they interact with atmosphere and we find that the electronic properties of 1D TMDs are robust against environmental conditions, as opposed to the 2D semiconducting energy gap which undergoes a red shift.

Acknowledgments

First, I would like to express my gratitude to my supervisor Assoc. Prof. Ioannis N. Remediakis, who presented me with opportunity to go further, obtain new knowledge and in this road towards the finish line, whenever I hit a bump, he was always there to help me push forward. Also, I would like to thank my advisors in this PhD thesis Assoc. Prof. George Kopidakis and Assoc. Prof. George Kioseoglou who have been by my side since my first steps as a scientific researcher and provided essential insights into my work.

I also wish to thank my thesis committee Assoc. Prof. Gerasimos Armatas, Assoc. Prof. Vangelis Harmandaris, Prof. George E. Froudakis and Prof. Nikos Katsarakis, for taking time from their tight schedules to participate and support my PhD and our collaborator Prof. Efthimios Kaxiras for the fruitful discussions and the participation in a major part of this study.

I gratefully acknowledge the funding received towards my PhD from the General Secretariat for Research and Technology (G.S.R.T.) and the Hellenic Foundation for Research and Innovation (H.F.R.I.). Finally, without the computational resources from the Cy-Tera Project, which is co-funded by the European Regional Development Fund and the Republic of Cyprus through the Research Promotion Foundation, the Bibliotheca Alexandrina and the Greek Research & Technology Network (GRNET) in the National HPC facility – ARIS, I would be able to complete such a demanding study during my PhD years.

I would like to especially thank Dr. Aristeia Maniadaki for all her support throughout these years and my colleagues with whom at some point we shared an office Antonis Raptakis, Michail Minotakis, Nikos R. Vrithias and George Vailakis and all together we managed to create some unforgettable memories. I couldn't have asked for a better working environment.

Finally, I wish to thank my parents Dora and Vasilis, who supported me in any possible way throughout my whole life, my sister Maria, who as a musician, understands nothing from my poster presentations but still insists on collecting them, my friend Stefania Liakaki-Stavropoulou who stood by my side every day and my partner Stelios Antonakis for making me laugh even on the hardest days. This work is dedicated to them.

Contents

Abbreviations.....	11
Chapter 1 - Introduction.....	13
1.1 Introduction to TMDs.....	15
1.1 Structural properties of TMDs.....	15
1.2 Physical properties and applications.....	16
Chapter 2 - Theoretical and computational methods.....	21
2.1 Schrödinger equation	23
2.1.1 Born – Oppenheimer approximation.....	23
2.2 Density Functional Theory (DFT).....	24
2.2.1 Generalized – Gradient approximation (GGA).....	25
2.2.2 DFT code.....	25
2.3 Tight binding approximation (TBA).....	27
2.3.1 Introduction.....	27
2.3.2 Tight - binding approximation in a periodic infinite chain	27
2.3.3 Tight - binding approximation in hexagonal solid sulfur - A non-periodic structure.....	30
2.3.4 Tight-binding code.....	32
Chapter 3 - Simulations of model S structures.....	33
3.1 Introduction.....	35
3.2 Infinite linear chain.....	35
3.3 DFT and TBA in various finite structures.....	37
3.4 Conclusion	40
Chapter 4 - Electronic properties of TMD nanoribbons.....	43
4.1 Introduction.....	45
4.2 Computational Methodology.....	45
4.3 Stability and electronic structure.....	47
4.3.1 Density of States as a function of width and edge reconstruction.....	47
4.3.2 Band structure.....	52
4.3.3 Wavefunction visualization of the metallic states.....	53
4.3.4 Edge energy of TMD nanoribbons.....	54
4.4 Conclusion.....	56
Chapter 5 - Edge states in TMDs.....	57
5.1 Introduction to the Shockley Model.....	59
5.2 Results and Discussion.....	61
5.3 Conclusion.....	66
Chapter 6 - TMD nanoribbons with adsorbed O and OH.....	67
6.1 Introduction.....	69
6.2 Adsorption and substitution of Oxygen on MoS ₂ nanoribbons.....	70
6.3 Oxygen adsorption on TMD nanoribbons.....	72
6.3.1 Electronic properties of oxidized TMD nanoribbons.....	73
6.3.1.1 Density of States and Band structure.....	74
6.4 Hydroxyl adsorption on TMD nanoribbons.....	77

6.4.1 Density of States and Band structure.....	79
6.5 TMD nanoribbons with 50% O and OH adsorption.....	80
6.5.1 The effect of adatoms concentration on the electronic properties.....	81
6.6 TMD nanoribbons as candidates for Oxygen and Hydrogen Evolution Reactions	83
6.7 Conclusion.....	84
Conclusions	87
Appendix	89
References	91

Abbreviations

Atomic simulation environment	ASE
Brillouin zone points	kpts
Density functional theory	DFT
Density of states	DOS
Exchange – correlation potential	XC
Generalized – gradient approximation	GGA
Grid – based projector augmented wave method	GPAW
Grid points	gpts
Highest occupied molecular orbital	HOMO
Hydrogen evolution reaction	HER
Linear combination of atomic orbitals	LCAO
Local density approximation	LDA
Local spin density approximation	LSDA
Lowest unoccupied molecular orbital	LUMO
Nanoribbon width	n_c
Oxygen evolution reaction	OER
Perdew – Burke – Ernzerhof functional	PBE
Surface energy (edge energy)	γ
Tight binding approximation	TBA
Transition metal dichalcogenides	TMDs

CHAPTER 1

INTRODUCTION

Chapter 1

Introduction

1.1 Introduction to TMDs

Since the isolation of graphene other layered materials have been intensively studied, with transition metal dichalcogenides (TMDs) of the type MX_2 (M=transition metal and X=chalcogen) being of particular interest, due to their unique electronic properties[1-3]. Such materials include MoS_2 , WS_2 , MoSe_2 and WSe_2 which both in 2D and 3D formations present semiconducting character[4-10], while in the case of MoS_2 there is strong evidence that in the quasi-1D structures, the material is metallic[11-13].

Apart from being a model system for the structure of edges, MoS_2 nanoribbons have been studied extensively as they offer a unique electronic structure that combines features of MoS_2 and graphene. Bollinger et. al, [12,13] predicted the existence of metallic edge states in MoS_2 nanoribbons using electronic structure calculations. Ridolfi et al., [14] studied the effect of short and long-range disorder on MoS_2 zig-zag nanoribbons, and found that the metallic states are robust against structural disorder. TMD nanoribbons were later synthesized by Camacho-Bragado et al.. attached to MoO_3 clusters [15] and by Wang et al., [16] inside carbon nanotubes. In this paper Wang et al., included DFT calculations that showed spin polarization at E_F for MoS_2 nanoribbons with a fully saturated Mo edge by Sulfur atoms. Theoretical studies also include the work of Li et al., [17] who performed spin-polarized calculations and predicted that zig-zag MoS_2 nanoribbons are magnetic and are more stable than triangular nanoclusters, Kou et al., [18] who showed that strain and applied electric field can alter dramatically both magnetic and electronic behavior, and Kim et al., [19] who found that armchair nanoribbons can be stabilized by H adsorption and possess a semiconducting character with strong excitonic effects. Presence of metallic edges seems to be a general feature of hexagonal 2D materials [20,21]. In previous work [22], we reported that the metallic edges alter the dielectric permittivity of the nanoribbons and that the spatial extent of this effect is around 5 Å from the edge of the material. Finally, MoS_2 nanoribbons could play a key role in the hydrogen evolution reaction [23,24], and graphene support enhances these features [25,26]. Yu et al., [27] verified the tunability of edge states through the use of external electric fields and hydrogen absorption.

Although the stability of metallic states in MoS_2 and their electronic structure is well established [13,28], little is known about nanoribbons of MoSe_2 , WS_2 and WSe_2 . In this research our main goal is to address two issues regarding the thermodynamic stability and the electronic structure in all four common TMD nanoribbon edges. First we examine the thermodynamic stability of various edge reconstructions under relevant experimental conditions in chalcogen reach environment. Second we study the electronic structure of quasi – 1D nanoribbons and we examine how robust the edge-related metallic states are and what is the position of the Fermi level of the metallic region relative to the Fermi level of the 2D bulk. We find that all TMD nanoribbons present metallic edges and we analyze our results using the Shockley theory. Finally, we repeat our calculations for TMD nanoribbons in O/OH reach environment and we find that the metallic edges are robust even in the case of environmental exposure.

1.2 Structural properties of TMDs

Transition metal dichalcogenides (TMDs) are highly anisotropic crystalline layered materials with a structure similar to graphite. In bulk formation TMDs consist of hexagonal MX_2 layers (M=transition metal and X=chalcogen) which are weakly coupled with Van der Waals interactions [1,2], creating a structure that can be easily exfoliated for the extraction of few layers or even a 2D TMD monolayer. This procedure is benefited by the difference of the strength between the interlayer and intralayer bonds. A monolayer consists of atoms bounded with a strong mix of ionic and covalent bonds [3]. Figures 1.2a and 1.2.b offer a schematic representation of the bulk and 2D structures.

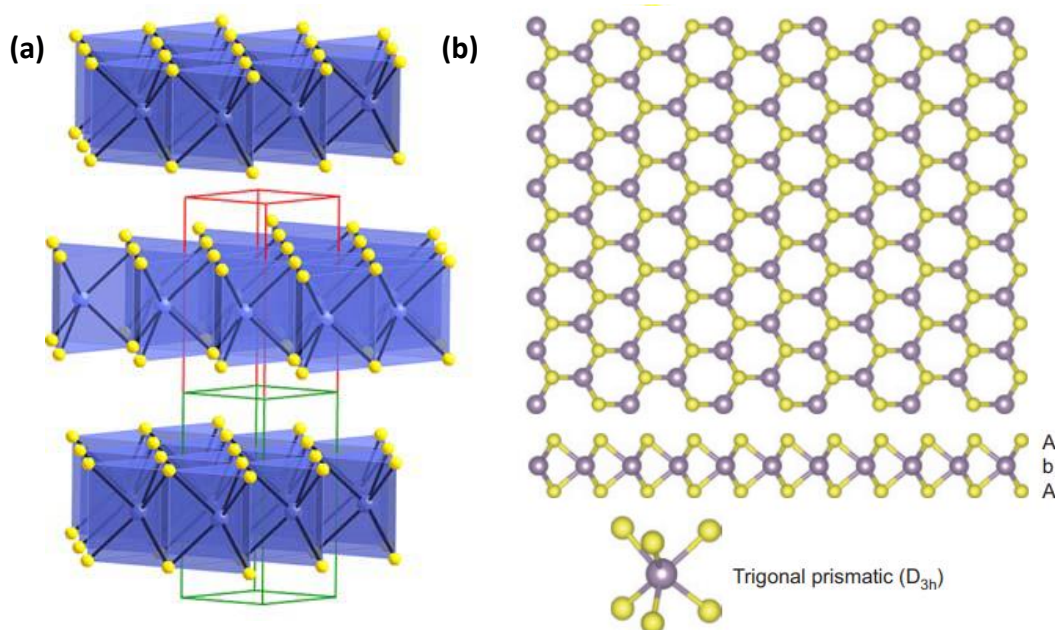


Figure 1.2: (a) Side view of the 3D structure of layered TMDs presenting the Chalcogen-Metal-Chalcogen stacking of trigonal prisms. Reprinted figure by permission from John Wiley and Sons: Roldan, J. A. Silva-Guillén, M. Pilar López-Sancho, F. Guinea, E. Cappelluti and P. Ordejón, Electronic properties of single-layer and multilayer transition metal dichalcogenides MX_2 ($\text{M}=\text{Mo}, \text{W}$ and $\text{X}=\text{S}, \text{Se}$), *Annalen der Physik*, 526, 347-357, 2014. Copyright 2014 by WILEY-VCH Verlag GmbH & Co. KGaA, Weinheim [3]. (b) Top and side view of a TMD monolayer (2D). Reprinted figure by permission from Springer Nature Customer Service Centre GmbH: Nature Publishing Group, *Nature Chemistry*, 5 263-275, The chemistry of two-dimensional layered transition metal dichalcogenide nanosheets, *Nature Chemistry*, M. Chhowalla HS Shin, G. Eda, LJ Li, KP Loh and H. Zhang, 2013 [29]. In both figures yellow color represents the chalcogen atoms (A) while blue the metals (B).

Depending on the composition of the material, the thickness of each layer varies from 3.1 Å in the case of MoS_2 to 3.2 Å for WSe_2 . The interlayer distances lie in the same range, while the bond lengths between metal and chalcogen atoms in the same layer range between 1.5 Å and 1.6 Å [30].

1.3 Physical properties and applications

As opposed to the zero-gap semi-metallic graphene [31], MX_2 ($\text{M}=\text{Mo}, \text{W}$ and $\text{X}=\text{S}, \text{Se}$) in both 3D and 2D formations are semiconductors [4,6-9,32-34]. However, when lowering the dimension, the gap turns from indirect to direct [4-5,7-9,33-34]. This unique property was explained by performing bandstructure calculations for TMDs at different dimensions [3,10,35]. These studies showed that decreasing the number of layers in the bulk structure of TMDs causes a blue shift of the indirect energy gap, which eventually when we have only a single-layer the gap becomes direct. The blue shift of the energy gap in MoS_2 is shown in figure 1.3.1. Similar shifts were observed in all semiconducting transition metal dichalcogenides. The increase in the numerical values of energy gap in the four most common TMDs (MoS_2 , MoSe_2 , WS_2 and WSe_2), when lowering the dimension from 3D to 2D, is presented in table 1.3.

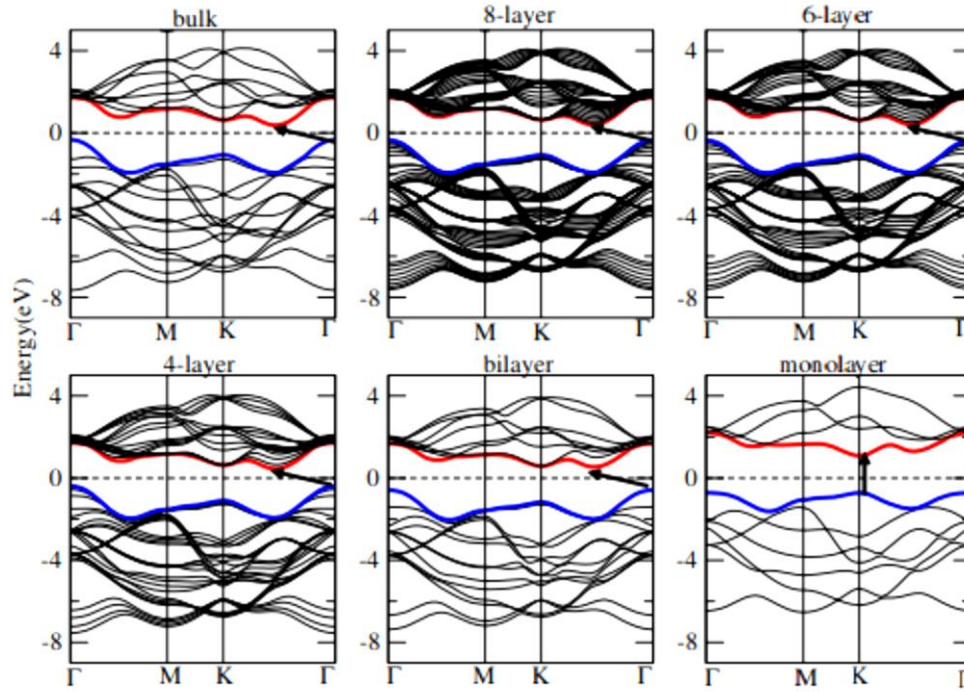


Figure 1.3.1: Theoretical calculation of the bandstructure of MoS₂ showing the blue shift of the energy gap. Different graphs correspond to different number of layers in the calculation. In all graphs red and blue curves show the highest occupied and lowest unoccupied levels respectively. The energy gap is shown with arrows, while the Fermi level is set at 0 eV. Reprinted figure by permission from Springer Nature Customer Service Centre GmbH: Nature Publishing Group, The European Physical Journal B - Condensed Matter and Complex Systems, 85, 186, Electronic structure of transition metal dichalcogenides monolayers 1H-MX₂ (M=Mo, W; X=S, Se, Te) from ab initio theory: new direct gap semiconductors, A. Kumar and P. K. Ahluwalia, 2012. [35]

	E_g (eV) Bulk (3D)	E_g (eV) 2D
MoS₂	1.20	1.69
MoSe₂	1.09	1.51
WS₂	1.35	1.85
WSe₂	1.23	1.63

Table 1.3: Table of values of the energy gaps of MX₂ TMDs. In the bulk form the values presented here are experimental and the gap is indirect at the K-Γ direction of the Brillouin zone [33]. In the 2D structure TMDs the values were calculated theoretically with GGA and the semiconducting gap is direct and found at the K point of the Brillouin zone [10].

In 2010, Mak et al., examined the effect of the tunable gap in MoS₂ with photoluminescence (PL) [4]. The results showed that the monolayer MoS₂ presents intense light emission by a factor of more than 10⁴ compared to the bulk material (see Fig.: 1.3.2). The intense photoluminescence occurs at energy of

1.9eV, which lies in the region of visible spectrum suggesting that MoS₂ is a great candidate for optoelectronic applications such as photovoltaics.

The application of transition metal dichalcogenides in the industry is not something new, for example MoS₂ has been widely used for decades as a lubricant. The introduction of a variety of nanostructures (nanosheets, nanoribbons, nanotubes, etc..) with intriguing physical properties has attracted great interest in the scientific community only recently [36-65]. In 2013 Zhang et al., performed theoretical calculations on zig-zag WS₂ nanoribbons and observed magnetic moment fluctuations when the structure undergoes strain [59]. Lin et al. in 2014 suggested that after nanotube unzipping WS₂ could be a great candidate for hydrogen evolution reaction [60]. Finally, recent studies on Molybdenum Disulfide indicate the presence of metallic character in 1D nanoribbons [11-13,22,67-69]. Helveg et al., in 2000 noticed with scanning tunneling microscopy of MoS₂ nanoclusters on Au substrate, an intense yellow brim [11]. Bollinger et al., in 2001 simulated with DFT an MoS₂ stripe and concluded that this brim occurs due to metallic edge states crossing the band gap of the 2D material [12]. The MoS₂ nanoclusters are shown in figure 1.3.3.

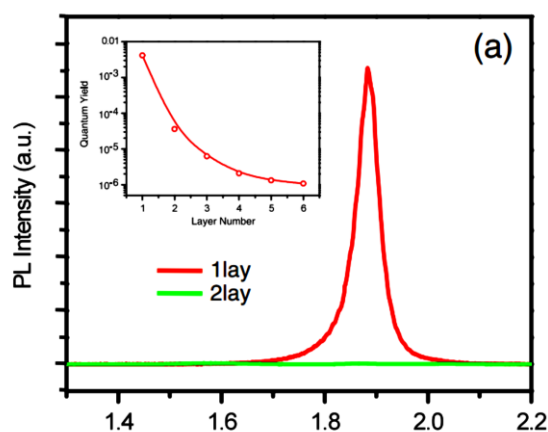


Figure 1.3.2: Comparison of the photoluminescence (PL) spectra of bilayer and single – layer MoS₂ showing the intense PL of the monolayer at 1.9 eV. Reprinted figure with permission from K. F. Mak, C. Lee, J. Hone, J. Shan and T. F. Heinz, Atomically thin MoS₂ : a new direct – gap semiconductor, Physical Review Letters, 105, 136805, 2010. Copyright 2010 by the American Physical Society. [4]

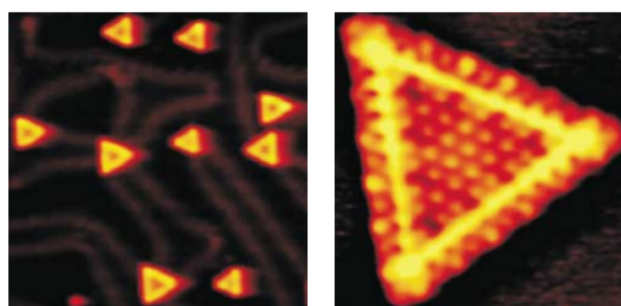


Figure 1.3.3: (left) STM imaging of MoS₂ nanoclusters on Au (111) substrate. **(right)** Zoomed figure on one MoS₂ nanocluster showing the intense yellow brim around the edges. Reprinted figure with permission from M. V. Bollinger, J. V. Lauristen, K. W. Jacobsen, J. K. Nørskov, S.Helveg and F. Besenbacher , One-Dimensional Metallic Edge States in MoS₂ , Physical Review Letters, 87, 196803, 2001. Copyright 2001 by the American Physical Society. [12]

In this study we examine four semiconducting MX_2 TMDs (MoS_2 , MoSe_2 , WS_2 , WSe_2) with ab – initio calculations in the quasi 1D nanoribbon structure and we present our findings on the electronic properties of nanoribbons with various widths, different edge configurations and in the presence of chalcogen [66], oxygen and hydroxyl environments.

This PhD thesis is organized as follows: In chapter 2, we introduce the theoretical and computational methods used in this study (Density Functional Theory and Tight – Binding Approximation). Then perform simulations of model S structures, with both methods, to obtain insight into the electronic structure of S compounds and perform a comparison between DFT and TBA in terms of accuracy and time consumption (chapter 3). In chapter 4, we perform DFT calculations for the stability and electronic properties (such as density of states and bandstructure) of MoS_2 , MoSe_2 , WS_2 and WSe_2 nanoribbons. For each material, we consider seven nanostructures that vary in width and edge reconstruction by the addition of various numbers of extra chalcogen atoms (from zero to four) and we present a comparison of electronic properties between the 1D and 2D materials. In all cases we find that our materials present metallic edges, the physics of which is described in chapter 5 according to the Shockley theory. Finally, we examine the same electronic properties in 1D and 2D TMDs, by simulating environmental conditions in an oxygen/hydroxyl reach environment. Our results show that the metallic edges are robust even in the presence of Oxygen atoms or Hydroxyl radicals, as opposed to the semiconducting character of the bulk structure which after oxidization undergoes a red shift and the gap turns from direct to indirect.

CHAPTER 2
THEORETICAL AND
COMPUTATIONAL
METHODS

Chapter 2

Theoretical and computational methods

2.1 Schrödinger equation

The study of phenomena that occur on atomistic level, such as light – matter interactions or the formation of chemical bonds requires the solution of the Schrödinger's equation which is a very complex problem. For that reason, several approximations have been developed such as the ones we use in this PhD thesis, Density Functional Theory and Tight – Binding Approximation. However, depending on the properties that we aim to study, we need to consider which method is the optimum choice. For example, a calculation of a bandstructure done with DFT, although accurate, it is a very demanding project itself even in the case of periodic structures, with no spin polarization taken under consideration. On the other hand, with TBA we can perform a full calculation very fast even in large systems where the periodicity is affected by impurities. In this chapter we describe Density Functional Theory and Tight – Binding approximation DFT and TBA and the computational methods that we used for each theory.

Schrödinger's equation describes quantum phenomena, including those that occur in the matter due to the nuclei – electron interactions among others. When an electronic structure simulation is performed, the modeling of these interactions is required.

The general Schrödinger equation or time – dependent (SE) is:

$$\hat{H}\Psi = i\hbar \frac{\partial}{\partial t} \Psi ,$$

where the Hamiltonian term \hat{H} corresponds to the energy operator and Ψ is the wavefunction. In ground state calculations such as Density Functional Theory (see section: 2.2) time – dependence is not important, and we are only interested in the lowest-energy eigenstate of the Hamiltonian. The Hamiltonian is calculated according to next equation in which the first two terms refer to the kinetic energy of the ions and electrons respectively, while the following terms present the potential energy of each interaction.

$$\hat{H} = \sum_I -\frac{\hbar^2}{2M} \nabla_I^2 + \sum_i -\frac{\hbar^2}{2m} \nabla_i^2 + \frac{1}{2} \sum_{ij} \frac{e^2}{4\pi\epsilon_0 |\vec{r}_i - \vec{r}_j|} + \\ + \frac{1}{2} \sum_{IJ} \frac{Q_I Q_J}{4\pi\epsilon_0 |\vec{R}_I - \vec{R}_J|} - \frac{1}{2} \sum_{iI} \frac{e Q_I}{4\pi\epsilon_0 |\vec{r}_i - \vec{R}_I|} ,$$

where, \vec{r}_i, \vec{r}_j and \vec{R}_I, \vec{R}_J refer to positions of electrons and nuclei respectively.

Solving the time - independent Schrödinger equation still remains difficult and necessary approximations need to be done, such as the Born – Oppenheimer approximation.

2.1.1 Born – Oppenheimer approximation

The Born – Oppenheimer approximation dictates an uncoupled movement of the nuclei and the electrons. This assumption is based on the difference between the two masses, leading to a much slower movement of the nuclei in contrast to the electrons. Usually the motion of atoms are either ignored (as we

do in this work) or taken into account by means of Newton's law of motion. As a result of this approximation the Schrödinger's equation and the Hamiltonian are transformed respectively:

$$\hat{H}_e \Psi_e = E_e \Psi_e$$

$$\text{with } E = E_e + E_{ion} \quad \text{and} \quad E_{ion} = \sum \frac{1}{2} m_I u_I^2 + \frac{1}{2} \sum_{IJ} \frac{Q_I Q_J}{4\pi\epsilon_0 |\vec{R}_I - \vec{R}_J|}$$

$$\hat{H} = \sum_i -\frac{\hbar^2}{2m} \nabla_i^2 + \frac{1}{2} \sum_{ij} \frac{e^2}{4\pi\epsilon_0 |\vec{r}_i - \vec{r}_j|} - \frac{1}{2} \sum_{iI} \frac{e Q_I}{4\pi\epsilon_0 |\vec{r}_i - \vec{R}_I|}$$

2.2 Density Functional Theory (DFT)

Density Functional Theory (DFT) is an ab initio computational method which is based on the idea of a non uniform spatial electron distribution. In this case in order to determine the system properties all we have to do is take under consideration a function of the electrons arrangement, hence a ground state function (Hohenberg – Kohn theorem [70]). Also according to the Kohn – Sham equations [71], Schrödinger's equation for an interacting system can be solved if we calculate the potential of a fictitious non interacting system with the same density. In the simplified system of DFT we can calculate its properties by using the following equations:

$$\text{Electron density:} \quad N = \int n(\vec{r}) d^3r,$$

where the electron density $n(\vec{r})$ is a functional of the normalized ψ :

$$n(\vec{r}) = \sum_{i=1}^N |\psi(\vec{r})|^2$$

In this case the Hamiltonian is a functional of electron distribution,

$$H_e = \sum_{i=1}^N H[n(\vec{r})]$$

The Hamiltonian for an electron in DFT, is a sum of four parameters: electron kinetic energy and three potentials that are due to the electron – nucleus interaction, the electron – electron interaction and the exchange – correlation potential, respectively.

$$H = -\frac{\hbar^2}{2m} \nabla^2 + V_{n-e} + V_{e-e} + V_{xc}$$

By analyzing the previous equation, we see that the terms of the first two potentials are easily calculated by the following equations:

$$V_{e-e} = \frac{e^2}{4\pi\epsilon_0} \int \frac{n(\vec{r}')}{|\vec{r}-\vec{r}'|} d^3 r' , \quad V_{n-e} = \sum_I \frac{eQ_I}{4\pi\epsilon_0} \frac{1}{|\vec{r}-\vec{R}_I|},$$

and that the presence of the electron density simplifies the process, since there is no need for wavefunction calculations in many body systems. However, the last term, which corresponds to the exchange – correlation potential, is the most important factor in the density functional theory because it corrects the error of the electron self–interaction, which leads to the overestimated electron – electron interaction. For the calculation of the XC potential many functionals have been developed. For this thesis we used the generalized gradient approximation (GGA).

2.2.1 Generalized – Gradient approximation (GGA)

For the purposes of calculating the exchange – correlation potential a use of an appropriate approximation is essential. Even though the exact functional for a many body interaction system is unknown, there are several approximations with the simplest one being the local density approximation (LDA) or in more generalized form, the local spin density approximation approximation (LSDA) [72]. The LDA approximation uses the known XC energy of the free electron gas and considers the total XC energy of the system as a sum of the local energies in the simulation box, which makes its appropriate for density homogeneous systems. Generalized – gradient approximation, however, calculates the total XC energy with respect to the density gradient, providing more accurate results in surface simulations [72-73].

$$E_{XC}^{LDA}[n] = \int n \epsilon_{XC}^{gas}(n) dr \quad E_{XC}^{GGA}[n] = \int n \epsilon_{XC}^{GGA}(n, \nabla n) dr$$

In GGA the most common functional and the one we use in our study, is the Perdew – Burke – Erzrenhof (PBE) [72].

2.2.2 DFT code

For the density functional theory calculations we use the grid – based projector augmented wave (GPAW) [74] computational package which is open–source and implements the PAW method created by Peter Blöch in 1994[75]. PAW method uses pseudo–wavefunctions which include the core states and by considering the frozen core approximation it reconstructs the full wavefunctions and electron density.

GPAW uses a real–space uniform grid for the representation of the wavefunctions transforming Ψ in Schödinger's equation to a more complex, yet smoother and easier to calculate wavefunction (see Fig.: 3.2). From the atomic properties GPAW is developed as a module of the Atomic Simulation Environment (ASE) [76], which provides a useful database for atomistic and electronic simulations.

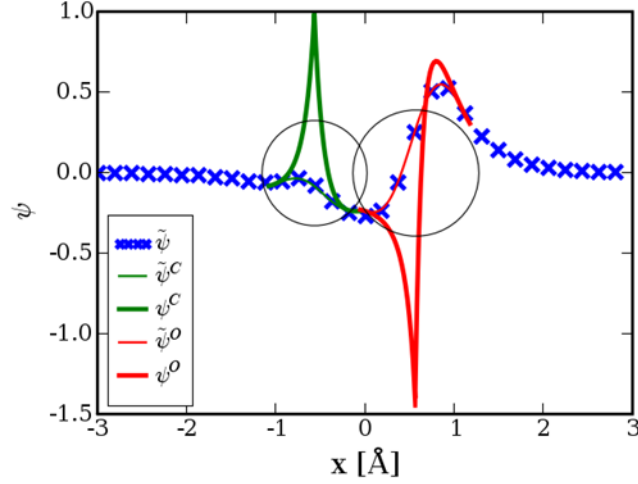


Figure 3.2: Schematic representation of $2\sigma^*$ orbital of CO[77].

In order to generate accurate results in a theoretical study, one has to set some parameters to create a simulation as close as possible to the real structure. In GPAW these parameters are the real-space grid, defined by the grid points (g-points) and the grid width, and the number of k-points in the reciprocal lattice.

Grid points are inversely proportional to the grid width, which equals:

$$h \approx \frac{\alpha}{gpts+1} \quad , \quad \alpha \text{ being the length of the simulation box.}$$

Also, according to Bloch's theorem, in a periodic system the energy eigenvalues can be described as the product of a periodic function, with a period of $u(\vec{r})$ and the exponential factor $\exp(i\vec{k} \cdot \vec{r})$:

$$\psi(\vec{r}) = e^{(i\vec{k} \cdot \vec{r})} u(\vec{r})$$

That way all the physical properties in the system are periodic functions of the eigenstates of the \vec{k} vector. We only need to consider \vec{k} vectors inside the primitive unit cell of the reciprocal lattice of the system, which is called the Brillouin zone. For example, in order to solve the Schrödinger's equation for a many body problem in one dimension, we just have to take the k points that fall in the range between $\pm \frac{\pi}{\alpha}$. Again, α is the lattice constant.

Although the more grid points and k-points one uses in a simulation, the study will present more accurate results, the computation can be very time-consuming. Thus, we have to perform sample calculations in order to find the appropriate number of real and reciprocal space points that will generate the most accurate results in the minimum time. For example, in most materials, in order to have good energy convergence the grid width should be around 0.2 Å. We have confirmed this empirical rule in our simulations where the optimum grid spacing was found to be 0.19 Å. All parameters used in our simulations will be provided when the corresponding structure is presented.

2.3 Tight Binding Approximation

2.3.1 Introduction

The tight binding approximation (TBA) [78-81] is based on the theory of linear combination of atomic orbital (LCAO), adapted for solving condensed matter problems. According to this theory, one can solve the Schrodinger equation by considering the electron wavefunction as linear combination of Bloch waves, where each wave corresponds to a specific type of atomic orbital. The key approximation of TBA is that only few atomic orbitals are taken into account (usually only p and s) and only electron hopping between neighbouring atoms is allowed. In that manner this method simplifies the construction of the Hamiltonian matrix just by considering the overlap of the atomic orbitals in a system. To familiarise better with the tight binding approximation it will be useful to consider some examples for periodic and non – periodic systems. In the following sections, we will introduce some simple structures which will guide us through the mathematical analysis of the tight binding approximation.

2.3.2 Tight Binding Approximation in periodic infinite chain

First, let's consider two neighbouring atoms in a 3D crystal structure. According to the tight binding approximation when two atoms (A and B) are found in a distance α with each other, the corresponding electrons close to the nuclei will feel a potential similar to that of a single atom. However, due to the presence of the second atom an overlap of the atomic orbitals will occur leading to a wavefunction which is a linear combination of Bloch waves.

$$\Psi(\mathbf{r}) = \sum_i e^{ik \cdot \mathbf{R}_i} \Phi(\mathbf{r} - \mathbf{R}_i),$$

where Φ corresponds to specific atomic orbitals (s, p, d etc.) and \mathbf{R}_i is the real space translation vector in the crystal.

Now let's look at the infinite linear chain shown in figure 2.3.2.1. This periodic chain consists of atoms at a fixed distance α along the \hat{x} direction and atomic orbitals s, p_x , p_y and p_z . Due to orthogonality the only orbital interactions that will participate in the formation of the molecular orbital, are the ones with the same orientation, such as s- p_x , p_x - p_x , p_y - p_y etc.

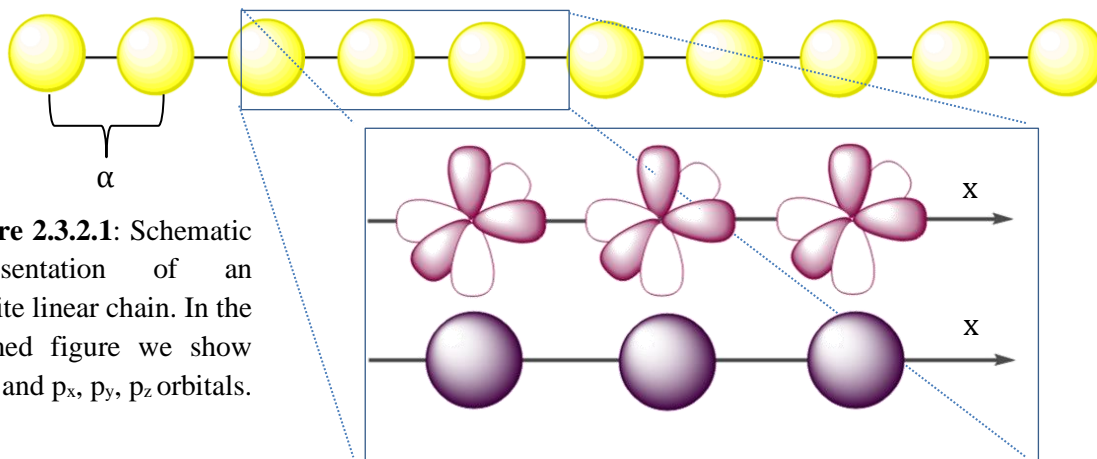


Figure 2.3.2.1: Schematic representation of an infinite linear chain. In the zoomed figure we show the s and p_x , p_y , p_z orbitals.

With this criterion in mind and the fact that the Hamiltonian matrix is Hermitian, the construction of the Hamiltonian matrix for a periodic linear chain (considering only the first neighbours) is a 4x4 matrix, where the calculation of the matrix elements is required for only the five out of sixteen (orthogonal elements present zero overlap, plus s-p_x overlap equals p_x-s). The Hamiltonian matrix for a general basis set s, p_x, p_y, p_z is given below:

$$\begin{pmatrix} H_{ss} & H_{sp_x} & 0 & 0 \\ H_{p_x s} & H_{p_x p_x} & 0 & 0 \\ 0 & 0 & H_{p_y p_y} & 0 \\ 0 & 0 & 0 & H_{p_z p_z} \end{pmatrix}$$

Where $H_{sp_x} = H_{p_x s}$.

Analytically for the interactions we will have:

$$H_{ss} = \langle s; 0 | H | s; 0 \rangle + \langle s; 0 | H | s; \alpha \rangle e^{ik_x \alpha} + \langle s; 0 | H | s; \alpha \rangle e^{-ik_x \alpha}$$

$$H_{p_x p_x} = \langle p_x; 0 | H | p_x; 0 \rangle + \langle p_x; 0 | H | p_x; \alpha \rangle e^{ik_x \alpha} + \langle p_x; 0 | H | p_x; \alpha \rangle e^{-ik_x \alpha}$$

$$H_{p_y p_y} = \langle p_y; 0 | H | p_y; 0 \rangle + \langle p_y; 0 | H | p_y; \alpha \rangle e^{ik_x \alpha} + \langle p_y; 0 | H | p_y; \alpha \rangle e^{-ik_x \alpha}$$

$$H_{p_z p_z} = \langle p_z; 0 | H | p_z; 0 \rangle + \langle p_z; 0 | H | p_z; \alpha \rangle e^{ik_x \alpha} + \langle p_z; 0 | H | p_z; \alpha \rangle e^{-ik_x \alpha}$$

$$H_{sp_x} = H_{p_x s} = \langle s; 0 | H | p_x; \alpha \rangle e^{ik_x \alpha} + \langle s; 0 | H | p_x; \alpha \rangle e^{-ik_x \alpha}$$

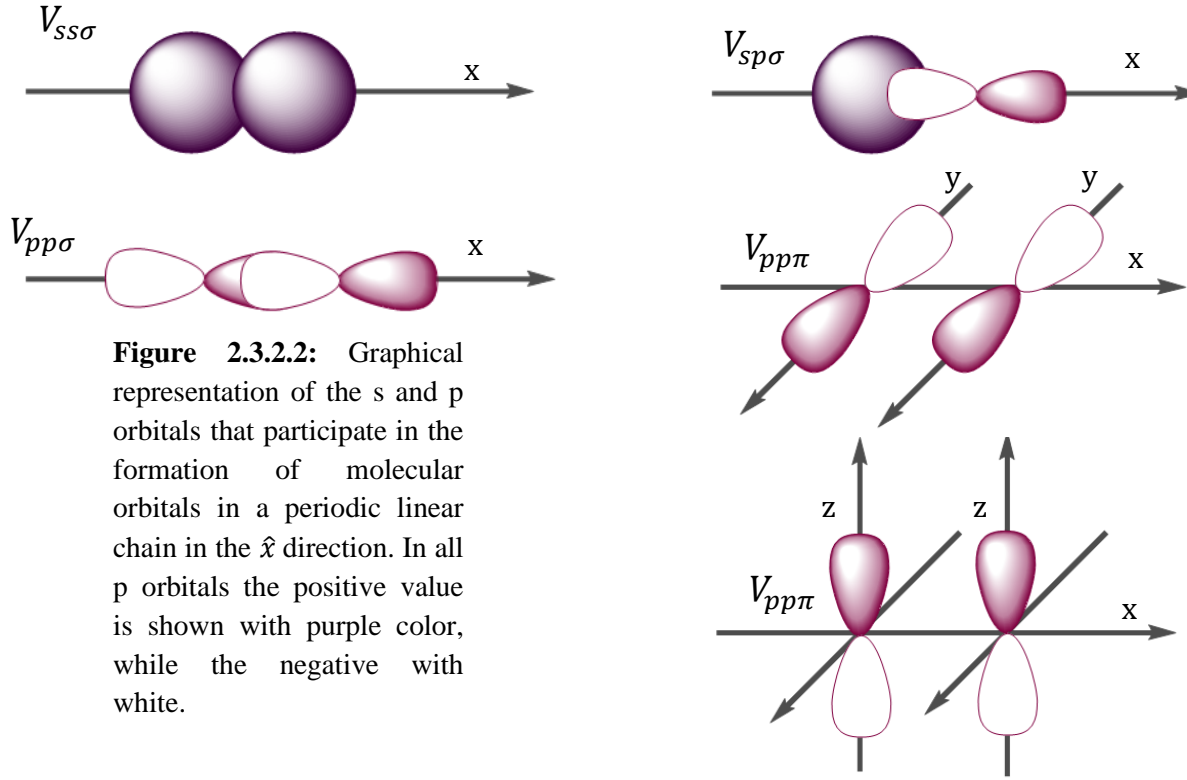
Slater and Koster in 1954 [82], proposed the use of known integrals $V_{ss\sigma}$, $V_{sp\sigma}$, $V_{pp\sigma}$, $V_{pp\pi}$, $V_{ss\sigma}$ etc., of the diatomic molecules for the description of the general 3D integral:

$$\langle \Phi_n^*(\mathbf{r}) | H | \Phi_m(\mathbf{r} + \mathbf{R}_j) \rangle$$

In the approximation of Harisson, these integrals describe electron sharing between two orbitals in neighbouring atoms and are given by:

$$V_{ll'm} = \eta_{ll'm} \frac{\hbar^2}{m_e d^2}$$

Where d is the distance between atoms (in our case d=α), l and l' refer to the orbital types of atoms A and B, m corresponds to the quantum number and m_e is the electron mass respectively[83]. The graphical representation of the orbital interactions in our linear chain is shown in figure 2.3.2.2.



The dimensionless coefficients $\eta_{ll'm}$ in the diatomic molecule integrals depend on the structure of the unit cell. Froyen and Harisson in 1979 extracted the values of these coefficients for cubic and tetrahedral structures by equating band energies from LCAO and free – electron theory [84]. The theoretical values of $\eta_{ll'm}$ are given in table 2.3.2.

	Simple cubic structure	Tetrahedral structure
$\eta_{ss\sigma}$	-1.23	-1.39
$\eta_{sp\sigma}$	1.90	1.84
$\eta_{pp\sigma}$	3.70	3.24
$\eta_{pp\pi}$	-1.23	-0.93

Table 2.3.2: Theoretical values for the dimensionless coefficients $\eta_{ll'm}$ as obtained from the calculations for simple structures by Froyer and Harisson [83].

Using the integrals for the diatomic molecule with s and p orbitals from Slater and Koster and by substituting the resulting H_{nm} elements in the Hamiltonian matrix, the matrix for this linear infinite chain is then transformed to:

$$\begin{pmatrix} \varepsilon_{ss}(0) + 2V_{ss\sigma}\cos(k_x\alpha) & 2V_{sp\sigma}\sin(k_x\alpha) & 0 & 0 \\ 2V_{sp\sigma}\sin(k_x\alpha) & \varepsilon_{p_xp_x}(0) + 2V_{pp\sigma}\cos(k_x\alpha) & 0 & 0 \\ 0 & 0 & \varepsilon_{p_y p_y}(0) + 2V_{pp\sigma}\cos(k_x\alpha) & 0 \\ 0 & 0 & 0 & \varepsilon_{p_z p_z}(0) + 2V_{pp\sigma}\cos(k_x\alpha) \end{pmatrix}$$

Single – electron energies are simply the eigenvalues of the matrix above. Similarly, we can construct the hamiltonian matrix for any possible structure (3D, 2D). However, depending on the structure, periodic/non-periodic, linear or cyclic, we have to consider some other factors. For example, for a structure similar to cyclohexane which is not periodic and presents a chair conformation, we calculate the Hamiltonian matrix by analysing the three p orbitals to the three axis using direction cosines and since there is no periodicity the Hamiltonian matrix elements will be only a function of the diatomic molecular integrals $V_{ll'm}$. In the next section we will present this procedure using the solid Sulfur hexagonal structure as an example.

2.3.3 Tight Binding Approximation in hexagonal Sulfur – A non periodic structure

Lets consider now a different case where we impliment the tight binding approximation. In this case we will consider a hexagonal non periodic system and we will use the structure of Sulfur shown in figure 2.3.3.1.

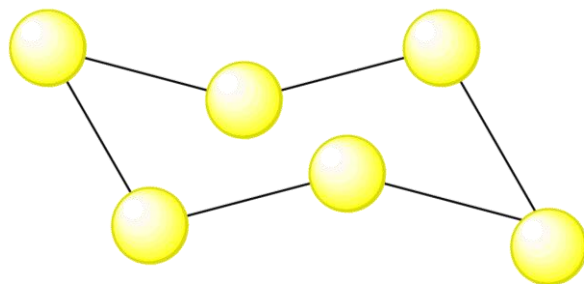


Figure 2.3.3.1: Side view of a non periodic ring structure.

From figure 2.3.3.1 it is obvious that not all atoms are on the same plane and that the cyclic configuration causes a rotation of the atomic orbitals along the vertical axis that goes through the center of the structure. The Hamiltonian matrix is now a 24x24 matrix, which consists of 4x4 blocks corresponding to each neighbouring interactions. Notice that in the matrix shown below the first block corresponds to the first atom (A), while the second describes the bond between atoms A and B. Hence the two elements shown here with H_{ss} , although both refer to s orbitals, are not equal in numerical values.

$$\begin{pmatrix} H_{ss} & 0 & 0 & 0 & H_{ss} & H_{sp_x} & H_{sp_y} & H_{sp_z} & \cdots \\ 0 & H_{p_x p_x} & 0 & 0 & H_{p_x s} & H_{p_x p_x} & H_{p_x p_y} & H_{p_x p_z} & \cdots \\ 0 & 0 & H_{p_y p_y} & 0 & H_{p_y s} & H_{p_y p_x} & H_{p_y p_y} & H_{p_y p_z} & \cdots \\ 0 & 0 & 0 & H_{p_z p_z} & H_{p_z s} & H_{p_z p_x} & H_{p_z p_y} & H_{p_z p_z} & \cdots \\ H_{ss} & H_{sp_x} & H_{sp_y} & H_{sp_z} & H_{ss} & 0 & 0 & 0 & \cdots \\ H_{p_x s} & H_{p_x p_x} & H_{p_x p_y} & H_{p_x p_z} & 0 & H_{p_x p_x} & 0 & 0 & \cdots \\ H_{p_y s} & H_{p_y p_x} & H_{p_y p_y} & H_{p_y p_z} & 0 & 0 & H_{p_y p_y} & 0 & \cdots \\ H_{p_z s} & H_{p_z p_x} & H_{p_z p_y} & H_{p_z p_z} & 0 & 0 & 0 & H_{p_z p_z} & \cdots \\ \vdots & \vdots & \vdots & \vdots & \vdots & \vdots & \vdots & \vdots & \ddots \end{pmatrix}$$

For the calculation of the matrix elements we consider a second cartesian system for the orbitals of atom B in reference to the orbitals of atom A. Figure 2.3.3.2 presents typical examples of the the analysis of atoms' B orbitals in response to the atom A.

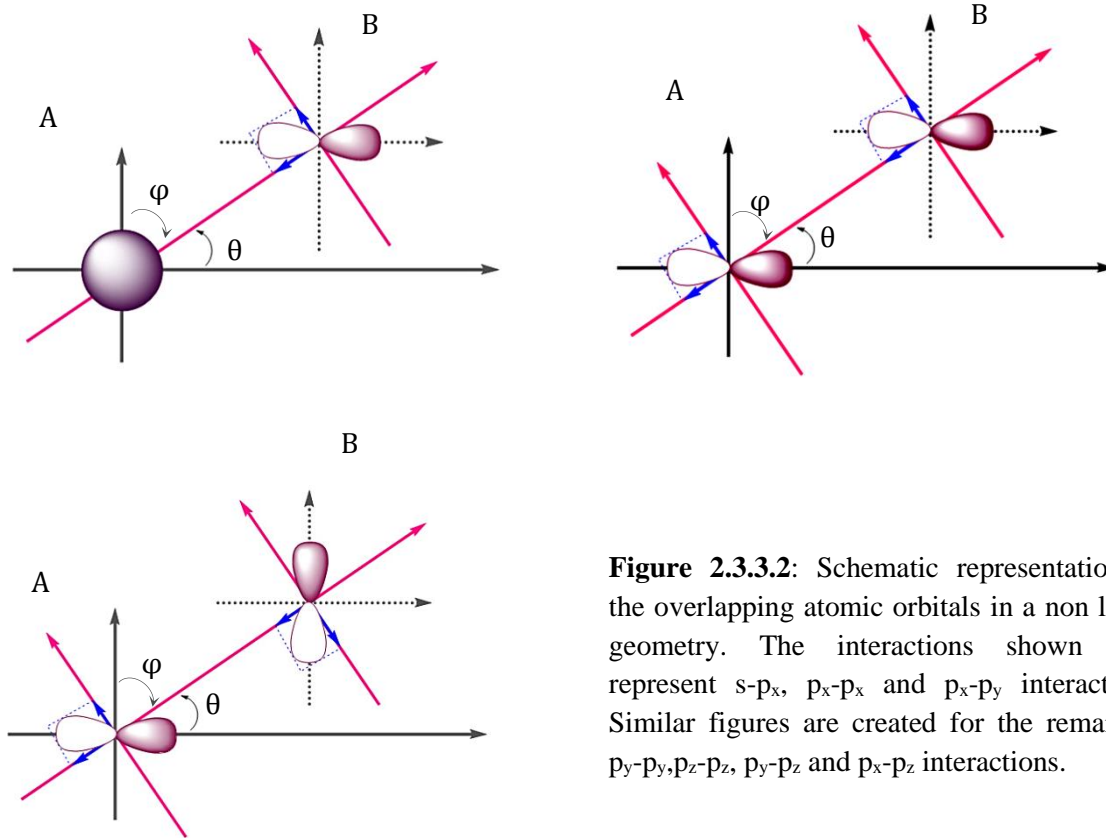


Figure 2.3.3.2: Schematic representation of the overlapping atomic orbitals in a non linear geometry. The interactions shown here represent s- p_x , p_x - p_x and p_x - p_y interactions. Similar figures are created for the remaining p_y - p_y , p_z - p_z , p_y - p_z and p_x - p_z interactions.

The matrix elements for the corresponding interactions of a cyclic non periodic structure shown in figure 2.3.3.2, are given below. Similarly, we calculate the remaining components.

$$H_{sp_x} = V_{sp\sigma} \cos\theta$$

$$H_{p_x p_x} = V_{pp\sigma} \cos^2 \theta + V_{pp\pi} \sin^2 \theta$$

$$H_{p_x p_y} = V_{pp\sigma} \cos \theta \cos \varphi - V_{pp\pi} \cos \theta \cos \varphi \quad , \quad \text{where : } \theta = \frac{\pi}{2} - \varphi$$

$$\vdots$$

$$\vdots$$

In both previous examples we have shown a typical procedure for the calculation of a bandstructure through tight binding approximation. Although mathematical analysis can be a painstaking process depending on what structure we have and how many orbitals need to be considered, the most difficult part is the calculation of the diatomic molecule integrals. A solution to that problem is to consider the $V_{ll'm}$ integrals as parameters in the calculation and perform a fit of the energy eigenvalues to the ones calculated from a more accurate method such as DFT. In the next chapter we perform such calculations for hypothetical structures using the grid-based projector augmented wave computational method (GPAW) [77].

2.3.4 Tight – Binding code

For the tight – binding calculations, we use our own codes, developed during the course of this thesis. The codes are written in python and use the ASE library [67] to handle the atomic positions. The tight – binding scheme of Harisson [73] is employed, where the various η parameters (see section 2.3.2) can be modified in order to fit DFT results. Diagonalization of Hamiltonian and parameter fitting is done by means of numpy and scipy packages.

CHAPTER 3

Simulations of model S structures

Chapter 3

Simulations of model S structures

3.1 Introduction

In this chapter we perform calculations for the bandstructure for several hypothetical structures, periodic and non-periodic, with DFT and tight binding approximation and we find the appropriate $\eta_{ll'm}$ values for the calculation of the $V_{ll'm}$ integrals. For the density functional theory calculations we use the open-source GPAW [77] computational package and the Atomic Simulation Environment (ASE) [76]. We construct multiple structures with both methods and fit our TBA energy eigenvalues results to the those from DFT.

For the selected structures we were inspired from materials that we used in the nanoribbon study, that we will present later in this PhD thesis. For example, the main unit cell of solid Sulfur consists of three six-membered rings, while the metastable α -monoclinic formation of Selenium consists of three eight-membered rings [84]. For the hypothetical structures we created unit cells that consist only of one six-membered or eight-membered ring. Other formations where a simple linear chain (periodic and non-periodic), a zig-zag chain and a structure that consists of four atoms similar to the edge of transition metal dichalcogenide nanoribbons (TMDs) shown in section 4.2.5. In our research we found that TMD nanoribbons present metallic edge states that show a topological – insulator like behavior [66]. Here we aim to examine the band topology with tight – binding approximation for the d and p orbitals of the valence electrons in MX_2 (M=Mo, W, X=S, Se). Starting with the Sulfur structures (with s and p orbitals) we hope to find universal values of the $\eta_{ll'm}$ parameters and the atomic terms ϵ_{ss} and ϵ_{pp} for all the possible structures and then implement the TBA in our nanoribbons to further analyze their complex band – structures.

Our research follows three steps. First we construct multiple hypothetical structures which consist of s and p orbitals, using the GPAW method and we calculate the energy eigenvalues. Then we perform a tight binding calculation for the energy eigenvalues of the same structures and finally using the Levenberg – Marquardt algorithm [85], we perform a non – linear fit of these energies to the DFT results in order to extract the appropriate values for the $\eta_{ll'm}$ parameters in the $V_{ll'm}$ integrals and the atomic terms ϵ_{ss} and ϵ_{pp} .

3.2 Infinite linear chain

The first simulation that we perform is the calculation of the bandstructure of a periodic infinite linear chain consisting of Sulfur atoms, with s and p orbitals. For the construction of the linear chain with DFT we use a tetragonal unit cell with lattice constant $a=2.05$ Å consisting of only one Sulfur atom and we impose periodic boundary conditions along \hat{x} axis. The lattice constant a corresponds to the S-S bond length as taken from webelements database [86]. A vacuum of 12 Å was imposed along axis \hat{y} and \hat{z} . In GPAW, a parameter that is important for the good energy convergence is the number of electron bands used in the calculation. In other chapters of our study we introduce much more unoccupied bands than the actual number of the antibonding bands. Here, since we aim to compare our results to TBA the number of bands is set exactly to the number of orbitals in the calculation, i.e. nbands=4. Also in order to compare our DFT bandstructure results to TBA we use (10x1x1) k-points in the reciprocal lattice and (12x72x72)

g-points for the real space grid. The (10x1x1) k-points are equivalent with the formation of a non-periodic linear chain consisting of ten atoms, such as the chain presented in the next section. The unit cell used in our calculation is shown in figure 3.2.1.

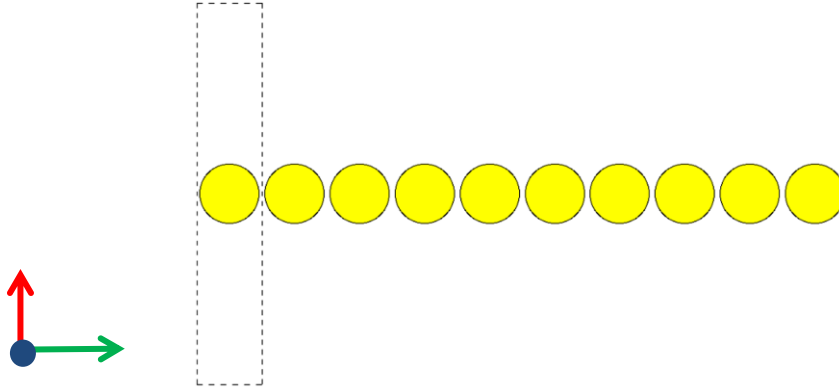


Figure 3.2.1: Schematic representation of the periodic linear chain used in our simulations. The axis shown here are color-coded as such; \hat{y} axis is shown in red, \hat{x} axis in green and \hat{z} in blue.

Following the procedure explained in chapter 2 subsection 2.3.2 we construct the Hamiltonian matrix for the same structure and we develop a code that calculates the energy eigenvalues as a function of the 10 k-points. Finally, we fit our results for the tight binding calculation to the resulting eigenvalues from DFT and we find the appropriate $\eta_{ll'm}$ and ϵ_{ss} , ϵ_{pp} values for an accurate bandstructure calculation through TBA. The calculated bandstructure and the energy eigenvalues as a function of level number are presented in figures 3.2.2a,b.

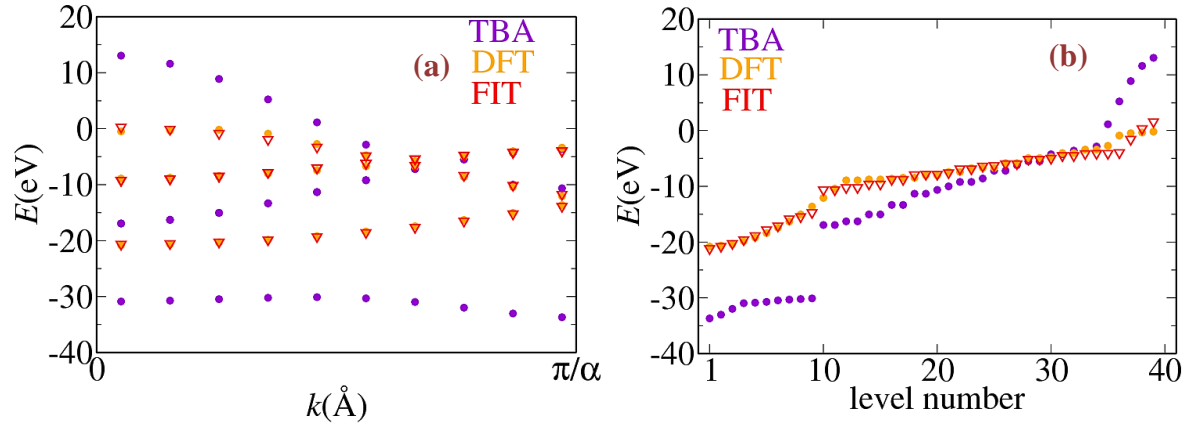


Figure 3.2.2: (a) Comparison of the bandstructure of an infinite linear chain, calculated with DFT and TBA as a function of the k vector in the reciprocal lattice. (b) Energy eigenvalues as a function of level (molecular orbital) number for the same structure. In both figures the symbols presenting the energy eigenvalues are color-coded according to the calculation method (DFT and TBA are shown with orange and purple circles respectively, while red triangles correspond to our results after the fit).

From figure 3.2.2a we see that even though we have four atomic orbitals in the calculation, thus 4 bands, in the graph only three are obvious at each k-point. This results suggests a degeneracy of two bands in all cases. A closer look to figure 3.2.2b shows clearly the presence of degeneracy. To perform the data fit we begin with the values of $\eta_{ll'm}$ and ϵ_{ss} , ϵ_{pp} suggested by Harisson for a tetragonal cell [83] and allow our TBA results to perform an ubounded fit to the DFT calculation. The red triangles in both graphs show that our fit is in very good agreement with the energy eigenvalues found with GPAW. Table 3.2.1 presents the initial and final values used in our fit calculation.

$\eta_{ss\sigma}$	$\eta_{sp\sigma}$	$\eta_{pp\sigma}$	$\eta_{pp\pi}$	ϵ_s	ϵ_p	ΔE (all/ E_F)
-1.39 i	1.88 i	3.24 i	-0.93 i	-20.80 i	-10.27 i	0.07/0.18
-0.39 f	1.19 f	0.77 f	-0.47 f	-14.88 f	-7.36 f	

Table 3.2.1: Table of the initial (i) and final (f) TBA parameters as derived from the fit calculation. In last column we present the deviation error as calculated taking under consideration all data points or only the energy eigenvalues at a range ± 5 points around the Fermi level at -4.76eV.

3.3 DFT and TBA for non periodic stuctures

Here we perform calculations for the energy bandstructure in a variety of non-periodic structures with DFT and according to the TBA method analyzed in chapter 2 subsection 2.3.3. In this study as mentioned in the introduction of this chapter, we simulate various hypothetical structures such as; linear and zig-zag chains, hexagonal and octagonal rings and a four – atom structure similar to the nanoribbon edge presented later in section 4.2.5. Again we consider only atoms with s and p orbital (ex. S or Se) and draw a fit of the eigenvalues in order to find the most suitable $\eta_{ll'm}$, ϵ_{ss} and ϵ_{pp} parameters for an accurate energy bandstructure calculation with tight binding approximation.

As opposed to the previous section, we perform multiple calculations starting from different numerical values of these parameters in order to find universal values that give good results in all structures. Table 3.2.2 in the end of this section presents the initial and final parameters for our calculations shown in the corresponding figures. These results present only selected examples of the much more many calculations we performed for the data fit (~30 calculations per structure that did not provide good results). In all cases a vacuum of 12 Å is imposed along all directions and the number of bands is set to the number of atoms \times four orbitals. Figures 3.3.1 to 3.3.2 present our results for energy eigenvalues of all structures through DFT and TBA and the corresponding fits.

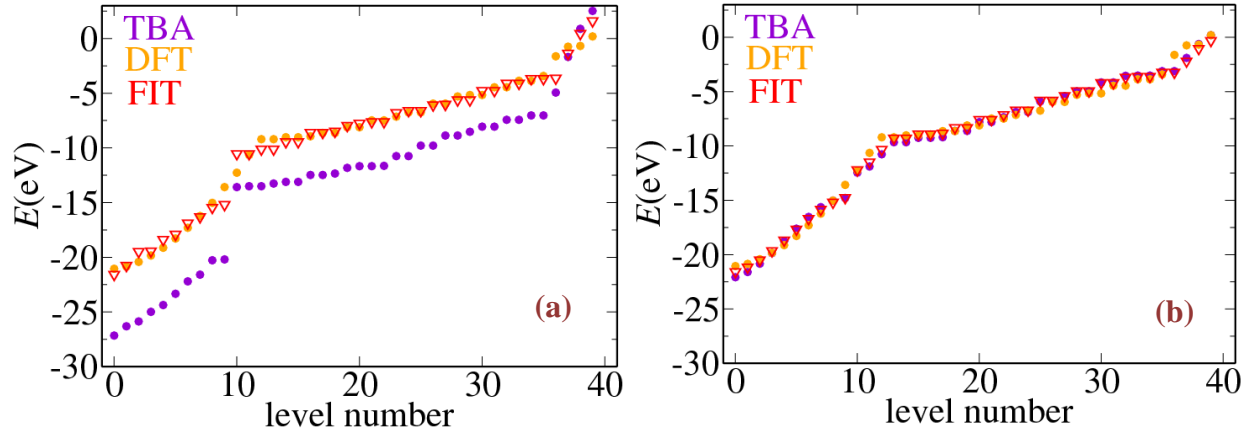


Figure 3.3.1: Comparison of the energy eigenvalues of a non periodic linear chain consisting of 10 atoms, calculated with DFT and TBA as a function of energy level number. In both figures red triangles show the TBA energy eigenvalues after fitting the data to DFT. The initial $\eta_{ll'm}$, ε_{ss} and ε_{pp} in figures (a) and (b) were taken from Harrison and from the medium value of ring structures (m_r) respectively. Table 3.2.2 presents a collection of the initial and final TBA parameters.

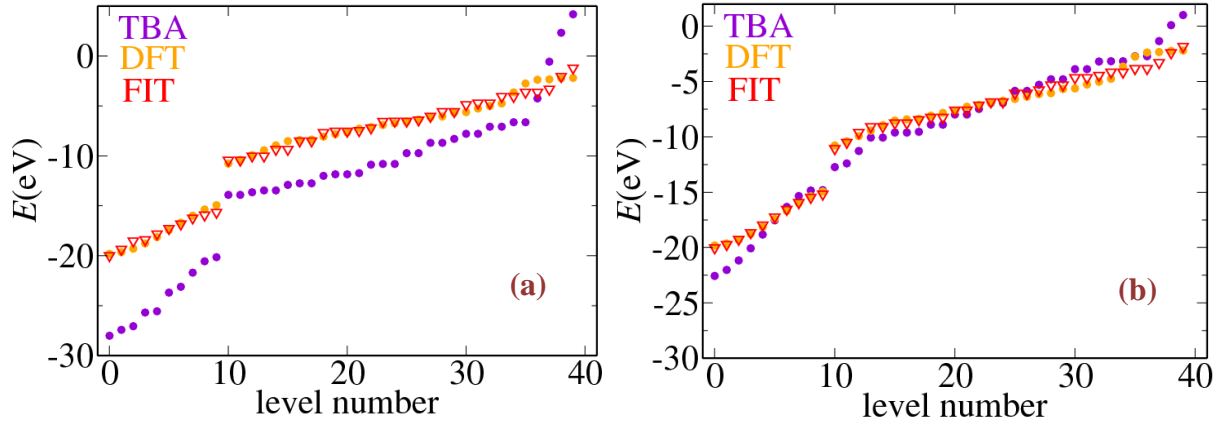


Figure 3.3.2: Same as figure 3.3.1 for the structure of a non periodic zig-zag chain consisting of 10 atoms. Notice that in this case the range in the \hat{y} axes differs in graphs (a) and (b). This difference is due to the lowering of the TBA energy values at highest orbitals.

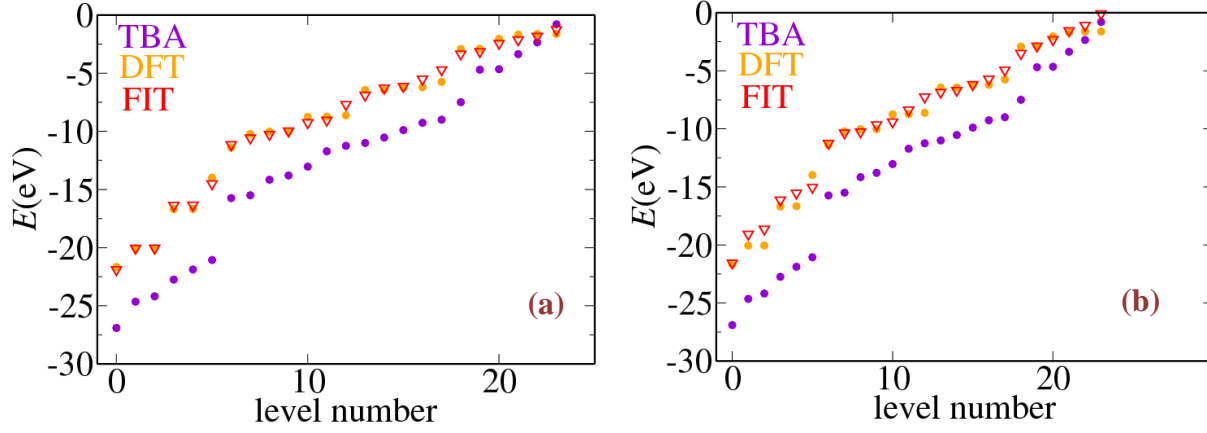


Figure 3.3.2.3: Comparison of the energy eigenvalues for a hexagonal ring structure calculated with DFT and TBA as a function of energy level number. In both figures the initial $\eta_{ll'm}$, ε_{ss} and ε_{pp} were taken from Harisson. Red triangles present the TBA energy eigenvalues after fitting the data to DFT. In figure (a) all data points were considered in the fit, while in figure (b) we selected specific values at a range close to the Fermi level. Table 3.2.2 presents a collection of the initial and final TBA parameters.

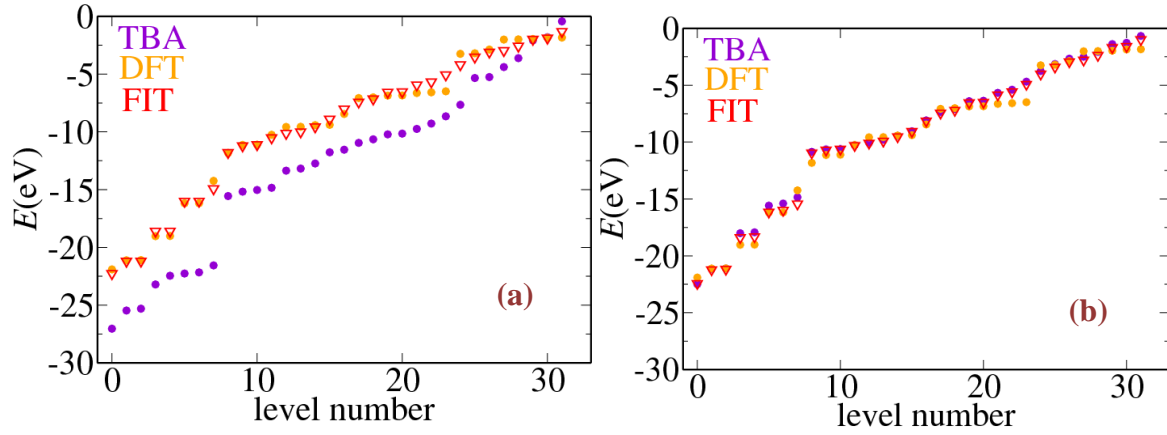


Figure 3.3.4: Comparison of the energy eigenvalues for an octagonal ring structure, calculated with DFT and TBA as a function of energy level number. In both figures red triangles show the TBA energy eigenvalues after fitting the data to DFT. The initial $\eta_{ll'm}$, ε_{ss} and ε_{pp} in figures (a) and (b) were taken from Harisson and from the final parameters in the case of four atoms (in table 3.4.4. noted as “edge”).

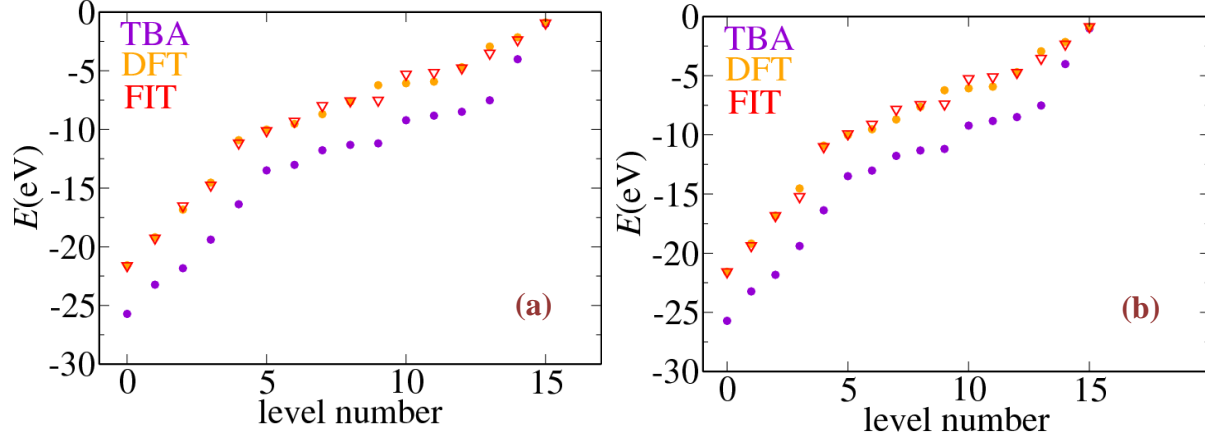


Figure 3.3.5: Comparison of the energy eigenvalues for a four atom structure (edge), calculated with DFT and TBA as a function of energy level number. In both figures the initial $\eta_{ll'm}$, ϵ_{ss} and ϵ_{pp} were taken from Harisson. Red triangles present the TBA energy eigenvalues after fitting the data to DFT. In figure (a) all data points were considered in the fit, while in figure (b) we selected specific values at a range close to the Fermi level. Table 3.2.2 presents a collection of the initial and final TBA parameters

In our calculations we have considered only interactions between first neighbouring atoms ($d < 3.0 \text{\AA}$). We performed several calculations for the fit selecting specific number of points. Because we are interested in electronic properties in some cases we focus our fit in the energies around the Fermi level. Our results after the fit show very good agreement for the energy eigenvalues with the DFT calculations and confirm that both TBA and DFT can provide accurate descriptions of the energy band – structure. This is further confirmed by the calculation of the deviation error provided in table 3.2.2, where in most cases the energy deviation is found in the third decimal point. However, our search for universal $\eta_{ll'm}$, ϵ_{ss} and ϵ_{pp} values even after a huge amount of test calculations, was unsuccessful. Hence, a description of the band – structures of all the nanoribbons studied later in our research, would require more extensive calculations, which is beyond the scope of this study.

3.4 Conclusion

In this chapter we presented a comparison of two computational methods (TBA and GPAW) for the calculation of the bandstructure in hypothetical periodic and non – periodic structures inspired by the twofold coordinated solid Sulfur and Selenium. With both methods we extracted the energy eigenvalues in S clusters and performed a fit of the results as derived from the tight – binding calculations, to the ones from the most accurate DFT calculation.

We found that after the fit, we can conclude on the appropriate values for the $\eta_{ll'm}$, ϵ_{ss} and ϵ_{pp} in the diatomic molecule integrals $V_{ll'm}$, that will lead to the accurate description of the energy bandstructure using the tight – binding approximation. We tried to find values for these parameters that are universal regardless of the structure of the material, however, such an ambitious pursuit proved to be much more difficult and time – consuming than expected. For that reason, from now on in our study, all the calculations are performed only with DFT as implemented by the GPAW package.

Notations: i=initial, f=final, b=bounded, u=unbounded, r=relaxed, l=linear, a=accordeon, h=hexagon, o=octagon, e= edge, m= midval (r=ring structure, c=chain structure), H=Harrison



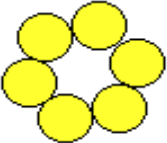
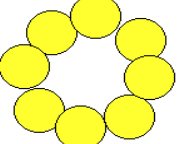
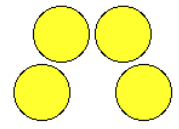
Structure	eV/atom	d 1st (Å)	d 2nd (Å)	Fit points/ Figure no.	$\eta_{ss\sigma}$	$\eta_{sp\sigma}$	$\eta_{pp\sigma}$	$\eta_{pp\pi}$	ϵ_s	ϵ_p	ΔE (all/ E_F)
linear 	-3.303	2.050	4.100	All/ 3.3.1a	-1.39 iHu	1.88 iHu	3.24 iHu	-0.93 iHu	-20.80 iHu	-10.27 iHu	0.22/ 0.06
					-1.115 f	1.897 f	1.911 f	-0.986 f	-15.637 f	-7.109 f	
				All/ 3.3.1b	-1.11 im _r u	0.27 im _r u	1.88 im _r u	-0.94 im _r u	-18.18 im _r u	-6.39 im _r u	0.08/ 0.08
					-0.98 f	0.00 f	1.71 f	-0.87 f	-18.17 f	-6.26 f	
zig-zag 	-3.296	2.292	4.100	All/ 3.3.2a	-1.39 iHu	1.88 iHu	3.24 iHu	-0.93 iHu	-20.80 iHu	-10.27 iHu	0.16/ 0.13
					-0.50 f	1.54 f	0.93 f	-0.87 f	-15.85 f	-7.03 f	
				All/ 3.3.2b	-1.11 im _r u	0.27 im _r u	1.88 im _r u	-0.94 im _r u	-18.18 im _r u	-6.39 im _r u	0.06/ 0.15
					-0.62 f	0.00 f	1.18 f	-0.67 f	-17.60 f	-6.45 f	
Hexag. r 	-3.888	~2.082	~3.253	All/ 3.3.3a	-1.39 iHu	1.88 iHu	3.24 iHu	-0.93 iHu	-20.80 iHu	-10.27 iHu	0.08/ 0.06
					-1.05 f	0.0 f	1.77 f	-0.99 f	-18.20 f	-6.20 f	
				[0,4-7, 13-22]/ 3.3.3b	-1.39 iHu	1.88 iHu	3.24 iHu	-0.93 iHu	-20.80 iHu	-10.27 iHu	0.31/ 0.18
					-1.52 f	1.66 f	2.10 f	-1.12 f	-15.07f	-6.88 f	
Octag. r 	-3.867	~2.065	~3.354	All/ 3.3.4a	-1.39 iHu	1.88 iHu	3.24 iHu	-0.93 iHu	-20.80 iHu	-10.27 iHu	0.10/ 0.18
					-1.03 f	0.0 f	1.89 f	-0.86 f	-18.60 f	-6.55 f	
				All/ 3.3.4b	-1.26 ieb	0.8 ieb	1.97 ieb	-0.98 ieb	-17.73 ieb	-6.41 ieb	0.21/ 0.03
					-1.13 f	0.79 f	1.91 f	-0.93 f	-18.13 f	-6.55 f	
edge 	-3.736	2.041	3.328	All/ 3.3.5a	-1.39 iHu	1.88 iHu	3.24 iHu	-0.93 iHu	-20.80 iHu	-10.27 iHu	0.00/ 0.00
					-1.26 f	0.8 f	1.97 f	-0.98 f	-17.73 f	-6.41 f	
				[0,2,4,6, 9-15]/ 3.3.5b	-1.39 iHu	1.88 iHu	3.24 iHu	-0.93 iHu	-20.80 iHu	-10.27 iHu	0.00/ 0.00
					-1.78 f	0.91 f	1.96 f	-0.94 f	-17.90 f	-6.33 f	

Table 3.2.2 : Complete set of TBA parameters prior and after the fit for non periodic structures. For each structure we present initial and final $\eta_{ll'm}$, ϵ_{ss} and ϵ_{pp} parameters (as explained by the blue notations) for two different fits in respect to the previous figures. In all cases we present the distances between one atom and the first ($d < 3.0$ Å) and second neighbours and the cohesive energy per atom. The deviation errors after each fit showed in the last column, confirm our excellent agreement with DFT results.

CHAPTER 4
ELECTRONIC PROPERTIES
OF TMD NANORIBBONS

Chapter 4

Electronic properties of TMD nanoribbons

4.1 Introduction

Previous studies on MoS₂ prove that as opposed to the semiconducting character of the material in 2D and 3D formations, when the dimension is lowered to quasi 1D, such as the nanoribbon structure, MoS₂ presents metallic character around the edges [11-13,22,67-69]. In our research we aim to understand which parameter is the one that affects this unique change in the electronic character of the four most common quasi 1D TMDs (MoS₂, WS₂, MoSe₂, and WSe₂). For that reason we construct a variety of TMD zig – zag nanoribbons that differ in composition, width and edge termination, creating a total of a total of 140 nanoribbons and we perform calculations for their properties such as the edge energy, the density of states and the bandstructure and we visualize the wave functions of the edge – localized states. The electronic properties of 1D TMDs are then compared to the 2D materials.

4.2 Computational methodology

To construct the nanoribbons, we start from a rectangular repeat unit (see Fig. 4.2.1) with sides of length α along the \hat{x} and $\alpha\sqrt{3}$ along the \hat{y} directions, where α is the lattice constant of the 2D material [10] presented in table 4.2. In relation to the original lattice vectors \mathbf{a}_1 , \mathbf{a}_2 of the honeycomb lattice, which is the underlying crystal lattice for the bulk 2D layer of the TMDs, the new vectors that describe the repeat unit are given by: $\mathbf{a}_3=\mathbf{a}_1-\mathbf{a}_2$, $\mathbf{a}_4=\mathbf{a}_1+\mathbf{a}_2$. This repeat unit contains 2 metal (M) and 4 chalcogen (X) atoms, at the sites labeled A and B in Fig. 4.2.1. In this figure, red circles (marked A) represent the positions of M atoms and yellow circles (marked B) represent the projections of X atoms on the plane.

We construct a supercell by repeating this unit cell n_c times along the \hat{y} direction, and then a vacuum region is added along the \hat{y} and \hat{z} directions. Periodic boundary conditions are imposed along all directions. In the \hat{y} and \hat{z} direction, consecutive slabs are separated by 12.0 Å of vacuum. For few test systems, we repeated the calculation with open boundary conditions along these directions, where the wavefunctions and density vanish at the edges of the simulation box. The two methods gave identical results. The structure formed is a nanoribbon of infinite length along \hat{x} and has a width of n_c cells along \hat{y} , with $1 \leq n_c \leq 7$. This corresponds to nanoribbon widths in the range of 5.5 Å to 42 Å.

The Brillouin Zone (BZ) that corresponds to the new crystal structure defined by the repeat unit is a subspace of the original BZ of the honeycomb lattice, due to folding by the new reciprocal vectors \mathbf{a}_3 , \mathbf{a}_4 , as shown explicitly in Fig. 4.2.1(c). This results in the edge point K of the original BZ being mapped onto an interior point in the new BZ, while the interior point X of the original BZ becomes an edge point in the new BZ. These features are important in interpreting the band structures of the nanoribbons discussed in the following sections.

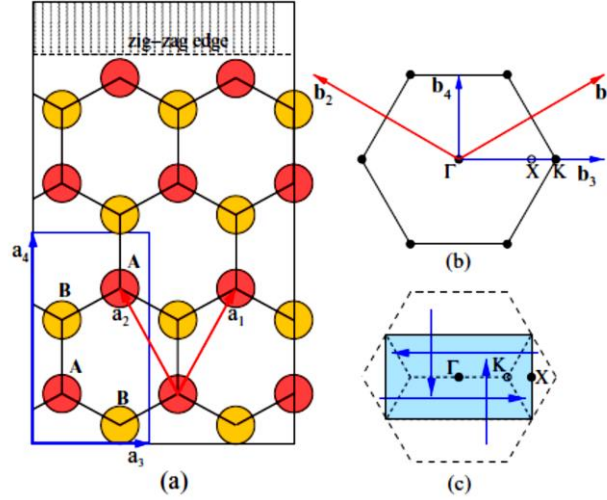


Figure 4.2.1: (a) Definition of the repeat unit (blue rectangle) and the repeat vectors \mathbf{a}_3 (\hat{x} -direction), \mathbf{a}_4 (\hat{y} -direction) (blue arrows) and original lattice vectors \mathbf{a}_1 , \mathbf{a}_2 (red arrows). (b) Brillouin Zone of the bulk 2D structure, with the original reciprocal lattice vectors \mathbf{b}_1 , \mathbf{b}_2 (red arrows) and the new vectors \mathbf{b}_3 , \mathbf{b}_4 (blue arrows) corresponding to the rectangular repeat unit. (c) Folding of the original BZ (dashed black lines) to the new BZ (solid black lines) through the mapping by displacements of $\pm\mathbf{b}_3$, $\pm\mathbf{b}_4$. The positions of special k -points Γ , K and X are marked by solid (K and X, Γ in (b) and (c) respectively) and open dots (X, Γ and K in (b) and (c)).

We perform first-principles electronic structure and total-energy calculations based on Density Functional Theory (DFT), using the real-space Grid-based Projector Augmented-Wave (GPAW) [77]. For the exchange-correlation functional we use the Generalized Gradient Approximation (GGA) of Perdew-Burke-Ernzerhof (PBE) [72]. Although the PBE functional is not the preferred choice for the calculation of the band structure due to its underestimation of the energy gap [87], the use of hybrid functionals and/or many-body equations to treat accurately the excitonic effects [88-90] is beyond the scope of the present work, as we focus on ground-state properties or trends for the electronic features. In GPAW, the computational parameters that need to be taken into account are the grid spacing, h , the number of Monkhorst-Pack k -points for sampling of the Brillouin zone and the thickness of the vacuum region, L_V , beyond the last atoms of the system. The parameters used in our study are $h = 0.19 \text{ \AA}$, $4 \times 1 \times 1$ k -points and $L_V = 12.0 \text{ \AA}$. The lattice parameters a (\hat{x} -direction), c (\hat{z} -direction) and the internal parameter regarding the intralayer S-S distance u are given in table 4.2.

	a (\AA)	c (\AA)	u (\AA)
MoS₂	3.193	13.717	0.635
MoSe₂	3.202	14.169	0.631
WS₂	3.197	13.236	0.630
WSe₂	3.311	13.939	0.628

Table 4.2: Table of the lattice parameters used in our simulations, as they were calculated in Ref [10].

For every width, n_c , we consider five different terminations of the M-edge. These terminations correspond to N_X ($0 \leq N_X \leq 4$) X adatoms decorating the M-edge. The geometrical configuration for the case with two chalcogen adatoms was chosen to be that of a dimer that lies perpendicular to the layer, in

accordance with several theoretical (Bollinger et al. [12]), Byskov et. al. [91]) and experimental (Helveg et al. [11]) observations. All the other structures with two adatoms we tried, yield much higher edge energies, by 0.23 eV/Å or more, above the edge energy of the structure with the dimer. For structures with three and four adatoms, we tried several different structures in order to locate the one with lowest energy; in all cases, the structures with twofold S atoms have by far lowest edge energy. We used the Atomic Simulation Environment (ASE) suite [76] for the generation of structures, atomic relaxation and analysis of the results. For the X-edge we do not expect any reconstruction other than changes in bond lengths [92]. In total, we consider 35 nanoribbon structures for each material and we took into account the full relaxation of atom positions in the first two atomic rows from both edges, as well as all adatom positions. The relaxed structures of five typical MX_2 nanoribbons for $n_c = 2$ are shown in Fig. 4.2.2. In all cases, chalcogen adatoms are two-fold coordinated and have similar bond lengths as in the bulk of the material.

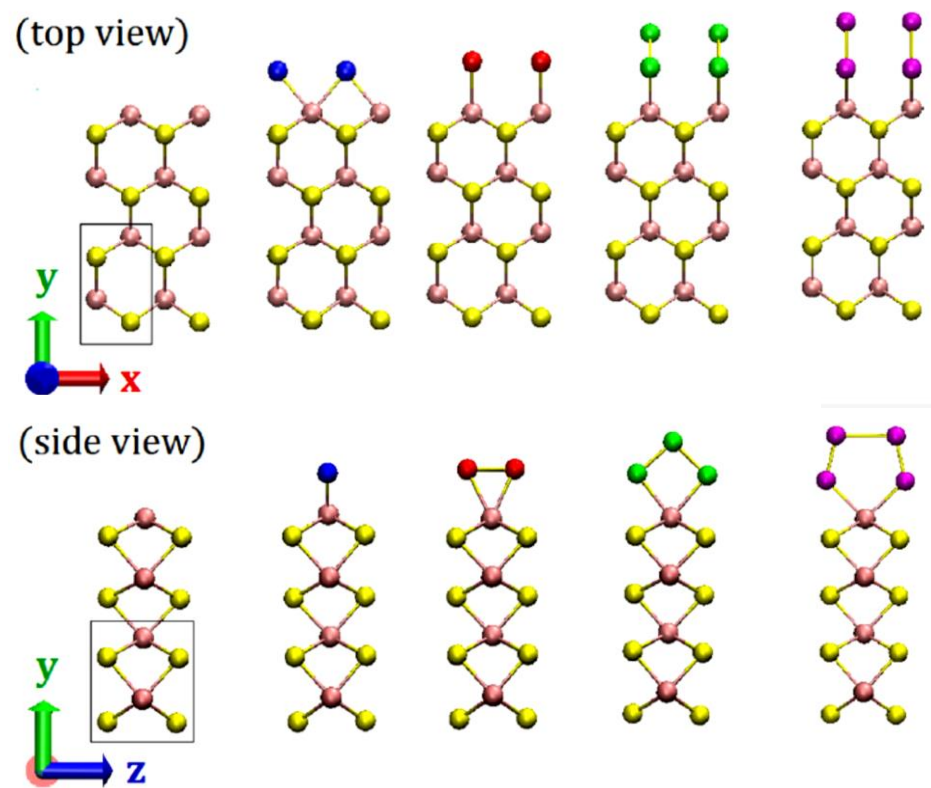


Figure 4.2.2: Structural models (top and side views) of relaxed structures of typical nanoribbons (MX_2 with $n_c=2$) with increasing number of adatoms N_x from zero (left) to four (right), at the metal-terminated zig zag edge. Two unit cells along the \hat{x} -direction of the periodic structure, are shown. Pink and yellow spheres represent the metal and chalcogen atoms, respectively. The extra chalcogen adatoms are color coded blue ($N_x = 1$), red ($N_x = 2$), green ($N_x = 3$), and purple ($N_x = 4$), for reference in the following figures.

4.3 Stability and Electronic structure

4.3.1 Density of states as a function of width and edge reconstruction

Dimensionality plays a key role in the electronic structure of TMDs. In 3D structures, all materials considered here are indirect gap semiconductors [33], while in each case the 2D single-layer

structure is a direct gap semiconductor [10,35]. This shift of the energy gap from K- Γ to K-K points of the Brillouin zone is responsible for the observed photoluminescence.

The density of states (DOS) of a TMD nanoribbon includes a characteristic peak at the Fermi level, E_F , surrounded by a few lower peaks that also lie inside the gap of the 2D material. These states are localized at the upper and lower edge of the nanoribbon along the \hat{y} direction and resemble electrons confined in 1D. We observe the same behavior in all TMDs, all widths and all numbers of chalcogen adatoms: there is a clear peak at E_F , the height of which decreases for increasing nanoribbon width, n_c (see Figs.: 4.3.1.1 – 4.3.1.5). At $n_c \rightarrow \infty$, the peak is expected to disappear.

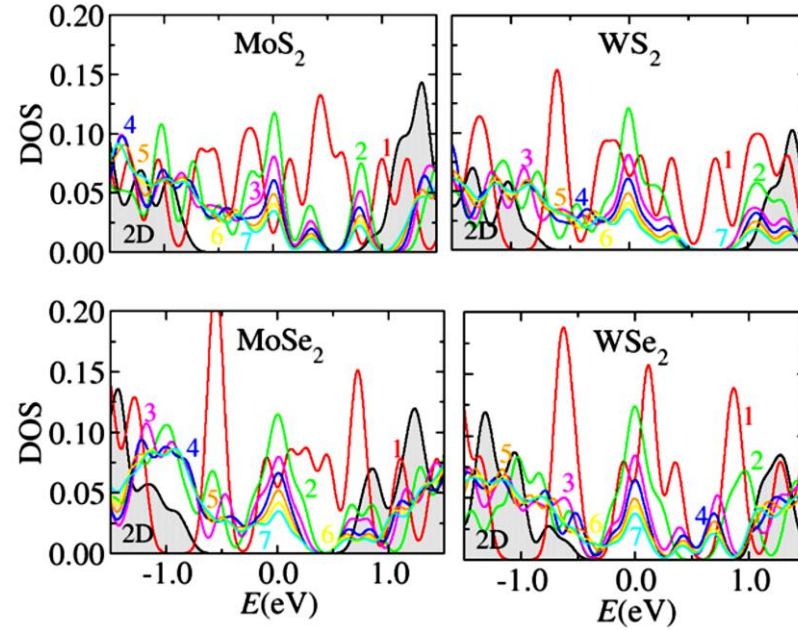


Figure 4.3.1.1: Comparison of the DOS of metal – terminated TMD nanoribbons with various widths to the DOS of 2D monolayers. The density of states of the 2D material is shown with the shaded area, while the color-coded numbers present the number of unit cells, n_c , in the nanoribbon. In all graphs the Fermi level is set at zero eV.

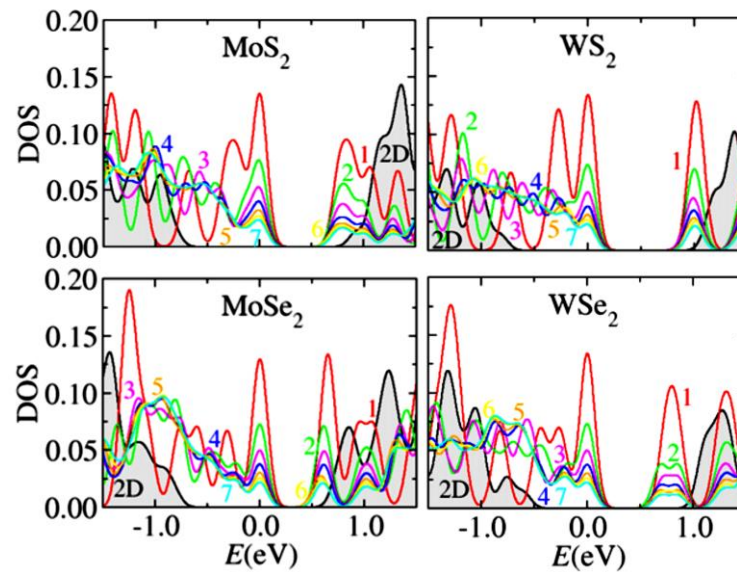


Figure 4.3.1.2: Same as figure 4.3.1.1 for TMD nanoribbons with one chalcogen adatom at the upper edge.

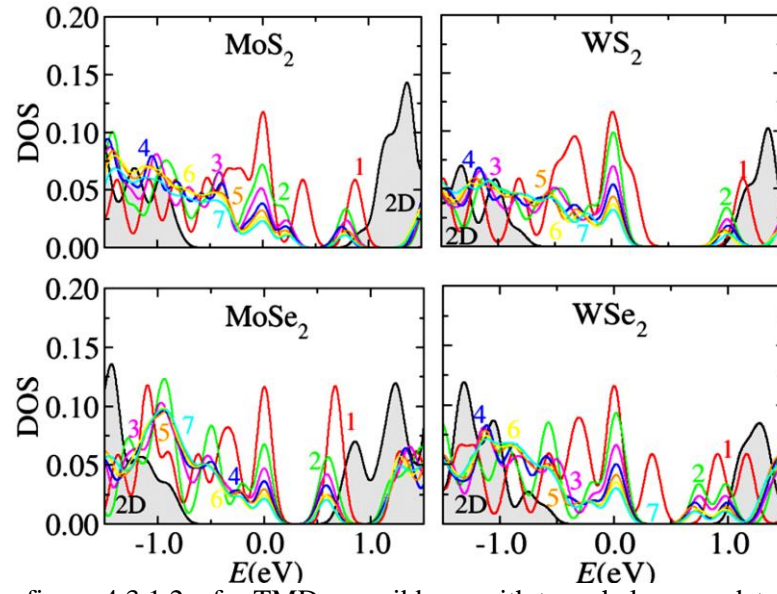


Figure 4.3.1.3: Same as figure 4.3.1.2.a for TMD nanoribbons with two chalcogen adatoms at the upper edge.

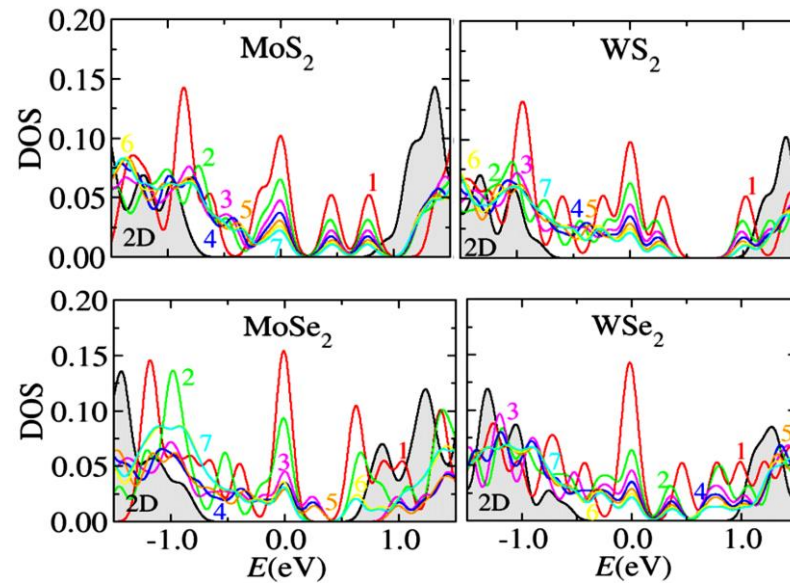


Figure 4.3.1.4: Same as figure 4.3.1.2.b for TMD nanoribbons with three chalcogen adatoms at the upper edge.

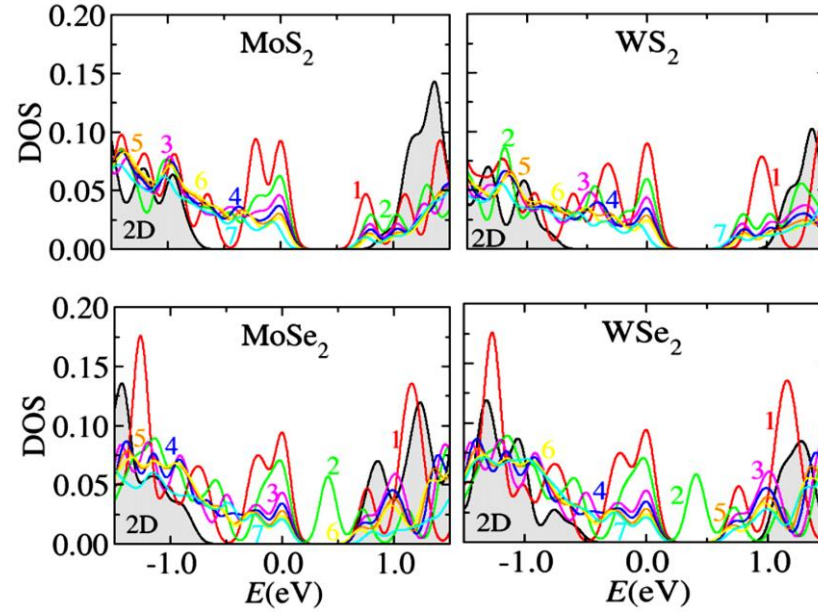


Figure 4.3.1.5: Same as figure 4.3.1.2.c for TMD nanoribbons with four chalcogen adatoms at the upper edge.

The reason for this width – dependence is the following: In the valence band of a nanoribbon with width n_c and N_x adatoms there are $18n_c + 3N_x$ occupied electronic states for each k -point in the Brillouin zone, only few of which are edge states (in the simulation we consider only the 6 valence e^- in both metals and chalcogens, leading to 3 occupied states per atom. For example, in the case of one unit cell and one adatom the total occupied states will be 21.). The contribution of edge states becomes negligible for large n_c . In Fig. 4.3.1.7 we present the DOS of nanoribbons with width $n_c = 6$. At this width, there are enough bulk states to represent the DOS of the 2D material, while the edge states are still prominent and have impact on the properties of the system. The DOS alone might not be enough to characterize the edge states as metallic, as it is important to verify that indeed the Fermi level of the nanoribbon lies within the gap of the 2D material. Aligning the DOS of two systems with different numbers of atoms in order to calculate the difference of their Fermi levels is a non-trivial task. Here, we adopt a simple procedure which is based on the assumption that states at the lowest edge of the valence band are not affected by the presence of the edge in the material.

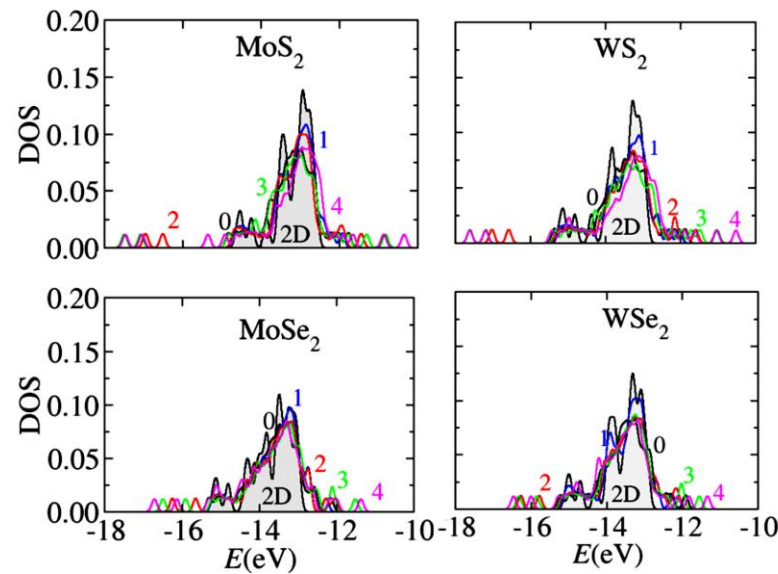


Figure 4.3.1.6: Density of states for bulk 2D MX₂ (grey shaded area) and the MX₂ nanoribbons (colored solid lines, with the same scheme as in Fig. 4.2.2). The energy range is within 4 eV of the low – energy peaks.

Our DOS calculations support this idea, as all of them possess identical peaks at low energies shown in Fig.: 4.3.1.6, regardless of edge structure and nanoribbon width. We shift the energy of electronic states of nanoribbons until those low-energy peaks are aligned with the corresponding peaks from the DOS of the 2D bulk. To make the comparison as accurate as possible, we recalculate the DOS of the 2D bulk using an identical unit cell with the same number of atoms and dimensions as in the case of nanoribbons with width $n_c = 6$ and metal-terminated edge. We chose the shift of energies so that the average error from these peaks is minimized. With this alignment, we find that the position of the Fermi level of the nanoribbons is always lower in energy compared to that of the single layer bulk (see Fig. 4.3.1.7).

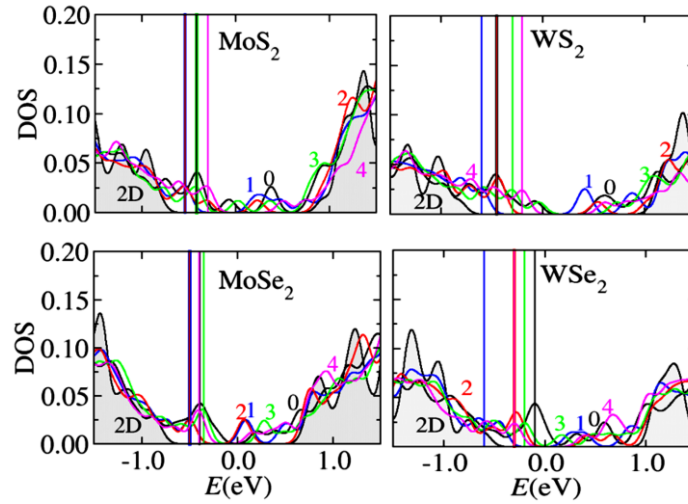


Figure 4.3.1.7: Density of states for bulk 2D MX₂ (grey shaded area) and the MX₂ nanoribbons (colored solid lines, with the same scheme as in Fig. 4.2.2). The energy range is within 1.5 eV of the mid-gap point, which is set to zero, the Fermi levels of the nanoribbons are shown with color-coded vertical lines.

All nanoribbons have Fermi levels that lie inside the gap of the 2D bulk, which establishes the metallic character of the zig-zag edges of TMD nanoribbons, due to the edge states. In all structures, with $N_x = 2$ chalcogen adatoms and for a width of $n_c = 6$, the nanoribbon Fermi level is pinned at about -0.3 eV to -0.5 eV below that of the 2D bulk, for all materials. A complete table of the Fermi level of the 1D nanoribbons is given below:

	MoS ₂ E _F shift in (eV)	MoSe ₂ E _F shift in (eV)	WS ₂ E _F shift in (eV)	WSe ₂ E _F shift in (eV)
0	-0.42	-0.40	-0.45	-0.10
1	-0.60	-0.50	-0.60	-0.45
2	-0.54	-0.50	-0.45	-0.30
3	-0.42	-0.35	-0.30	-0.20
4	-0.30	-0.40	-0.20	-0.30

Table 4.3.1: Pinning of Fermi Level of MX₂ nanoribbons of a width of 6 unit cells ($n_c=6$) with respect to single layer.

4.3.2 Band structure

Fig. 4.3.2 shows the band structures for TMD nanoribbons of width $n_c = 6$. The energies are given relative to the Fermi level of the 2D bulk. In all plots, the projection of the underlying band structure of the 2D bulk is shown as a shaded area. The gap is direct, as the two extrema occur at the same k -point which lies at $2/3$ of the distance from Γ to X, the edge of the 1D Brillouin Zone. Table 4.3.2 presents a comparison of the energy gaps of the 2D TMD monolayers as derived from our calculations to previous DFT study (ref. [10]), showing the good agreement between the two calculations.

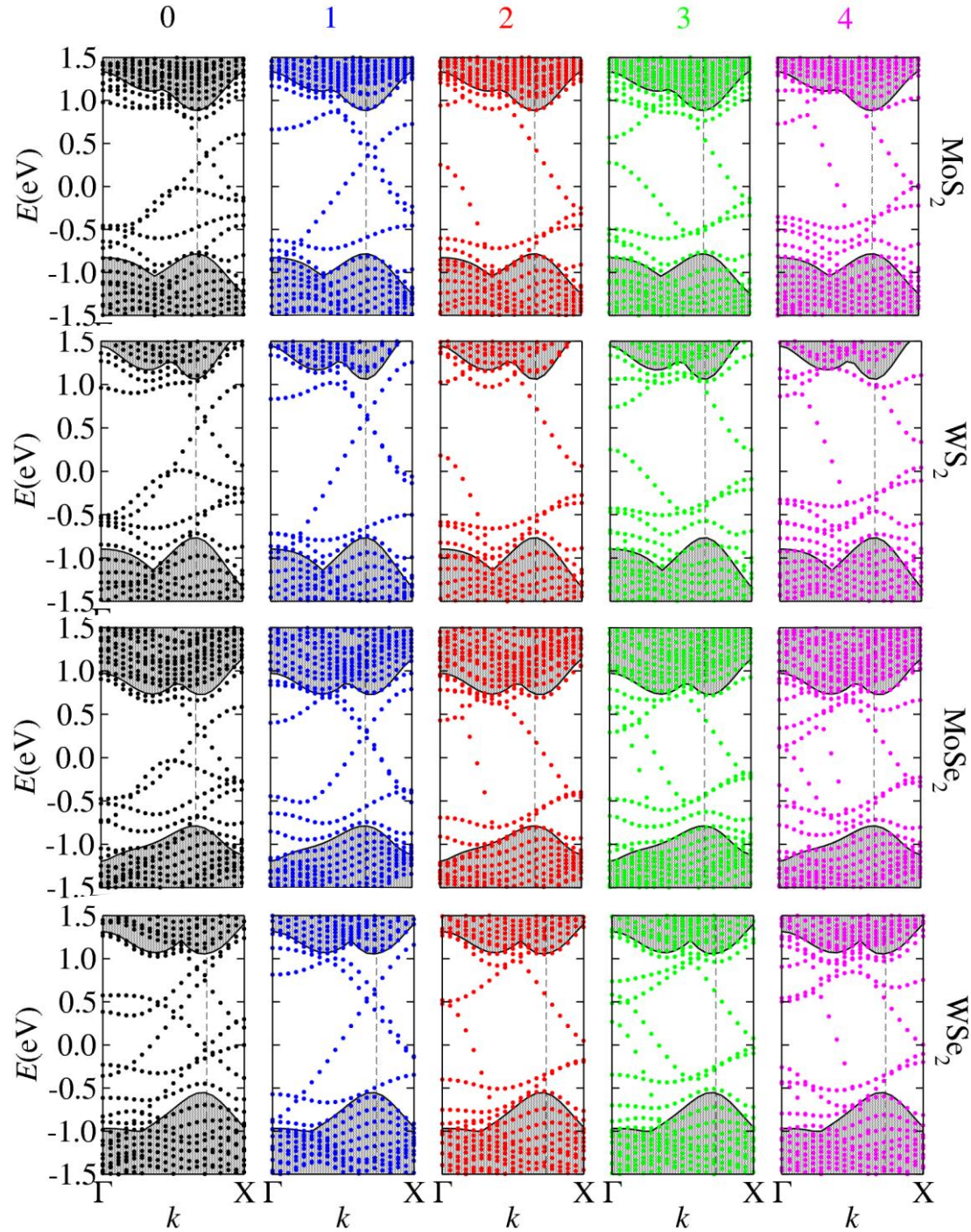


Figure 4.3.2: Band-structures of the TMD nanoribbons of width $n_c = 6$ and different number N_x of chalcogen adatoms along the zig-zag edge. The grey filled area shows the bandstructure of the 2D bulk in each case. The zero of the energy scale is set to the Fermi level of the ideal single-layer. The dashed vertical line indicates the K point of the BZ.

	E_g (eV) 2D	E_g (eV) 2D [10]
MoS₂	1.76	1.69
MoSe₂	1.56	1.51
WS₂	1.96	1.85
WSe₂	1.69	1.63

Table 4.3.2: Comparison of the values of the energy gaps of 2D TMDs as derived from our calculations (left column) and theoretical research as obtained from reference [10] (right column).

The point where the direct gap occurs corresponds to the K point of the Brillouin zone for the 2D hexagonal structure, due to folding from the definition of the primitive vectors of the unit cell, as shown in Fig. 4.1. In all cases, the band gap of the 2D material is crossed by several bands which are not flat, as one might have expected for localized defect states. These states correspond to metallic character, describing electrons that move in one-dimensional Bloch states along the edge.

4.3.3 Wavefunction visualization of the metallic states

It has been well established that TMD nanoribbons show metallic behavior. From the bandstructure calculation we observe two metallic states in the case of Sulfides and three in Selenides. Also the behavior of these states from these plots, suggested a localization. In this section we locate the metallic states and visualize their wavefunctions. We find that the metallic character is highly localized at the edge of the nanoribbons at a width of approximately 5 Å. Figure 4.3.3 shows the electron wavefunctions for the highest occupied (down) and lowest unoccupied (up) states at the Γ point of the Brillouin zone. The same behavior is observed in all metallic states and points of the Brillouin zone. However, depending on the selected k point the states can be found either at the upper edge or the lower.

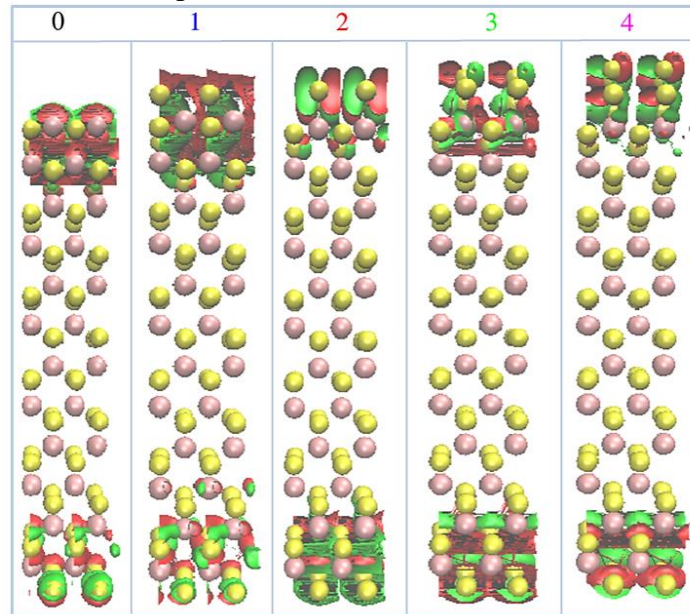


Figure 4.3.3: Wavefunction visualization of two metallic states in MoS₂ nanoribbons with different number of S adatoms. In this typical example, the HOMO state is found at the lower edge of the nanoribbon, while the LUMO at the upper edge. In all figures metal atoms are shown with pink color, while yellow atoms represent the chalcogens. Red and green colors correspond to the negative and positive isovalues of the wavefunction respectively.

From the wavefunction visualization we confirmed that the metallic states are localized at the edge. This method although it offers quite an insight in the electronic structure of transition metal dichalcogenide nanoribbons, it is however only a qualitative study in regard to the width of the metallic states. A more accurate calculation of the metallic region width will be presented in chapter 5.

4.3.4 Edge energy of TMD nanoribbons

The key quantity that determines the stability of nanoribbons, relative to the bulk 2D layer, is the edge energy, γ . This is the one-dimensional analogue of surface energy (surface tension), that is, the energy per unit length needed to cleave the material. A 2D material in vacuum is expected to have $\gamma > 0$, as it costs energy to break chemical bonds and create an edge. For a 2D material in equilibrium with an active compound, the edge energy will be different, as new bonds can be formed between edge atoms and atoms of molecules coming from the reservoir. By applying a general formula for the solid-gas interfacial tension [93,94], we can write:

$$\gamma = (\gamma_0 - E)/L \quad (1)$$

where γ is the edge energy in vacuum, E is the average energy of any new bonds that are formed and L is the average distance between such new bonds. From Eq.:(1) it is clear that γ could be either negative or positive, depending on the strength and density of the bonds between edge atoms and atoms/molecules of the reservoir. A negative value of γ means that the ripping of the material and formation of edges is an exothermic process, whereas ripping of the material is endothermic for $\gamma > 0$.

The edge energy, γ , is defined in a similar way as the surface energy of 3D materials: A nanoribbon made of MX_2 has total energy

$$E_{tot} = 2n_c E_{MX_2} + N_X \mu_X + 2\alpha\gamma \quad (2)$$

where E_{MX_2} is the energy of the monolayer per MX_2 unit, $2n_c$ is the number of MX_2 units along the \hat{y} direction, N_X is the number of chalcogen adatoms at the reconstructed edge and μ_X is the chemical potential of the chalcogen X. The last term is the energy cost associated with the formation of the two edges, which is proportional to the length of the unit cell along \hat{x} , α and the edge energy, γ . The edge energy is calculated by plotting E_{tot} as a function of n_c and then using a least-square method to fit a straight line to the calculations [22].

The chemical potential μ_X of chalcogen X (S or Se) is an important parameter that links the theoretical modeling to experimental conditions. In principle, the nanoribbons are in equilibrium with a reservoir of X atoms, and μ_X is the energy required to take one X atom from this reservoir. No matter what the X-containing compound is, μ_X cannot be greater than the energy of an isolated X atom (where the atom has no chemical bonds), and it cannot be lower than the energy of the solid bulk form of X, which is the preferred state of X at standard conditions. In order to establish reliable values for the chalcogen chemical potentials, we investigate the cohesive energy of their bulk structures. Chalcogens have some of the most complicated crystal structures for elemental solids [84]. A full DFT study of these structures is a demanding project in itself, beyond the scope of the present work. We limited ourselves to calculations of metastable structures that are simpler than the standard bulk forms of the chalcogen materials, while maintaining the same local environment around each chalcogen atom as in the bulk. Both chalcogens prefer to form structures with two-fold coordination, where rings of atoms are arranged periodically in space. The rhombohedral structure of S is modelled using a hexagonal unit cell that contains three rings of six S atoms. The structure of α – monoclinic Se has a unit cell that contains four eight-membered rings. We consider the cohesive energy of S and Se in these model structures, which is

the difference in energy between an isolated atom and an atom in the solid. We compare these values to the atomization energies of these materials [86]. The calculations are in excellent agreement to experimental data: the cohesive energy of S is found to be 2.82 eV (experimental value is 2.87 eV) while that of Se is found to be 2.43 eV (experimental value is 2.35 eV). This comparison establishes that our assumptions for the chalcogen chemical potentials are very reasonable.

The results for the dependence of the edge energy on the chemical potential of chalcogens are shown in Fig. 4.3.5. For purposes of comparison between the four materials we present the same range for the chalcogen chemical potential, starting at the bulk value. We give the chalcogen chemical potential with reference to the value of a chalcogen atom at zero pressure and temperature, and we indicate the values corresponding to the respective bulk elemental solids. The experimentally relevant region is the range of values larger than those limiting values. In chemical compounds of chalcogens (such as alkanethiols), X forms the same number of covalent bonds as in solid X, and should have similar energy (although somewhat higher than in its standard form).

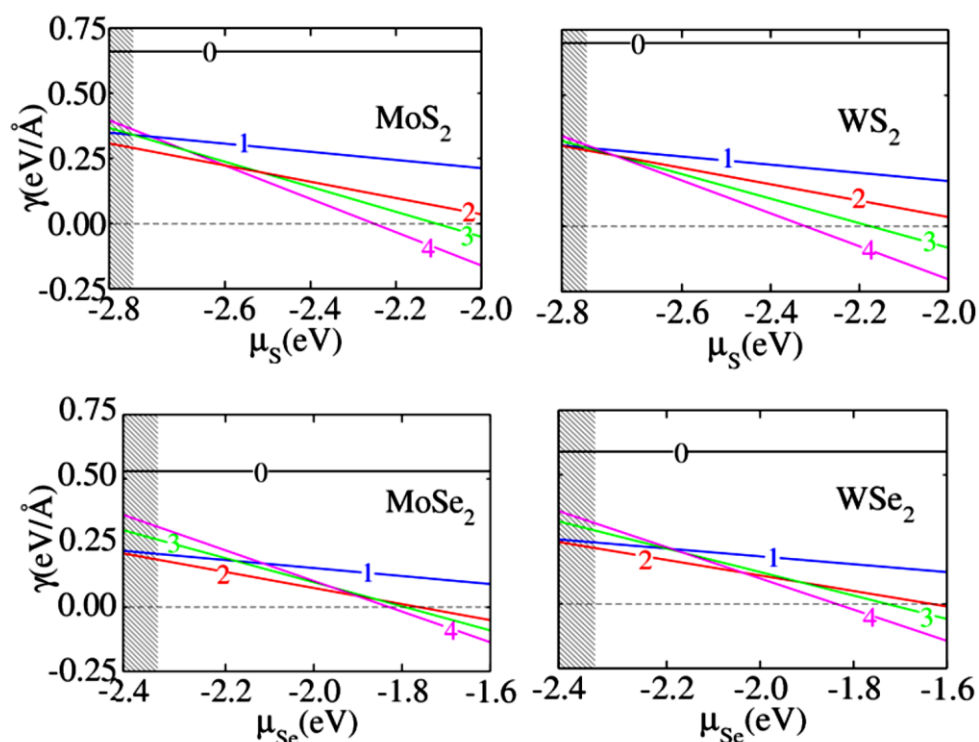


Figure 4.3.4: Edge energies, γ , of MX₂ nanoribbons with different number of adatoms, as a function of the chalcogen chemical potential, μ_X relative to the chemical potential of atomic X (M=Mo, W; X=S, Se). Different colors correspond to different number of adatoms, as in Fig. 4.2.2. The shaded vertical column indicates the range of values of the bulk chalcogen chemical potential. For S adatoms, the lower value is the experimental result, the upper value the theoretical result, while the opposite is the case for Se.

Depending on the value of the edge energy, we expect that when a single layer of a TMD material is exposed to a chalcogen environment, it will either remain intact ($\gamma > 0$) or, when $\gamma < 0$, the structure will be unstable. For all four materials, we find that $\gamma < 0$ when $\mu_X \sim 0$, the limit at which X atoms can lower their energy by leaving the gas phase and become incorporated into the TMD edge. For this reason, the structure with the largest possible number of chalcogen atoms (in our study $N_X = 4$) is always favored for high values of μ_X . Moreover, γ is negative in all cases when the chemical potential is about 0.5 eV above the energy of the solid. This means that edges will be formed spontaneously if the 2D material is at equilibrium with compounds where the chalcogen atoms are weakly bound. On the other hand, $\gamma > 0$ for chalcogen chemical potential near that of the solid phase, which means that TMD layers

will be stable with respect to most sulfides and selenides, and are vulnerable to ripping only when in contact with atomic chalcogens or radicals.

The plots of Fig. 4.3.4 also reveal the favorable number of adatoms for each material, that is, the number N_X that corresponds to the lowest energy structure. The metal-terminated edge has energy that is significantly higher (by about 0.3 eV/Å) than the energy of any other edge, implying that stable 1D nanoribbon structures will be formed by attracting chalcogen atoms at the zig-zag edge, once they are exposed to an external source. In the case of solid S or Se reservoirs, the preferred number of adatoms at the reconstructed edge is $N_X = 2$ for all four materials. For MoS₂ in particular, our findings are in excellent agreement to experiments that found complete absence of M-terminated edges and preference for edges terminated by S dimers [15]. For higher values of the chemical potential, the preferred amount of adatoms at the edge increases, as expected. In the case of atomic source, the edge energies of the nanoribbons is lowered by 0.3 eV/Å to 0.4 eV/Å per extra adatom. Only the structures with $N_X = 2$ or 4 are stable, since other terminations of the nanoribbons have higher energy at any value of the chemical potentials.

We conclude from this analysis that stable nanoribbon edges will have termination consisting of 2 chalcogen adatoms for chemical potential values close to the bulk chalcogen phases, or 4 chalcogen adatoms for chemical potential values higher than the bulk phase (by 0.1 - 0.2 eV for S compounds and by 0.3 - 0.5 eV for Se compounds); under no plausible conditions the edges will have metal-atom termination.

4.4 Conclusion

We performed a systematic set of first-principles calculations for TMD nanoribbons of four different materials (MoS₂, MoSe₂, WS₂ and WSe₂), of width between 5.5 Å and 42 Å, with edge structure containing various amounts of chalcogen X atoms, $0 \leq N_X \leq 4$, attached to the metal-terminated edge. We examined the thermodynamic stability of these nanoribbons at equilibrium with different chalcogen reservoirs. We find that nanoribbons with $N_X = 2$ adatoms are most stable with respect to the bulk chalcogen phase or stable molecules like thiols, while $N_X = 4$ is favored when weakly-bound chalcogen compounds are available.

While the 2D materials are semiconductors, TMD nanoribbons with zigzag edges are always metallic regardless of the composition, the width or the edge structure. The Fermi level of the metallic phase is always lower in energy than the Fermi level of the 2D bulk, thus making it favorable for electrons to occupy these metallic states. The bands of the edge states are one-dimensional Bloch states with large dispersion, extending across the band gap of the 2D layer. The presence of edge metallic states in a 2D bulk semiconductor, common to all the cases considered here, with bands crossing the gap and states that are stable against chemical modification of the edges, led to the suggestion [22] that TMD nanoribbons could be candidates for topological insulator behavior.

CHAPTER 5

Edge states in TMDs

Chapter 5

Edge states in TMDs

5.1 Introduction to the Shockley model

Although, in the previous chapter we established through multiple calculations the presence of metallic edges in TMDs, we have not yet been able to identify the factor that is responsible for these states. In this section of our research we refer to the Shockley theory [95] in order to study the physics of the metallic edges.

In a periodic material, the electron wavefunctions are Bloch states:

$$\psi(\vec{r}) = e^{i\vec{k}\cdot\vec{r}} u(\vec{r}) ,$$

where \vec{k} is the wavevector and $u(\vec{r})$ a periodic function with the same periodicity as the potential in Schrödinger equation. In this way the electron wavefunction at all equivalent points at a distance equal to the lattice constant (R_n) can be described only by knowing the wavefunction of the basic unit cell:

$$\psi(\vec{r} + \vec{R}_n) = e^{i\vec{k}\cdot\vec{R}_n} \psi(\vec{r}).$$

If a perfectly periodic material is cut in two pieces and surfaces are formed, the Bloch's theorem is no longer valid. Although the majority of the electronic states resemble Bloch states far from the surface, which decay exponentially in the vacuum region, it is possible that some electrons will be localized at or near the surface. These quantum states that are qualitatively different from Bloch states are called surface states.

The concept of surface states was first proposed by I. Tamm in 1932 for one-dimensional solid and was revisited and generalized to 3D by W. Shockley in 1939 [95-98]. The two approaches give the same qualitative results. In a periodic system, when the periodicity is broken, solely that reason can lead to a change in the electron potential at the surface. According to Shockley, the electron potential for a semi-infinite 1D solid that occupies a region $y < y_0$, where y_0 is the location of the surface plane, presents a periodic behavior inside that crystal, followed by a potential step (W):

$$V(y) = \begin{cases} W, & y \geq y_0 \\ V_0 \cos\left(\frac{2\pi(y-y_0)}{a_0}\right), & y < y_0 \end{cases}, \quad (1)$$

where a_0 is the interatomic distance between atoms parallel to the \hat{y} -axis and V_0 and W are material – dependent constants. The electron potential in a semi-infinite chain along \hat{y} -axis is shown in figure 5.1.1.

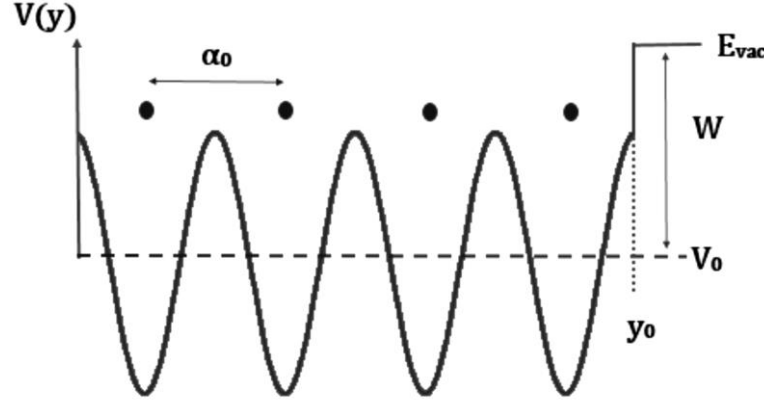


Figure 5.1.1: Electron potential for a semi-infinite chain along \hat{y} -axis. With horizontal dashed line the electron energy inside the crystal is shown, while E_{vac} corresponds to the energy in the vacuum region.

The wavefunctions of electron states inside the 1D chain form a linear combination of two Bloch states (one for each limit of the Brillouin zone) that vanish deep inside the crystal and present a rapid exponential decay in the vacuum region. The wavefunction of the surface state decays exponentially on both sides of the surface and is described by four parameters (q , k , A , B) according to:

$$\psi(y) = \begin{cases} B e^{-q(y-y_0)}, & y \geq y_0 \\ A e^{k(y-y_0)} \cos\left(\frac{\pi(y-y_0)}{a_0} + \delta\right), & y < y_0 \end{cases} \quad (2)$$

The propability density of the localized state $p(y) = |\psi(y)|^2$, then presents a maximum at the position $y=y_0$ of the surface plane. Figure 5.1.2 presents a comparison of the behavior between Bloch and surface states (a) and the probability density of a Shockley surface state (b). For a three – dimensional material, $p(y)$ is the average probability over the other two coordinates:

$$p(y) = \iint |\psi(x, y, z)|^2 dx dz.$$

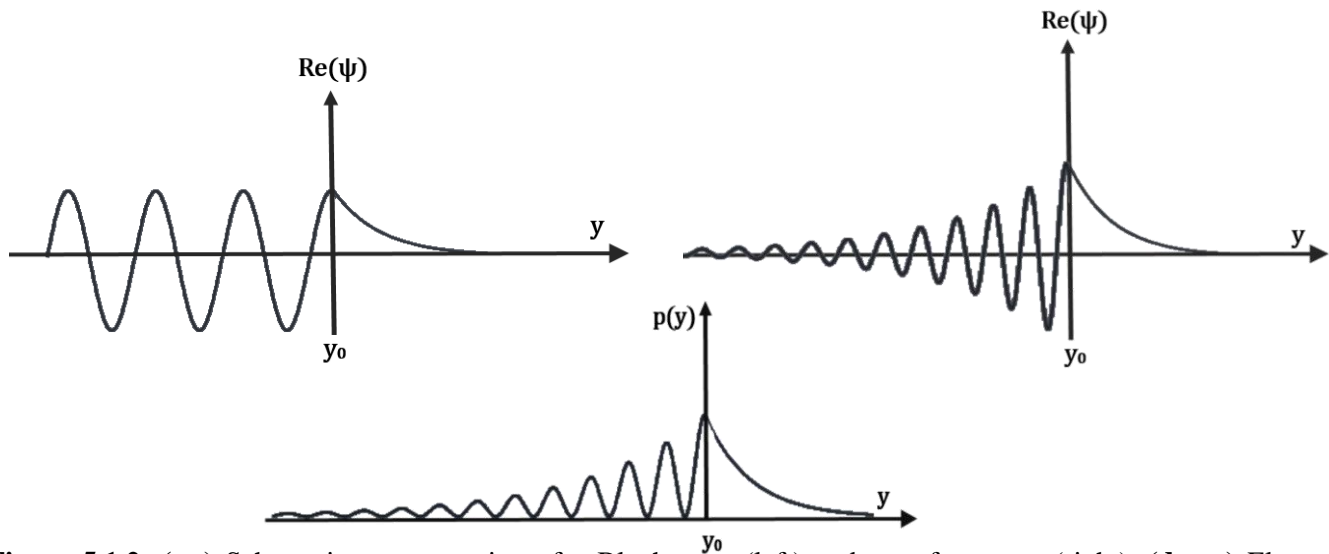


Figure 5.1.2: (up) Schematic representation of a Bloch state (left) and a surface state (right). (down) Electron probability density in a semi-infinite linear chain.

Assuming nearly-free electron model, i.e $W \gg V_0$, the workfunction corresponds to the energy required for the electron to be found in the forbidden area and is defined as the difference between the potential outside and inside the structure:

$$E_{vac} = \frac{\hbar^2 q^2}{2m} + E \implies W = E_{vac} - E = \frac{\hbar^2 q^2}{2m} \quad (3)$$

From equation (3) if we know the energy of the electron inside the crystal and the energy of the vacuum region we can conclude on the value of the wavenumber q from the workfunction and use it to describe the electron probability density in the vacuum region. To draw a full description and extract the remaining parameters of the wavefunction of the surface state, however, one has to consider the two continuity criteria for the wavefunction and the first derivative, where:

$$\lim_{y=y_0} \psi_A = \lim_{y=y_0} \psi_B \quad \text{and} \quad \frac{d\psi_A}{dy} \Big|_{y=y_0} = \frac{d\psi_B}{dy} \Big|_{y=y_0} \quad (4)$$

5.2 Results and discussion

We would like to find whether the metallic states we see in 1D TMD nanoribbons are in agreement with the Shockley model and are present due to the broken periodicity of the system along the finite \hat{y} direction. For that study we focus on the most stable structures, i.e. the nanoribbons with the two chalcogen adatoms, and we perform calculations for the electron potential along the nanoribbon. We then locate the true surface states and calculate the probability density along the \hat{y} axis for their Kohn–Sham wavefunctions. Finally, in order to find if the behavior of the probability density is described by the Shockley theory (eq.:2) we draw a non-linear curve fit and we conclude on the parameters of the electron wavefunction of the Shockley surface state.

In the following graphs (Fig.:5.2.1) we present the electron potential for quasi 1D TMD nanoribbons with two chalcogen adatoms as a function of the atom positions along the \hat{y} axis. For this calculation we find the electron potential throughout the whole structure and then get the average values in the \hat{x} and \hat{z} directions in order to project to electron potential behavior along the atoms positions in finite direction of the nanoribbon \hat{y} . As expected, a cosine-like behavior is observed, followed by a potential step at the edges of the structures. Comparing our workfunction graphs to the atom positions we find that the electron potential local minima are found around the chalcogens. This finding is explained by the much larger electronegativity of the chalcogens as opposed to the metal atoms (see Fig.: 5.2.3). Also, inside the nanoribbons we find that the electron – potential minima and maxima close to the upper edge where the chalcogen adatoms are found, differ from the inner structure. This result is expected since the optimum positions of the adatoms are not mirrored to the lowest edge chalcogens, leading to different edge formation. The non-symmetric structure however does not affect much the energy in the two vacuum regions where the calculated values for E_{vac} differ at the second decimal point (see table. 5.2.1).

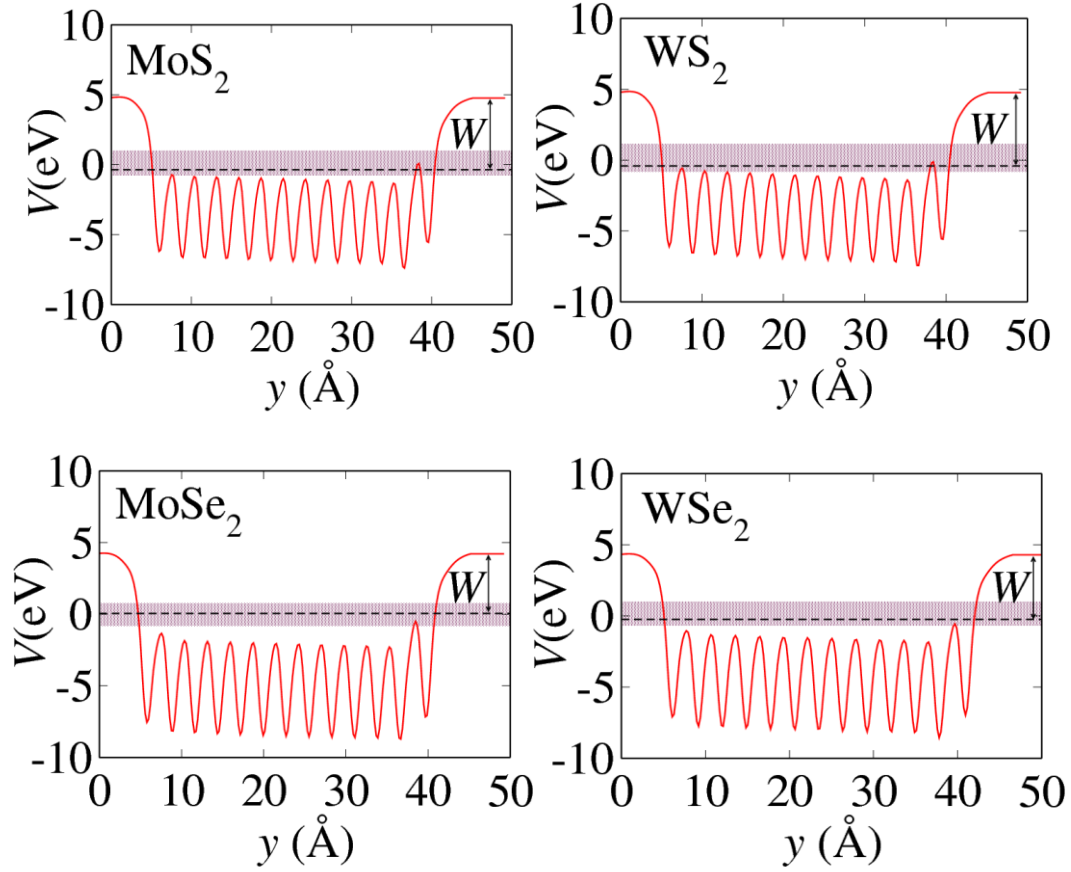


Figure 5.2.1: Graphical representation of the electron potential for quasi 1D TMDs of a width of six unit cells ($n_c=6$) and two chalcogen adatoms at the metal terminated edge (red curves). In all figures, the shaded areas show the energy gap of the corresponding 2D materials while the dashed lines present a metallic state. The Fermi level of the 2D materials is set a zero eV. With W we show the workfunction.

Table 5.2.1 presents our results for the energy in the vacuum regions left and right (in respect to the electron potential graphs) of the nanoribbons.

nanoribbon	E_{vac} (eV) left	E_{vac} (eV) right
MoS ₂	4.791	4.770
WS ₂	4.787	4.767
MoSe ₂	4.248	4.217
WSe ₂	4.321	4.294

Table 5.2.1: Vacuum energies for TMD nanoribbons of a width of six unit cells ($n_c=6$) and two chalcogen adatoms at the metal terminated edge.

As described in equation (3) of the introduction section, the workfunction is the energy of the vacuum region minus the energy of the electron inside crystal. In order to calculate the workfunction of each structure we first locate the metallic edge states. For the case of sulfides we find two edge state

which correspond to the highest occupied (113) and lowest unoccupied (114) states, while in the case of selenides an extra metallic state is observed. Appendix presents electron probability density calculations for all the structures mentioned in chapter 4.

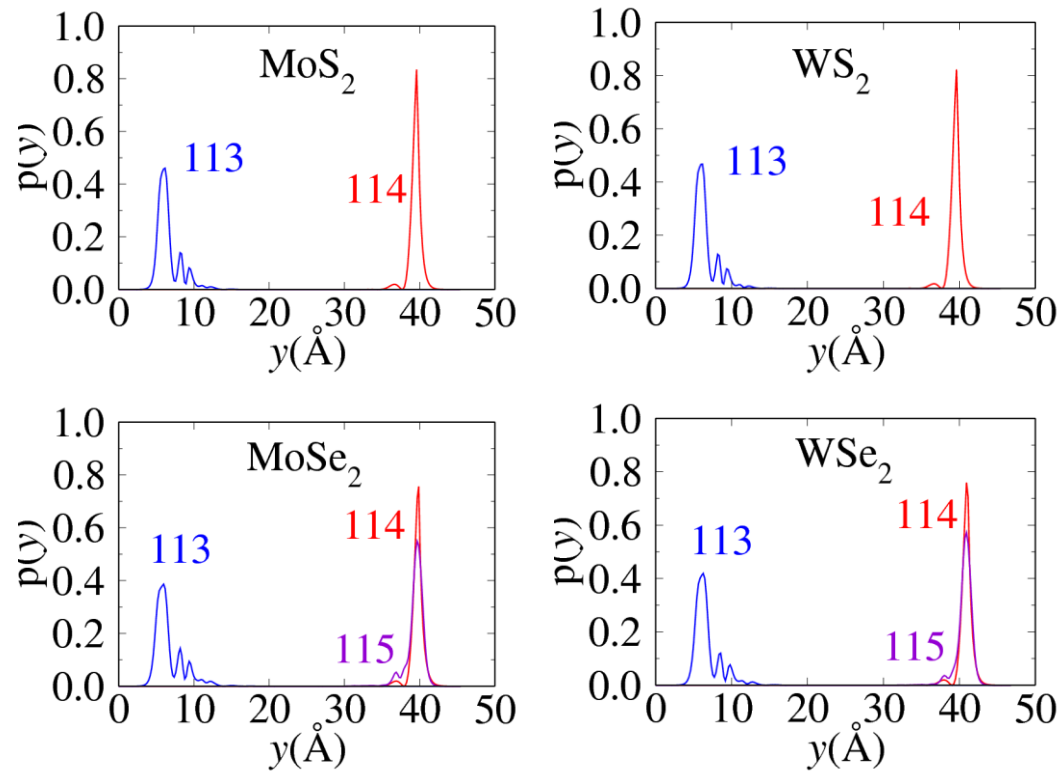


Figure 5.2.2: Graphical representation of the probability density curves for the metallic edge states in TMD nanoribbons as a function of the atom positions along the finite \hat{y} axis. Different number notations correspond to the different energy levels. HOMO (113) and LUMO (114) are shown by blue and red curves respectively.

Figure 5.2.2 shows the direct calculations for the probability density curves of the metallic states, as a function of the atom positions along the \hat{y} axis. From the graphs, we see that the metallic states can be found in either of the two edges of the nanoribbons and present the same localization width. However in our workfunction calculation we will choose to use the LUMO state which is the one with the highest probability density exactly at the edge (114) and we will consider the E_{vac} for the right side of the nanoribbon. From now on we will refer to this metallic state as the Shockley state (E_s). We rewrite equation (3) for the Shockley state:

$$W = E_{vac} - E_s = \frac{\hbar^2 q^2}{2m} \quad (5)$$

Table 5.2.2 presents our results for the energy in the vacuum region the energy of the Shockley state and finally the workfunction. The electron potential of TMD nanoribbons zoomed at a region close the edge, along with the atom positions is shown in figure 5.2.3.

nanoribbon	E_{vac} (eV)	E_s (eV)	W (eV)
MoS₂	4.770	-0.359	5.129
WS₂	4.767	-0.413	5.180
MoSe₂	4.217	0.060	4.157
WSe₂	4.294	-0.245	4.539

Table 5.2.2: Workfunction for quasi 1D TMD nanoribbons.

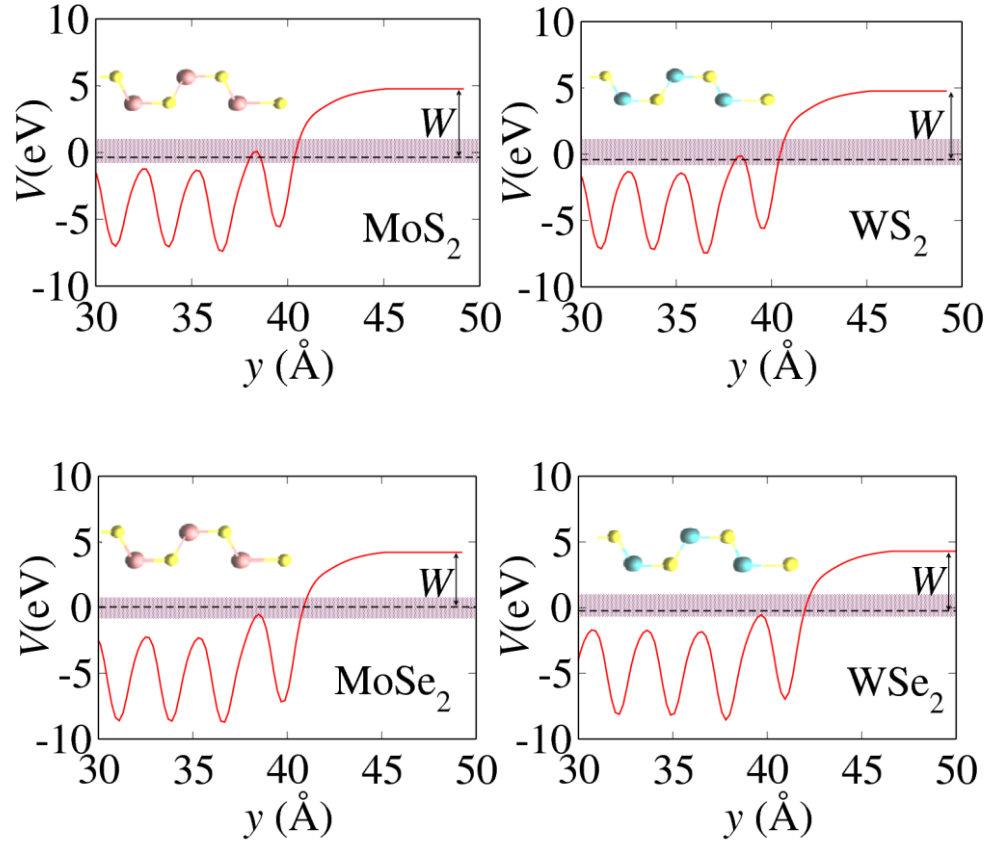


Figure 5.2.3: Workfunction graphs zoomed at the upper edge of the TMD nanoribbons, where the highest electron probability density is found. The nanoribbon structures parallel to the \hat{y} axis are presented in ball-and-stick model. With pink and cyan we show the Mo and W atoms respectively, while yellow atoms correspond to the chalcogens.

The probability density curve for a semi-finite at the \hat{y} direction nanoribbon is described by:

$$p(y) = \begin{cases} B e^{-2q(y-y_0)}, & y \geq y_0 \\ A e^{2k(y-y_0)} \cos^2\left(\frac{\pi(y-y_0)}{a_0} + \delta\right), & y < y_0 \end{cases} \quad (6)$$

By substituting the energies from table 5.2.2 to equation (3) we can now extract the value of the wavenumber q . Also from the two continuity criteria given in equation (7) we conclude on two conditions regarding the remaining parameters A , B , k and d .

$$B = A \cos d \quad \text{and} \quad k = \frac{\pi}{\alpha_0} \tan d - q \quad (7)$$

For the final step of this study we perform a non-linear curve fit of equation (6) to the direct calculation of the probability density. Using the calculated value of q and the conditions in equation (7) we are able to minimize the number of needed fitting parameters to the four A , k , d and y_0 instead of seven. A list of all the parameters used in the fit of equation (6) is given in table 5.2.3.

nanoribbon	q (\AA^{-1})	k (\AA^{-1})	d (rad)	A	B	α_0 (\AA)	y_0 (\AA)	y_0^p (\AA)
MoS₂	1.16	0.60	0.338	0.96	0.91	3.193	39.639	39.518
WS₂	1.17	0.61	0.365	0.96	0.90	3.197	39.557	39.543
MoSe₂	1.04	0.59	0.295	0.87	0.83	3.203	39.832	39.763
WSe₂	1.09	0.57	0.329	0.91	0.86	3.311	41.056	40.945

Table 5.2.3: Values of the parameters describing the probability density. The parameters that were allowed to fit during the calculation are k , y_0 , d and A . y_0^p refers to the position of the edge adatoms from the direct structure optimization calculation.

Figure 5.2.4 presents the non-linear curve fit of the probability density zoomed at the upper edge of the TMD nanoribbons. From the graphs we find that the direct calculation of the probability density of the edge localized metallic states (black dots) is in good agreement with the Shockley theory (red curve). Also we conclude on the localization width which in all cases is approximately 5.5\AA while from 5.2.3, we see that the periodicity width of the peaks is exactly one unit cell (α_0) and the maximum probability density is found exactly at the position of the edge chalcogen adatoms (comparison between fitted y_0 and real position y_0^p).

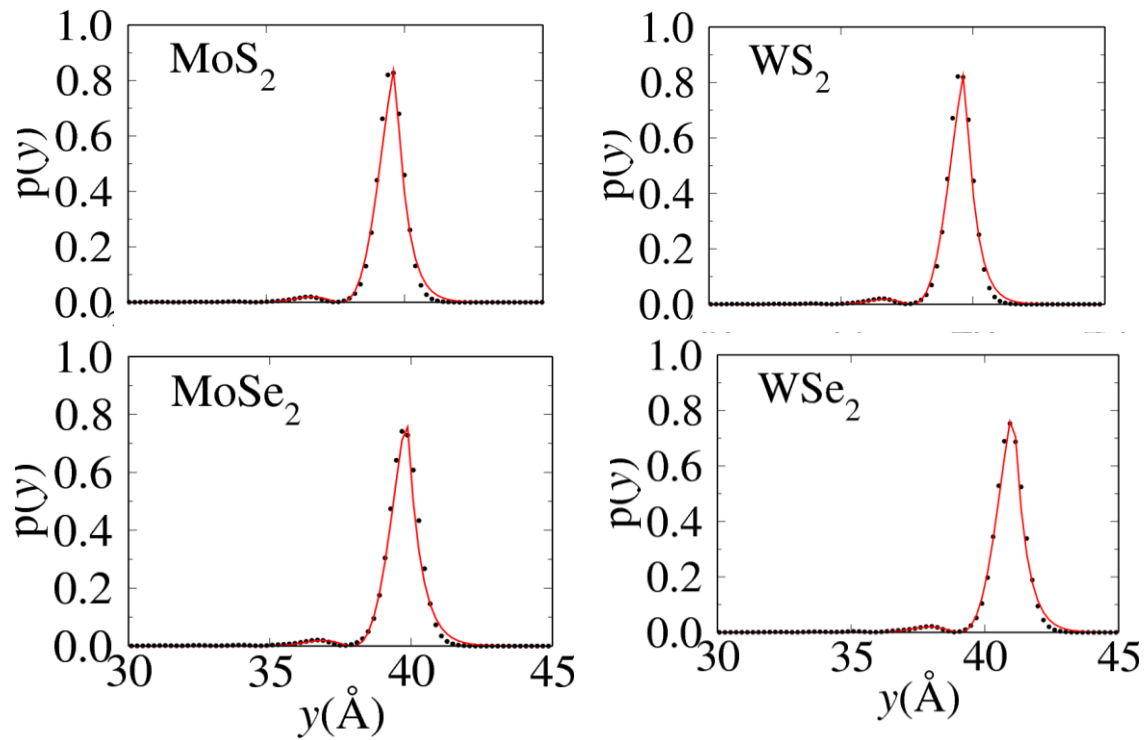


Figure 5.2.4: Non-linear curve fit of the probability density for the upper edge Shockley states in TMD nanoribbons. With black dots we present the direct calculation, while red curves show the fit.

5.3 Conclusion

In chapter 4 we established the presence of metallic character in all four most common TMD nanoribbons (MoS_2 , MoSe_2 , WS_2 and WSe_2), regardless of width, composition or edge reconstruction and we found that the metallic states are highly localized at the edges. Here we aimed to determine the reason for the localization of these states and we performed calculations for the workfunction and the probability density for TMD nanoribbons of a width of six unit cells.

We found that the probability density of the edge localized metallic states in TMD nanoribbons is in agreement with the Shockley theory. We concluded that in all TMDs the factor that is responsible for the presence of the metallic states is the broken periodicity of the material as we move to lower dimension from 2D monolayer to quasi 1D nanoribbon.

Although Shockley theory was developed to describe surface states in three – dimensional semiconductors, it can perfectly describe edge states of two – dimensional semiconductors as well. To our knowledge this is the first application of Shockley theory to a two – dimensional material.

CHAPTER 6

**TMD nanoribbons with
adsorbed oxygen and
hydroxyl**

Chapter 6

TMD nanoribbons with adsorbed O and OH

6.1 Introduction

In chapter 4 we have shown that TMD nanoribbons (such as: MoS₂, WS₂, MoSe₂, WSe₂) with zig-zag edges, when in a chalcogen rich environment, will attract two Sulfur or Selenium adatoms at the metal-terminated edge creating a robust structure. As opposed to the 3D and 2D semiconducting structures, quasi 1D nanoribbons present a strong localization (~ 5.5 Å) of metallic character around the edges. Also, there has been intense interest for application of TMD nanostructures in complex chemical reactions such as hydrogen/oxygen evolution reactions (HER/OER or CO₂ reduction [23,39-40,98-109].

In this chapter, we simulate TMD nanoribbons with Oxygen and Hydroxyl adsorbed at the edges, focusing on the adsorption energy as well as electron density of states and band – structure. We compare our results to the pristine and oxidized 2D monolayers. First, we focus on the relaxed structure of (1x6) MoS₂ nanoribbon. We introduce Oxygen atoms to our structure either by adsorption in various sites at the Sulfur saturated edge or by substitution, and we calculate the adsorption energy in order to find the most probable edge conformation. Due to the fact that we use periodic boundary conditions in the case of substitution we can only perform calculation for the 50% and 100% substituted nanoribbons. We find that the optimum Oxygen adsorption site is on top of each Sulfur atom. This geometry is then used for the rest materials (WS₂, MoSe₂, WSe₂) and for the calculation of the electronic properties. The same procedure is repeated for TMDs with Hydroxyl groups. Figure 6.1 represents the three main structures after optimization.

Finally, we create (2x6) supercells for the TMDs. We perform the same study for 50% adsorbed Oxygen atoms and Hydroxyl radicals and we compare our results to the 100% covered structures.

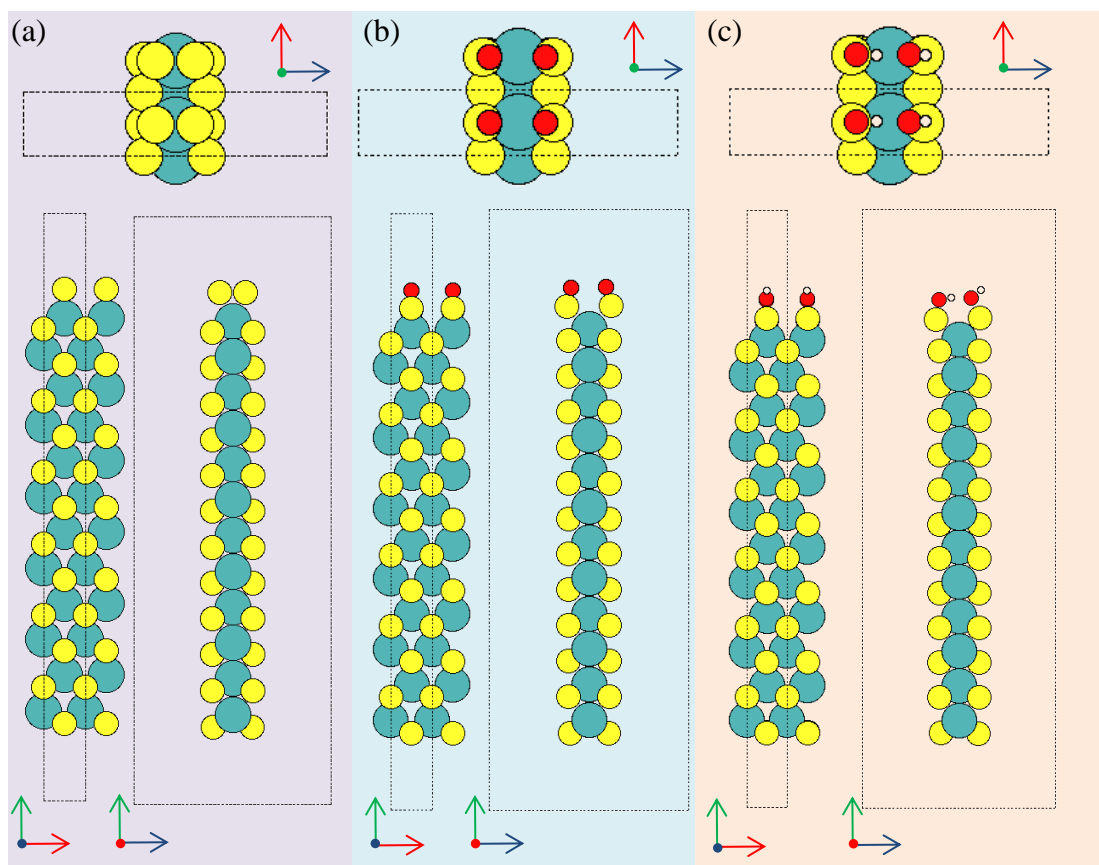


Figure 6.1: Ball – stick models of TMD nanoribbons after structure optimization. **(a)** Sulfur – saturated structure. **(b)** Nanoribbon with two Oxygen adatoms. **(c)** Nanoribbons with two adsorbed Hydroxyl groups. In all figures, we show the nanoribbons from three different viewpoints x,y,z (red, green and blue respectively). The supercell used in our calculations is presented by the dashed box in all figures.

6.2 Adsorption and substitution of Oxygen on MoS₂ nanoribbons.

In this section we perform structure optimization and adsorption energy calculations for MoS₂ nanoribbon which either undergoes Sulfur substitution by Oxygen atoms, or simply attracts Oxygen atoms on various edge sites. Figures 6.2.1 and 6.2.2 present the six possible Oxygen sites. In the case of Oxygen addition at a hollow site we present both the initial and the final sites and we see that the atom will move to a much a preferable position at a bridge site noted as p7.

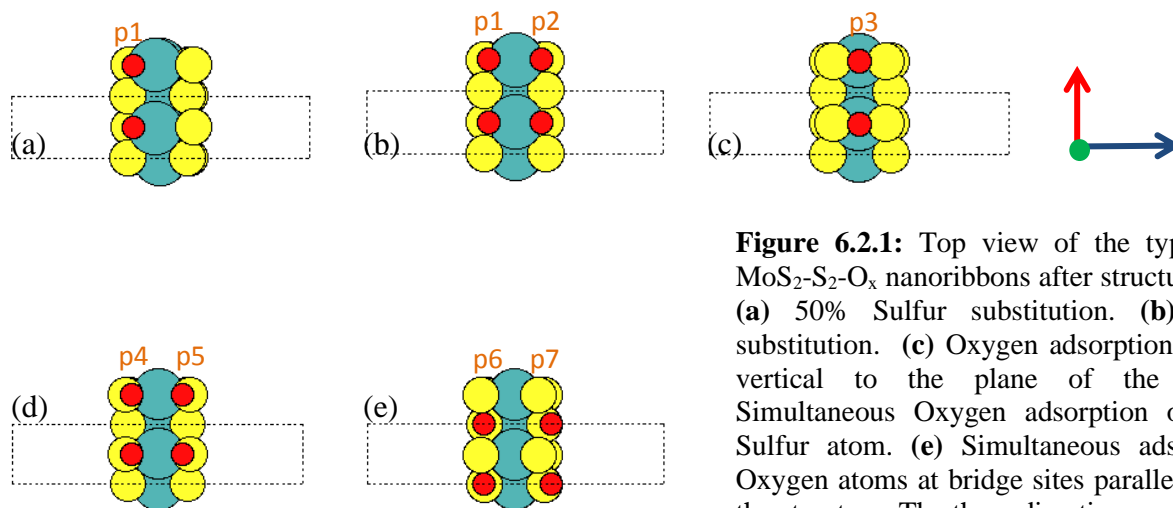


Figure 6.2.1: Top view of the typical models of MoS₂-S₂-O_x nanoribbons after structure optimization. **(a)** 50% Sulfur substitution. **(b)** 100% Sulfur substitution. **(c)** Oxygen adsorption at a bridge site vertical to the plane of the structure. **(d)** Simultaneous Oxygen adsorption on top of each Sulfur atom. **(e)** Simultaneous adsorption of two Oxygen atoms at bridge sites parallel to the plane of the structure. The three directions x,y,z are presented by red, green and blue arrows respectively.

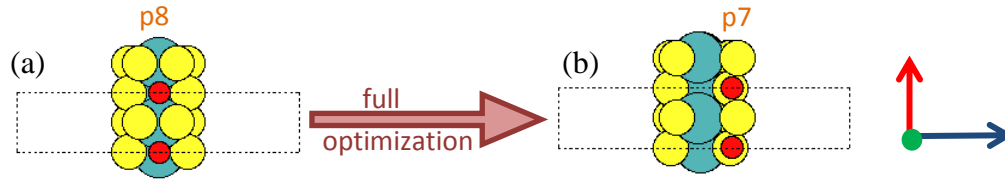


Figure 6.2.2: Top view of MoS₂-S₂-O nanoribbon with Oxygen adsorption at a hollow site before (a) and after (b) structure optimization.

In order to conclude on the most preferable structure, we calculate for each nanoribbon the energy of adsorption or substitution. The thermodynamic stability of the structures is dependent on the individual formation energies as described by equations (1) and (2) for the cases of substitution and adsorption respectively.

Energy of O substituted MoS₂ nanoribbon:

$$E_{sub} = \frac{1}{n} (E_{1D,O_n} - E_{1D} - \frac{n}{2} E_{O_2} + nE_S) \quad (1)$$

Energy of O adsorbed MoS₂ nanoribbon:

$$E_{ads} = \frac{1}{n} (E_{1D,O_n} - E_{1D} - \frac{n}{2} E_{O_2}) \quad (2)$$

Where n is the number of adsorbed/substituted atoms and E_{1D,O_n} , E_{1D} , E_{O_2} and E_S are the total energies of oxidized nanoribbon, the initial nanoribbon, the molecular Oxygen and the energy of solid S per atom, respectively. Table 6.2.1 presents the results for the energies corresponding to each of the MoS₂-S₂-O_x nanoribbons. However, before we proceed we should clarify that for Sulfur and Oxygen atoms we needed to perform additional potential energy calculations for atomic S and molecular O₂ in a box, using a vacuum region of 6 Å around the system. The total energies for O₂ and solid S were found -11.40 eV and 2.82 eV respectively. Finally, the total energy of the MoS₂ nanoribbon with two Sulfur adatoms prior to the Oxygen adsorption (E_{1D}) is -262.997 eV.

O site/sites	Configuration	n	E_{1D,O_n} (eV)	E_{sub} (eV)	E_{ads} (eV)
P1	50% - sub	1	-263.638	2.239	-
p1,p2	100% - sub	2	-265.886	2.560	-
p3	Bridge vertical – ads	1	-268.215	-	0.482
p4,p5	On top – ads	2	-274.474	-	-0.077
p6,p7	Bridge parallel – ads	2	-273.620	-	0.388
p8	Hollow - ads	1	-267.307	-	1.390

Table 6.2.1: Formation energies of oxidized MoS₂ nanoribbons and energies of adsorption and substitution. Columns 1 to 3 present the parameters describing our structures.

From our calculations regarding the most thermodynamically stable oxidized MoS₂ nanoribbons we conclude that the preferable structure is the one with the adsorption of Oxygen atoms on top of each Sulfur edge atom. The geometrical characteristics of all oxidized TMD nanoribbons are given the next section.

6.3 Oxygen adsorption on TMD nanoribbons.

In the previous section we established that the most stable oxidized MoS₂-S₂ nanoribbon is the one with two Oxygen adatoms on top of each Sulfur edge atom. We now repeat the same procedure, for the other three TMD materials (WS₂, MoSe₂, WSe₂). Since our materials present similar electronegativities we do not expect any change in the structural behavior, thus a calculation for other Oxygen sitting sites is not required. Figure 6.3 presents ball – and – stick model of TMD nanoribbons of width $n_c=6$ with two Oxygen adatoms at the edge. For the geometric characteristics description we have selected specific atoms (noted as A,B,C,D) for which the resulting angles are given in table 6.3.

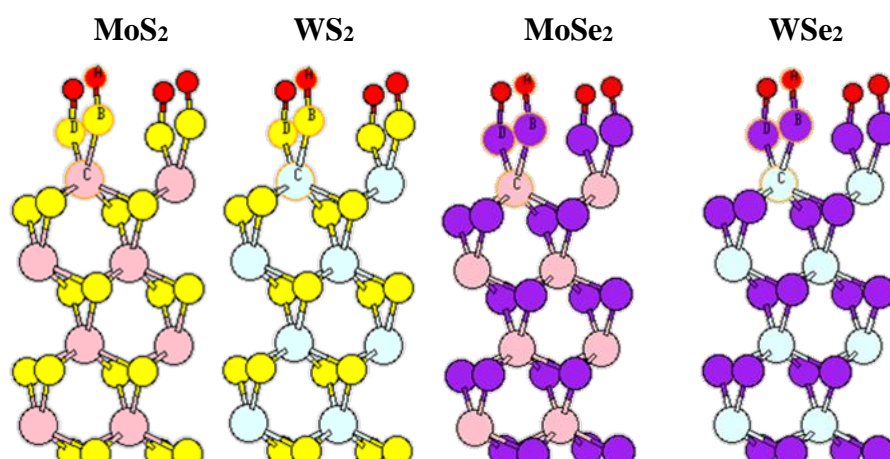


Figure 6.3: Ball-and-stick model of relaxed structures of oxidized TMD nanoribbons zoomed around the edge. In all figures the atoms are color coded in regard to the element. Mo and W atoms are shown with pink and cyan respectively, while yellow atoms represent Sulfur and purple Selenium. Red atoms correspond to Oxygens.

material	ABC (°)	BCD (°)	Torsion ABCD(°)
MoS ₂	121.67	88.73	0.00
WS ₂	122.73	87.37	0.00
MoSe ₂	119.88	86.87	0.00
WSe ₂	120.73	87.09	0.00

Table 6.3: Geometrical characteristics of the upper edge of oxidized TMD nanoribbons.

From the relaxed structures we see that the four edge atoms (2S, 2O) are found on the same plane, vertically to the plane of the nanoribbon, while the bond lengths between S-O and Se-O are 1.49 Å and 1.66 Å respectively. Although, from table 6.3.1 we see that the Oxygen-Chalcogen-Metal angle is close a

value most commonly found in planar trigonal geometries ($\sim 120^\circ$), the distance between for example S-O is in agreement with the value of uncoordinated sulfoxides [110] which present sp^3 hybridization. This suggests that even though sulfurides can be overcoordinated in this case the edge structure forms a more open bent tetrahedral geometry ($120^\circ > 109^\circ$). Also in all cases the distance between Oxygen atoms is over 2.7 \AA , much larger than the O-O single bond length (approximately 1.4 \AA) [111], showing that Oxygen atoms are undercoordinated and present a negative charge. This result is later confirmed by the large negative differential adsorption energies in the presence of Hydrogen (section 6.4) and the lowering of the Fermi level (section 6.5.3).

6.3.1 Electronic properties of oxidized TMD nanoribbons.

Following the same procedure as in the case of $\text{MoS}_2\text{-S}_2$ nanoribbon with two Oxygen adatoms at the “on top” site, from equation (2) in section 6.2, we calculate the adsorption energies for $\text{WS}_2\text{-S}_2\text{-O}_2$, $\text{MoSe}_2\text{-Se}_2\text{-O}_2$ and $\text{WSe}_2\text{-Se}_2\text{-O}_2$ nanoribbons. A complete table of the total and adsorption energies for all four materials is given bellow.

	$E_{1D,O_n} \text{ (eV)}$	$E_{1D} \text{ (eV)}$	$E_{ads} \text{ (eV)}$
$\text{MoS}_2\text{-S}_2\text{-O}_2$	-274.474	-262.997	-0.077
$\text{WS}_2\text{-S}_2\text{-O}_2$	-277.664	-266.132	-0.066
$\text{MoSe}_2\text{-Se}_2\text{-O}_2$	-250.599	-240.104	0.453
$\text{WSe}_2\text{-Se}_2\text{-O}_2$	-253.119	-242.566	0.424

Table 6.3.1a: Total and adsorption energies of oxidized TMD nanoribbons.

We would like to check if the metallic edges of TMDs discussed in Ch. 4 are affected by the presence of other elements such as Oxygen. To answer this question, we perform density – of – states and bandstructure calculations for TMD nanoribbons before and after oxidization and we compare our results to the corresponding 2D TMD monolayers, both pristine and oxidized.

In order to perform a comparison between 1D nanoribbons and 2D monolayers we first construct the pristine 2D structures using the same supercell as in nanoribbons without the edge chalcogen adatoms. This supercell now consists of 36 atoms in total (12 metal atoms and 24 chalcogen atoms) and a vacuum of 6 \AA is applied only in the \hat{z} direction. We then introduce Oxygen atoms to our pristine 2D structures, one on top of each chalcogen atom, since according to previous research (see Refs.: [40,100]) this is the preferable adsorption site. In this case our supercell consists of 48 atoms (12 metal atoms, 24 chalcogen atoms and 12 oxygens). Figure 6.3.1a presents a typical model of pristine and oxidized TMD monolayers (Notice the missing vacuum in the supercell at the \hat{y} direction). The oxygen adsorption energies of 2D TMDs are given in table 6.3.1b.

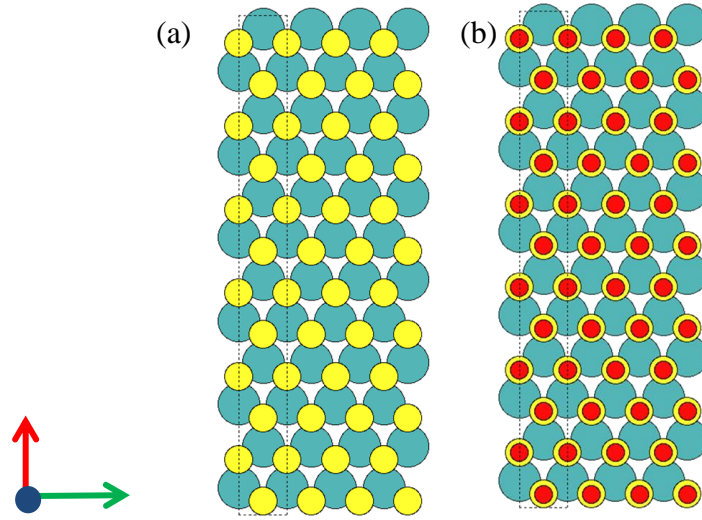


Figure 6.3.1a: Top view of a typical model of TMD monolayers prior (a) and after (b) surface oxidation. Metal atoms are presented by blue color, while chalcogens and oxygens are presented by yellow and red respectively.

	E_{2D,O_n} (eV)	E_{2D} (eV)	E_{ads} (eV)
Mo₁₂S₂₄O₁₂	-324.943	-257.082	0.045
W₁₂S₂₄O₁₂	-325.728	-260.241	0.243
Mo₁₂Se₂₄O₁₂	-289.372	-234.589	1.135
W₁₂Se₂₄O₁₂	-291.223	-237.413	1.216

Table 6.3.1b: Total and adsorption energies of oxidized TMD monolayers.

6.3.1.1 Density of states and band structure

For each material we plot the density of states as a function of the energy minus the Fermi level. In all cases, we shift the DOS plots by aligning the low – lying s states located at about -14 eV in order to probe changes in Fermi levels and we overlay the graphs of quasi 1D nanoribbons to the 2D materials for purposes of comparison. A full analysis of this procedure is presented in section 6.5.1 in which we examine the effect of different adatom concentrations on the Fermi level. Figure 6.3.1.1a presents the DOS for MoS₂, WS₂, MoSe₂, and WSe₂ nanoribbons in the most thermodynamically stable oxidized edge formation.

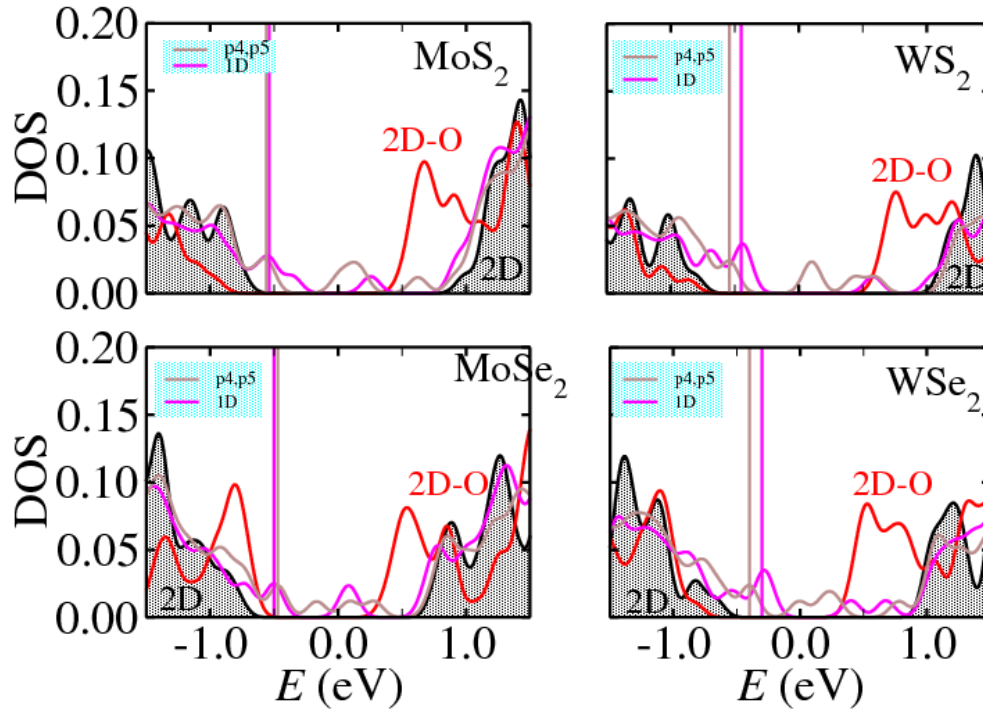


Figure 6.3.1.1a: Comparison of DOS for all four TMDs between the pristine and oxidized 2D monolayers and the nanoribbons before and after edge oxidation. In all graphs the pristine monolayer structure is shown with the grey shaded area, the oxidized 2D material is described by the red curve, while the nanoribbons without and with adsorbed Oxygen are presented by magenta and brown curves respectively. The Fermi level of 1D nanoribbons is shown by the vertical lines while for the 2D monolayers E_F is set at zero eV.

From figure 6.3.1.1a we see for the 2D monolayer with oxygen adatoms at a 100% coverage that new states are introduced in the gap without however closing the gap totally. This result is in agreement with previous studies done by Santosh KC et al., in 2015 [100] and the changes in the gap are presented in table 6.3.1.1a. Also in regard to the nanoribbons, the oxidation of their edges does not affect the metallic character of the materials. This is shown clearly where the Fermi level of the 1D nanoribbons lies in the gap of the 2D material.

	Pristine gap in (eV)	Oxidized gap in (eV)
MoS₂	1.75	1.47
WS₂	1.95	1.50
MoSe₂	1.55	1.07
WSe₂	1.68	1.24

Table 6.3.1.1a: Table of the energy gaps of the 2D TMD monolayers before and after oxidation.

A further confirmation of the metallic character of the quasi 1D nanoribbons was done by performing a bandstructure calculation. This is presented in the following plots. The energy shift done in both DOS and bandstructure plots ie. the Fermi level of the nanoribbons is presented in table 6.3.1.1b.

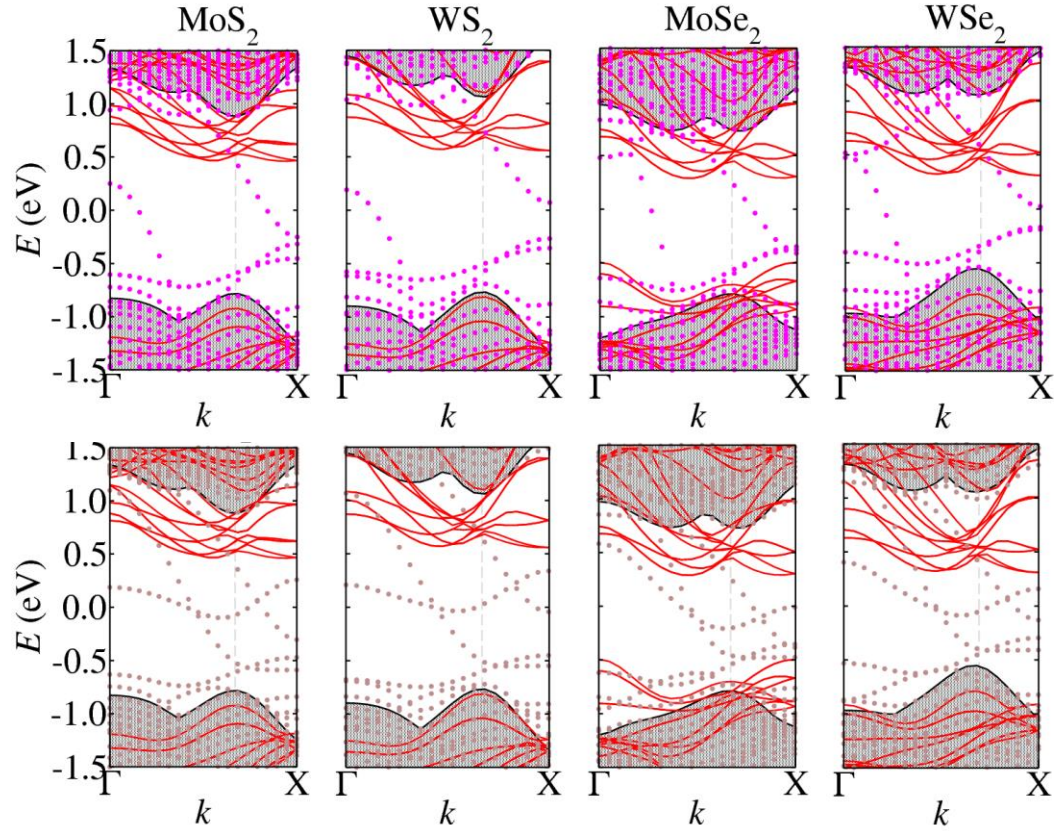


Figure 6.3.1.1b: Comparison of bandstructure for all four TMDs between the pristine and oxidized 2D monolayers and the nanoribbons before (**up**) and after (**down**) edge oxidation. In all graphs the curves are color coded in response to the DOS plots. The direct gap of the pristine TMD monolayers is shown by the grey vertical dashed line at $2/3$ of the \hat{x} axis. The Fermi level of 2D structures is set at zero eV.

	1D Fermi level (eV)	1D,O ₂ Fermi level (eV)
MoS₂	-0.54	-0.56
WS₂	-0.45	-0.54
MoSe₂	-0.50	-0.47
WSe₂	-0.30	-0.40

Table 6.3.1.1b: Table of the Fermi levels of the quasi 1D TMD nanoribbons before and after edge oxidation.

From the bandstructure plots it is obvious that the metallic character of the 1D nanoribbons no matter the edge composition will remain intact. Also another interesting finding is that when the 2D TMD monolayers are 100% covered with oxygen adatoms even though their semiconducting character is still present, the gap changes from direct to indirect. An opposite procedure is observed when the dimension of the material is lowered from 3D to 2D.

6.4 Hydroxyl adsorption on TMD nanoribbons.

In order to simulate OH adsorption at TMD edge, we use our previously relaxed structures and we attach hydrogen atoms on top of the Oxygens and repeat the structure optimization procedure. We then perform two calculations for each structure for the adsorption energy and the differential adsorption energy. In order to do that we first calculate the potential energy of a molecular Hydrogen and a Hydroxyl radical. The resulting values for the energy were found -6.655 eV and -8.226 eV respectively. The equation describing the corresponding adsorption energies are given below.

Adsorption energy of OH radical on TMD nanoribbon:

$$E_{ads} = \frac{1}{n}(E_{1D,O_nH_n} - E_{1D} - nE_{OH}) \quad (3)$$

Differential adsorption energy of H on oxidized TMD nanoribbon:

$$E_{diff} = \frac{1}{n}(E_{1D,O_nH_n} - E_{1D,O_n} - \frac{n}{2}E_{H_2}) \quad (4)$$

Where n is the number of adsorbed atoms or radicals ($n=2$ here) while E describes the corresponding total energies.

Table 6.4a presents the results for all total and adsorption energies:

	E_{1D,O_nH_n} (eV)	E_{1D,O_n} (eV)	E_{1D} (eV)	E_{ads} (eV)	E_{diff} (eV)
MoS₂-S₂-O₂-H₂	-282.673	-274.474	-262.997	-1.612	-0.772
WS₂-S₂-O₂-H₂	-285.917	-277.664	-266.132	-1.666	-0.799
MoSe₂-Se₂-O₂-H₂	-259.838	-250.599	-240.104	-1.641	-1.292
WSe₂-Se₂-O₂-H₂	-262.466	-253.119	-242.566	-1.724	-1.346

Table 6.4a: Total and adsorption energies of TMD nanoribbons with hydroxyl groups at the upper edge.

TMD nanoribbons with adsorbed Hydroxyl at the edge show an increase in the bonds between the S-O and Se-O going from of approximately 0.3Å. This increase is expected due to the presence of Hydrogen on each Oxygen atom. Figures 6.4a and 6.4b show a selected atoms (A,B,C,D) at the edge of TMD nanoribbons after Hydroxyl adsorption which correspond to different angles between Mo-S-O, W-S-O, Mo-Se-O and W-Se-O as given in table 6.4b.

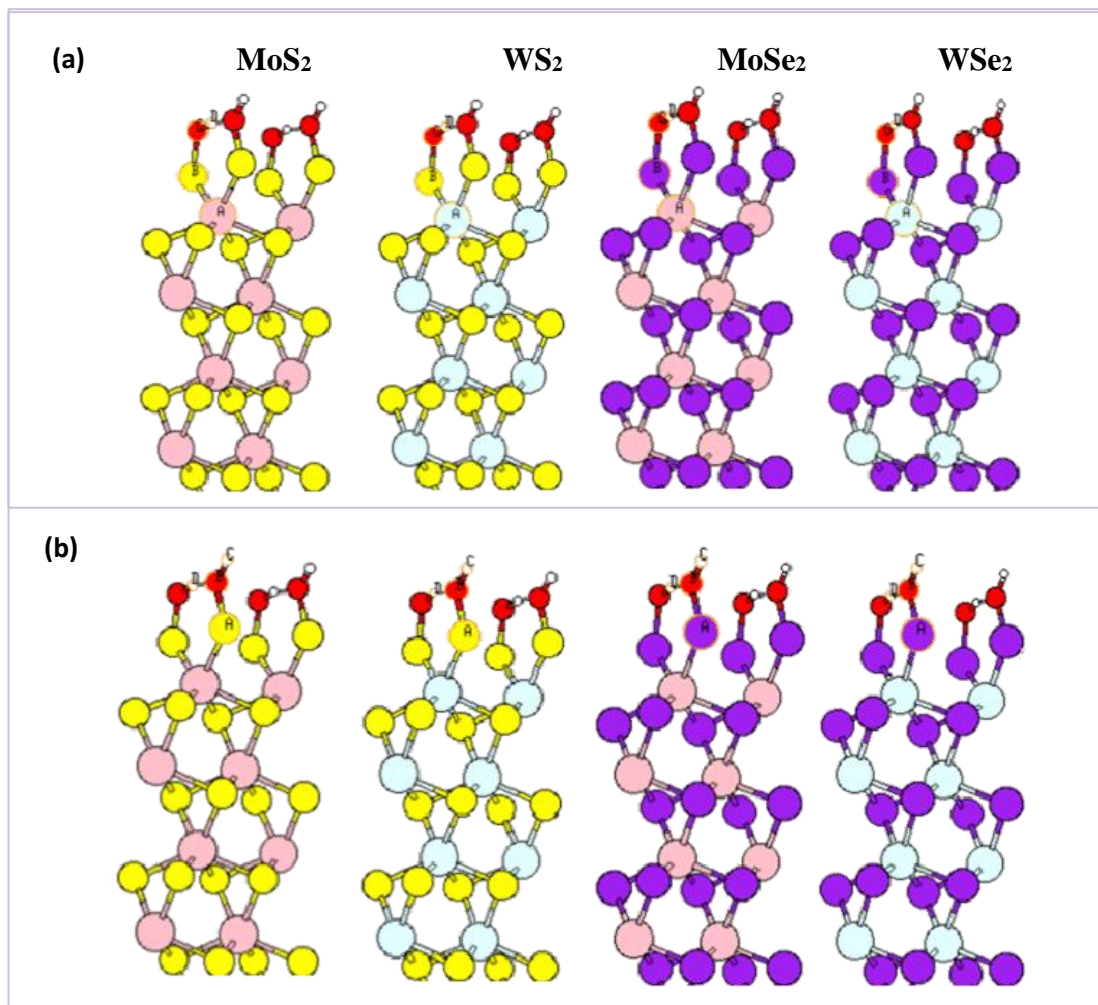


Figure 6.4: Ball-and stick model focused on the edge of relaxed structures of TMD nanoribbons after hydroxyl adsorption. For each structure two different sets of angles are shown in **(a)** and **(b)**. In all figures the atoms are color coded in regard to the element. Mo and W atoms are shown with pink and cyan respectively, while yellow atoms represent Sulfur and purple Selenium. Red atoms correspond to Oxygens and white to Hydrogens.

material	BCD (°)a	ABC (°)b	Torsion ABCD(°)
MoS ₂	107.71	113.06	0.00
WS ₂	107.25	113.84	0.00
MoSe ₂	107.70	109.86	0.00
WSe ₂	107.16	109.66	0.00

Table 6.4b: Geometrical characteristics of the upper edge of TMD nanoribbons with Hydroxyl group.

Although the plane of the edge atoms does not undergo any rotation and all atoms are again found vertical to the nanoribbon structure, in this case as opposed to oxidized TMDs the angles formed between the metals and the Oxygens get smaller (from $\sim 120^\circ$ to 107°). The interaction of the front Oxygen atom (labeled B in Fig. 6.4b) with the inner Hydrogen with weak Hydrogen bonding (distance between atoms $\sim 1.6 \text{ \AA}$) is causing a more close packed edge on the nanoribbons.

6.4.1 Density of states and band structure

We now plot the density of states and the bandstructure for the quasi 1D nanoribbons following the same procedure as in the case of the oxidized structures. The DOS and bandstructure are presented in figures 6.4.1a and 6.4.1b respectively. Figure 6.4.1a shows clearly that the metallic states are robust against any changes in the edge structure of the materials. This is further confirmed by the bandstructure calculations.

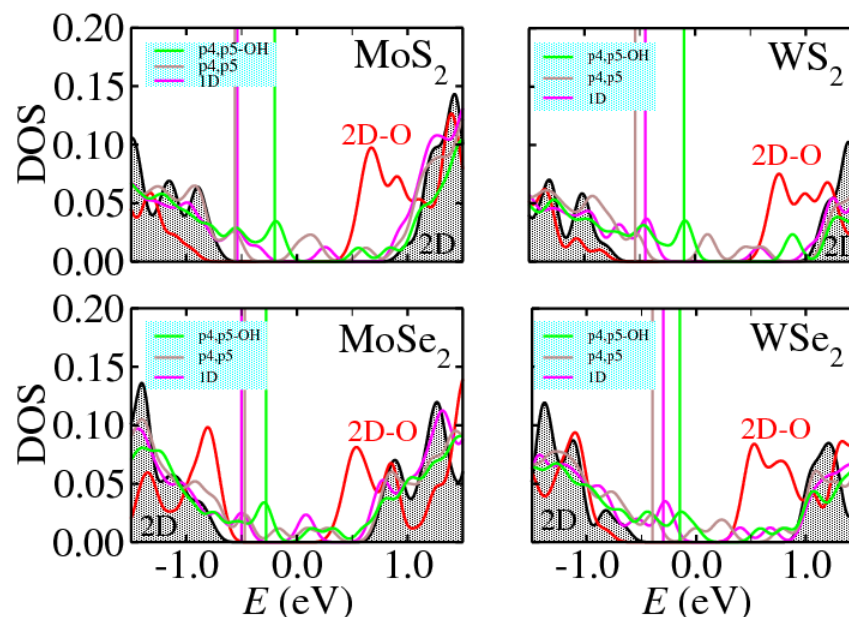


Figure 6.4.1a: Comparison of DOS for all four TMDs between the pristine and oxidized 2D monolayers and the nanoribbons with different edge composition. In all graphs the pristine monolayer structure is shown with the grey shaded area and the oxidized 2D material is described by the red curve. The nanoribbons without and with adsorpted Oxygen are presented by magenta and brown curves respectively, while green curve shows the nanoribbons with hydroxyl groups. The Fermi level of 1D nanoribbons is shown by the vertical lines while for the 2D monolayers E_F is set at zero eV.

We shift the DOS and bandstructure curves of the 1D TMD nanoribbons with hydroxyl groups to match the lowest states of the oxidized 1D TMD nanoribbons. The energy shift ie. the Fermi level shift of the nanoribbons is presented in table 6.4.1.

	1D,O ₂ H ₂ Fermi level (eV)
MoS₂	-0.20
WS₂	-0.10
MoSe₂	-0.28
WSe₂	-0.15

Table 6.4.1: Table of the Fermi levels of the quasi 1D TMD nanoribbons after hydroxyl adsorption.

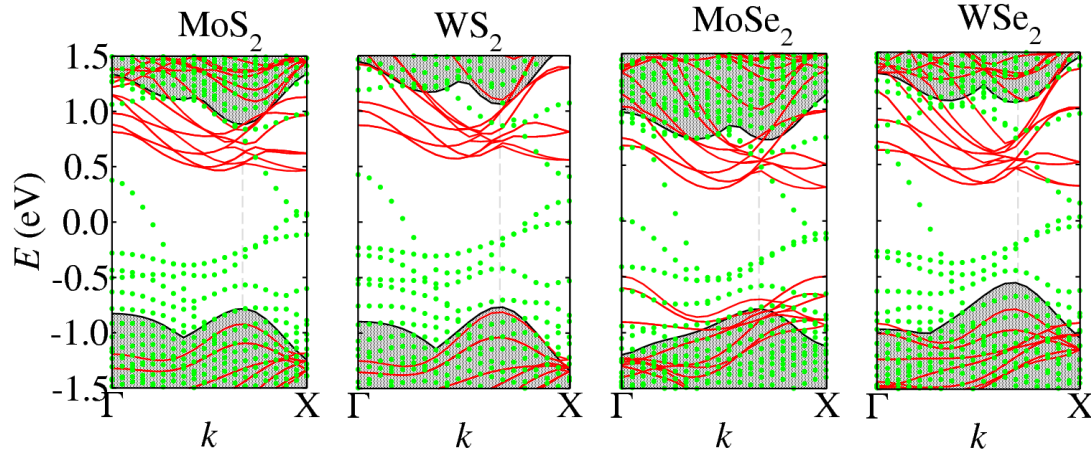


Figure 6.4.1b: Comparison of bandstructure for all four TMDs between the pristine and oxidized 2D monolayers and the nanoribbons after hydroxyl adsorption. In all graphs the curves are color coded in response to the DOS plots. The direct gap of the pristine TMD monolayers is shown by the grey vertical dashed line at $2/3$ of the \hat{x} axis. The Fermi level of 2D structures is set at zero.

6.5 TMD nanoribbons with 50% oxygen and hydroxyl adsorption

The final structures that we will study are TMD nanoribbons with 50% coverage with adsorbed Oxygen and Hydroxyl. In order to construct our nanoribbons we use a (2x6) supercell which consists of 2 unit cells in the \hat{x} direction and 6 unit cells in the y . Since a DFT calculation requires many cpu hours for calculations, let alone for close to 80 atoms, we try to minimize as much as possible the needed time. Thus, we refer to the previously optimized structures of TMDs with two chalcogen adatoms from chapter 4 and the ones with adsorbed Oxygen and Hydroxyl from previous sections.

Using the edge atom position from these structures, we manipulate our edge for the (2x6) supercells and we manage to minimize our required calculation time to one third. However, the process is still very time consuming preventing us from creating multiple cases of adsorption concentration. The geometrical characteristics for TMD nanoribbons with (2x6) supercell and 50% Oxygen and Hydroxyl adsorption are presented in the following sections. Table 6.5 shows the total energies and the adsorption energies of 50% Oxygen and Hydroxyl coverage of TMD nanoribbons according to equations (2) and (3) from sections 6.2 and 6.4 respectively.

	E_{1D,O_nH_n} (eV)	E_{1D,O_n} (eV)	E_{1D} (eV)	E_{ads} (eV)
$\text{MoS}_2\text{S}_2(\text{O})_{0.5}$	-	-537.025	-525.983	0.179
$\text{WS}_2\text{S}_2(\text{O})_{0.5}$	-	-543.469	-532.234	0.082
$\text{MoSe}_2\text{Se}_2(\text{O})_{0.5}$	-	-490.372	-480.184	0.606
$\text{WSe}_2\text{Se}_2(\text{O})_{0.5}$	-	-495.492	-485.197	0.552
$\text{MoS}_2\text{S}_2(\text{OH})_{0.5}$	-545.633	-	-525.983	-1.599
$\text{WS}_2\text{S}_2(\text{OH})_{0.5}$	-551.963	-	-532.234	-1.639
$\text{MoSe}_2\text{Se}_2(\text{OH})_{0.5}$	-499.854	-	-480.184	-1.609
$\text{WSe}_2\text{Se}_2(\text{OH})_{0.5}$	-504.939	-	-485.197	-1.645

Table 6.5: Total and adsorption energies of (2x6) TMD nanoribbons with 50% oxygen atoms and hydroxyl groups at the upper edge.

6.5.1 The effect of adatoms concentration on the electronic properties

In this section we examine the effect of Hydroxyl and Oxygen adsorption concentration on the electronic properties of TMD nanoribbons. In the following density of states graphs (Fig.: 6.5.1) we present analytically the procedure that we followed in order to calculate Fermi – level pinning. First, the lowest – energy peaks located at about -14 eV below the Fermi level are aligned in the different structures. These peaks correspond to s electrons of S atoms in the bulk and are very little affected by the surface structure. This procedure is shown in Fig.: 6.5.1. This alignment shifts the whole density of states plot relative to the DOS plot of the 2D material (Fig.: 6.5.2).

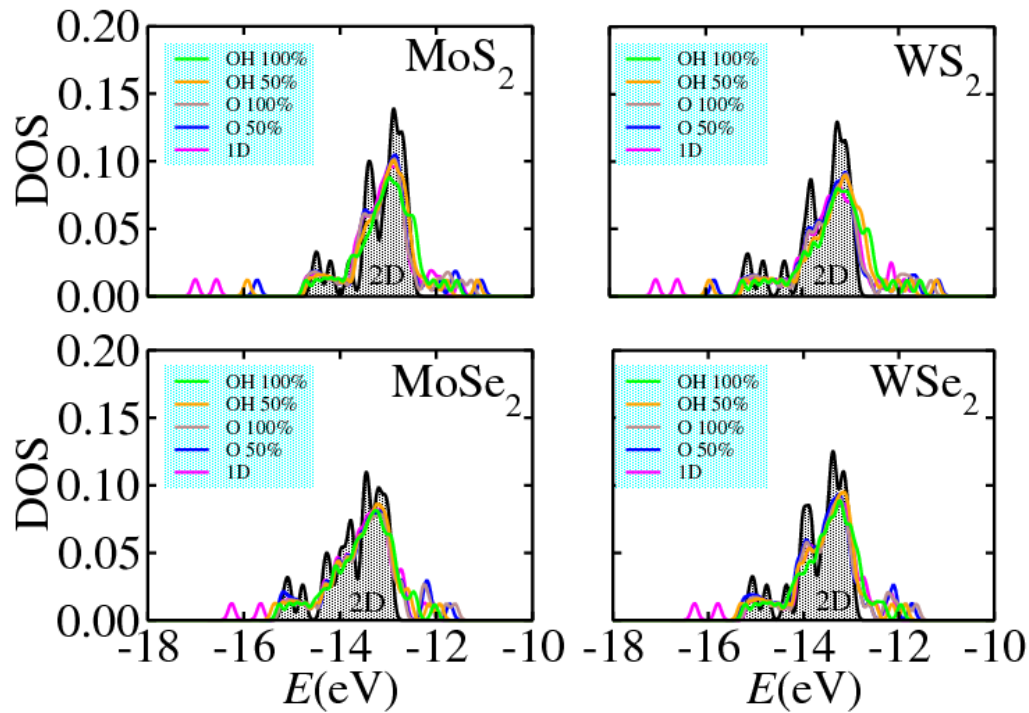


Figure 6.5.1: Density of states for bulk 2D MX_2 (grey shaded area) and the MX_2 nanoribbons (colored solid lines) with (1x6) and (2x6) supercells and different Oxygen and Hydroxyl concentrations on the upper edge. The energy range is within 4 eV of the low – energy peaks.

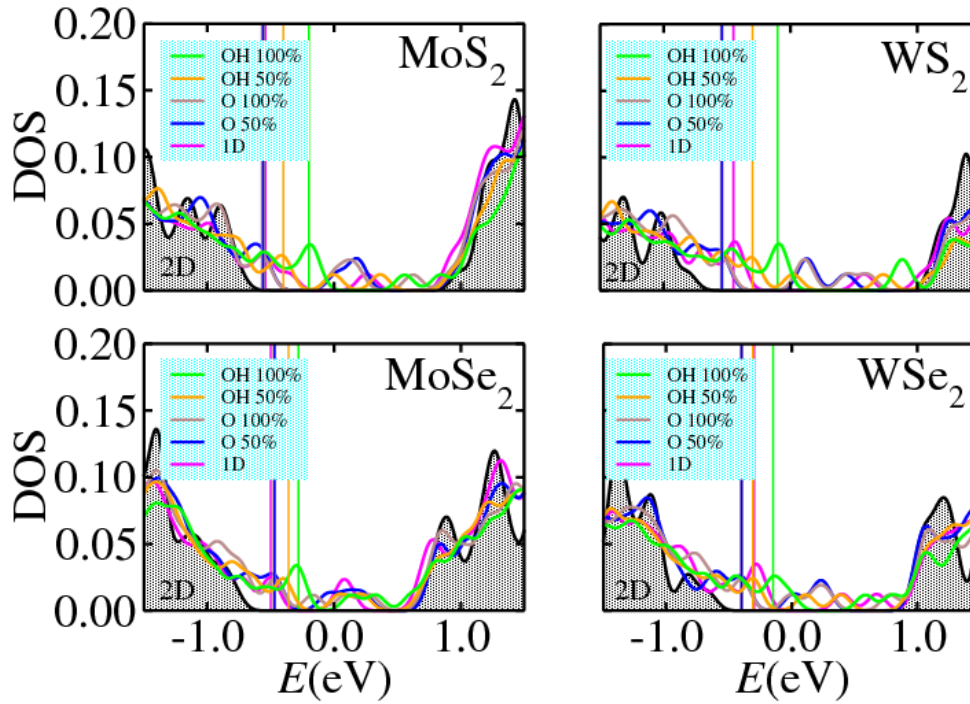


Figure 6.5.2: Density of states for bulk 2D MX₂ (grey shaded area) and the MX₂ nanoribbons (colored solid lines) with (1x6) and (2x6) supercells and different Oxygen and Hydroxyl concentrations on the upper edge. The energy range is within 1.5 eV of the mid-gap point, which is set to zero, the Fermi levels of the nanoribbons are shown with color-coded vertical lines.

We first align the electronic states of the 1D nanoribbons to the lowest states of the single layer. We then use these states as reference point to which we align the electron states of the oxidized nanoribbons. And finally, with the addition of hydrogen for the formation of hydroxyls, we shift the curves to the lowest states of the oxidized nanoribbons. In table 6.5.1 we collect all the numerical values of the Fermi level changes.

	1D E _F (eV)	1D, O 100% E _F (eV)	1D,O 50% E _F (eV)	1D,OH 100% E _F (eV)	1D,OH 50% E _F (eV)
MoS₂	-0.54	-0.56	-0.56	-0.20	-0.40
WS₂	-0.45	-0.54	-0.54	-0.10	-0.30
MoSe₂	-0.50	-0.47	-0.47	-0.28	-0.36
WSe₂	-0.30	-0.40	-0.40	-0.15	-0.31

Table 6.5.1: Pinning of Fermi Level of (1x6) and (2x6) MX₂ nanoribbons and various O, OH concentrations.

From table 6.5.1 we find that in all cases the Fermi level of TMD nanoribbons always falls in the gap of the 2D monolayer; A significant result that proves that the electronic properties of quasi 1D TMD nanoribbons are robust regardless of the environmental conditions. Also, the formation of a transition metal dichalcogenide nanoribbon leads to a lowering of the Fermi level, as opposed to the Fermi level of the monolayer which is set at zero eV. This behavior occurs due to the formation of a dipole moment at

the edges by the broken symmetry of the material. This is further confirmed by the change in the Fermi level in the presence of hydrogen atoms, which is an electrophilic addition and causes a change in the dipole moment and a shift of the Fermi level to higher energies.

Finally, an interesting finding from this study is that the presence of oxygen regardless of 50% or 100% coverage shows no difference in the Fermi level. A possible explanation for this result could be that the change of the dipole moment for these two concentration is similar since both cases undergo stress at the edges, which in turn would cause a change in the electron density at the nanoribbon edge. However, for the clarification of the behavior more research is required considering various oxygen concentrations.

6.6 TMD nanoribbons as candidates for Oxygen and Hydrogen Evolution Reactions

For the final part of this study we summarize our results for the adsorption energies of oxygen atoms and hydroxyl radicals on transition metal dichalcogenide nanoribbons and perform a comparison of their catalytic properties. Table 6.6 present our calculations for the adsorption energies of TMD nanoribbons with 50% and 100% oxygen and hydroxyl concentrations on the upper edge of the nanoribbon. A graphical representation of these results is shown in figure 6.6.

	$E_{ads}(\text{eV})$		$E_{ads}(\text{eV})$
$\text{MoS}_2\text{S}_2(\text{O})_{0.5}$	0.179	$\text{MoS}_2\text{S}_2(\text{OH})_{0.5}$	-1.599
$\text{WS}_2\text{S}_2(\text{O})_{0.5}$	0.082	$\text{WS}_2\text{S}_2(\text{OH})_{0.5}$	-1.639
$\text{MoSe}_2\text{Se}_2(\text{O})_{0.5}$	0.606	$\text{MoSe}_2\text{Se}_2(\text{OH})_{0.5}$	-1.609
$\text{WSe}_2\text{Se}_2(\text{O})_{0.5}$	0.552	$\text{WSe}_2\text{Se}_2(\text{OH})_{0.5}$	-1.645
$\text{MoS}_2\text{S}_2(\text{O})_{1.0}$	-0.077	$\text{MoS}_2\text{S}_2(\text{OH})_{1.0}$	-1.612
$\text{WS}_2\text{S}_2(\text{O})_{1.0}$	-0.066	$\text{WS}_2\text{S}_2(\text{OH})_{1.0}$	-1.666
$\text{MoSe}_2\text{Se}_2(\text{O})_{1.0}$	0.453	$\text{MoSe}_2\text{Se}_2(\text{OH})_{1.0}$	-1.641
$\text{WSe}_2\text{Se}_2(\text{O})_{1.0}$	0.424	$\text{WSe}_2\text{Se}_2(\text{OH})_{1.0}$	-1.724

Table 6.6: Adsorption energies of Oxygen atoms and Hydroxyl groups in different concentrations on transition metal dichalcogenide nanoribbons.

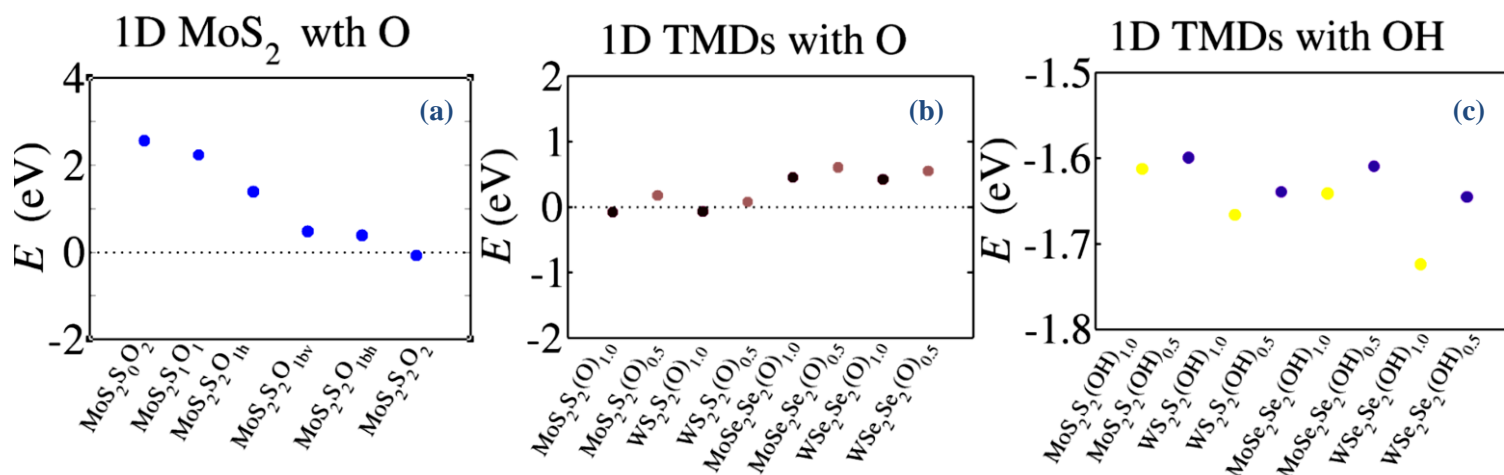


Figure 6.6: (from left to right) Adsorption and substitution energies for MoS₂ nanoribbons with Oxygen atoms at various sites. Adsorption energies for TMD nanoribbons with Oxygen adatoms. Adsorption energies for TMD nanoribbons with Hydroxyl groups.

The preference of Oxygen adsorption/substitution on 2D TMD monolayers has been confirmed through multiple studies on 2D [42, 99, 100, 104-107]. Here we show that quasi 1D TMDs when in oxygen rich environment, will attract atoms on the exposed edge. Figure 6.6a shows that the addition of Oxygen atoms at the nanoribbon edge is thermodynamically favored. This edge formation is the one used throughout this chapter, where the Oxygen adsorption occurs on top of Sulfur edge atoms, as explained in section 6.2

From figure 6.6b, we observe a difference in the adsorption energies for the four MoS₂, WS₂, MoSe₂ and WSe₂ nanoribbons with 100% coverage, showing that molybdenum disulfide is more reactive to oxygen, than the rest three TMDs. The adsorption energy of oxygen on Sulfurides is approximately 0.4 eV lower than Selenides. Specifically the lowest adsorption energy is found for MoS₂ nanoribbons with 100% Oxygen coverage. This result, shows that molybdenum disulfide is more reactive to Oxygen than any other TMD.

For the case of hydroxyl – rich environment we find that the hydroxyl groups will bound strongly to the edge of the TMD nanoribbons, showing adsorption energies in the range of -1.599 eV to -1.724 eV. This result suggests an intense hydrophilicity of TMDs meaning that when the material is exposed to water molecules it will instantly react with them. However, the presence of a second Hydrogen atom from the water molecule would cause positively charged edge sites creating a structure similar to transition states. The passivation of these states would require the removal of the extra Hydrogen, suggesting that TMD nanoribbons could be candidates for Hydrogen Evolution Reaction. This, result explains the use of MoS₂ as catalysts for complex chemical reactions.

6.7 Conclusion

In this chapter, we simulated TMD nanoribbons in Oxygen and Hydroxyl rich environments. We perform DFT calculations for the adsorption energies of TMD nanoribbons with adsorbed Oxygen and Hydroxyl in different concentrations and we examined the electronic properties

such density of states and bandstructure and we compared our results to pristine and oxidized 2D monolayers.

We found the preferable edge formation and by studying the electronic properties we concluded that the metallic character around the edges of TMD nanoribbons is robust against the presence of O and OH. However, in the case of the 2D materials, we found that the direct gap semiconducting behavior of the pristine 2D monolayer changes to indirect when the material undergoes oxidation.

Similarly to the chalcogen saturated nanoribbons in chapter 4, we studied the effect of Oxygen adatoms and Hydroxyl groups, by aligning their electronic states in the density of states graphs, to the DOS of the 1D TMDs and we found that no matter the environment (O or OH) the Fermi level of the 1D nanoribbons is always lower than the Fermi level of the 2D materials, although depending the electronegativity of the adatoms a shift to higher energies (yet still lower than the 2D) can occur.

Finally, we performed a comparison for the adsorption energies of TMD nanoribbons with O, and OH and we found that Molybdenum Disulfide is much more reactive to Oxygen than the rest TMDs and that the edges of all four TMDs present intense hydrophilicity.

Conclusions

Simulations of model S structures provided insight into the electronic structure of S compounds. We found that TBA, after finding the appropriate parameters through fitting to DFT, can describe accurately the bandstructure of these compounds, although TBA parameters might differ from one structure to the other.

DFT calculations on the electronic properties, density of states and bandstructure of TMD nanoribbons reveal that regardless of edge reconstruction, composition or width, quasi 1D TMDs present metallic edges, as opposed to the 2D bulk semiconducting materials. With the calculation of the edge energy we concluded on the most stable edge formation, which depending on the chalcogen environment, would be either with two or four adatoms.

Next, by locating the true surface states and by comparing our results on the probability density to the Shockley model, we found that the sole reason for the presence of the metallic behavior is the broken periodicity of the material as we move to lower dimension from 2D monolayer to quasi 1D nanoribbon.

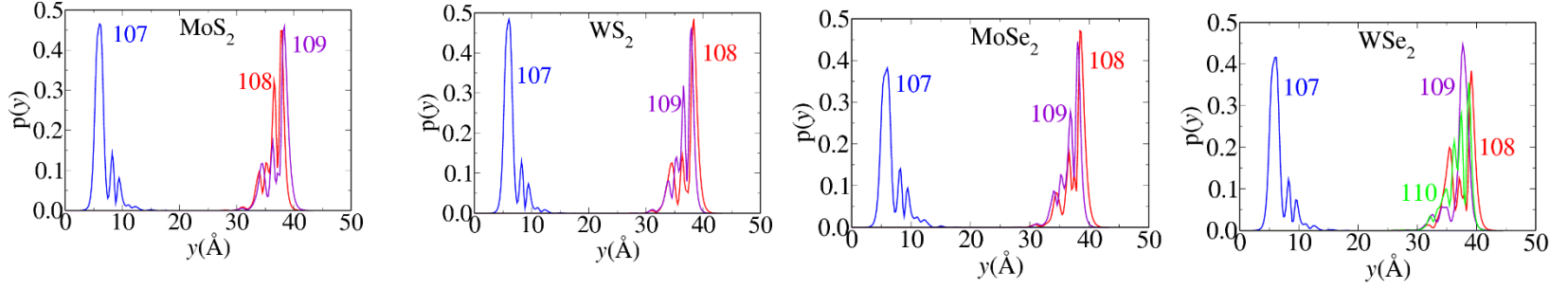
Finally, with the introduction of O and OH on the edge of the most stable structure of the TMD nanoribbons, we studied the effect of environmental conditions in our structures and we compared our results to the 2D pristine and oxidized monolayers. We found that the electronic properties of TMD nanoribbons are robust against the presence of O or OH, as opposed to the 2D materials in which the direct gap shifts to indirect in the presence of oxygen. Compared to MoSe_2 , WS_2 and WSe_2 , MoS_2 showed increased adsorption of O, while the most reactive in OH was found to be WSe_2 . However, all four materials are expected to be highly reactive in OH – rich environment such as water.

Transition metal dichalcogenide nanoribbons present unique electronic properties and can be great candidates for a wide range of applications from functional devices to catalysts for chemical reactions, such as oxygen evolution.

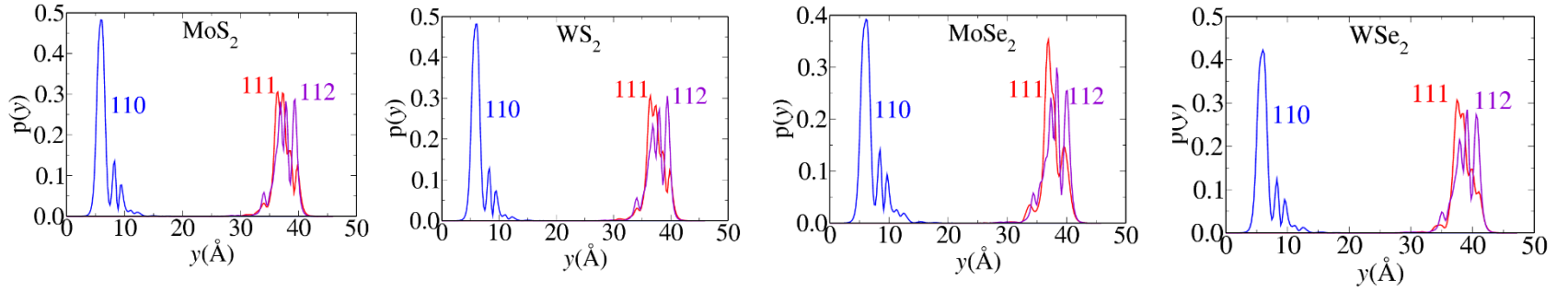
Appendix

Graphical representations of the electron probability densities for all four TMD nanoribbons with different edge reconstructions.

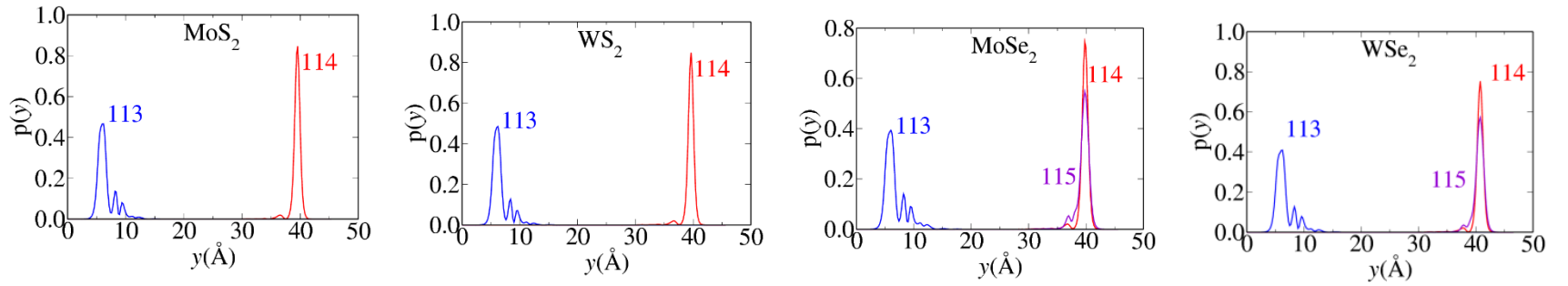
Unsaturated TMD nanoribbons



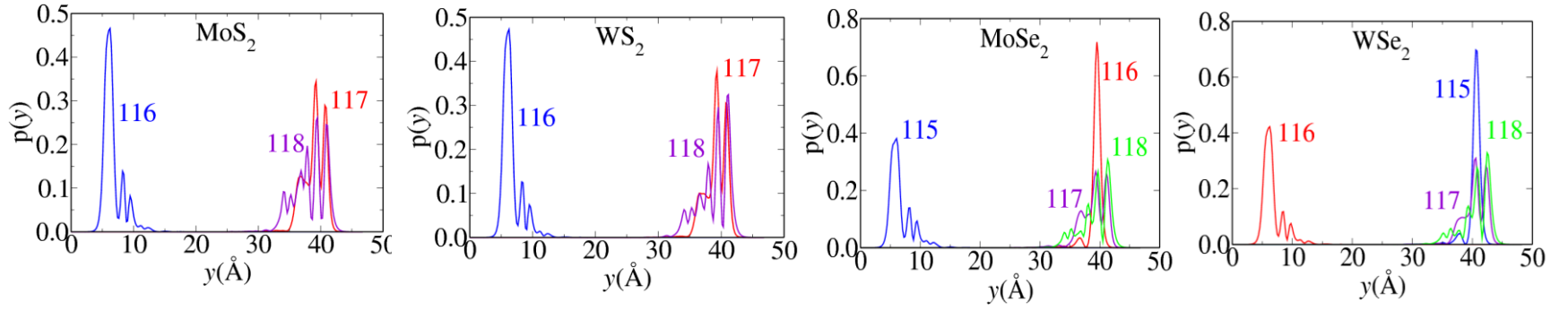
Saturated TMD nanoribbons with one chalcogen adatom



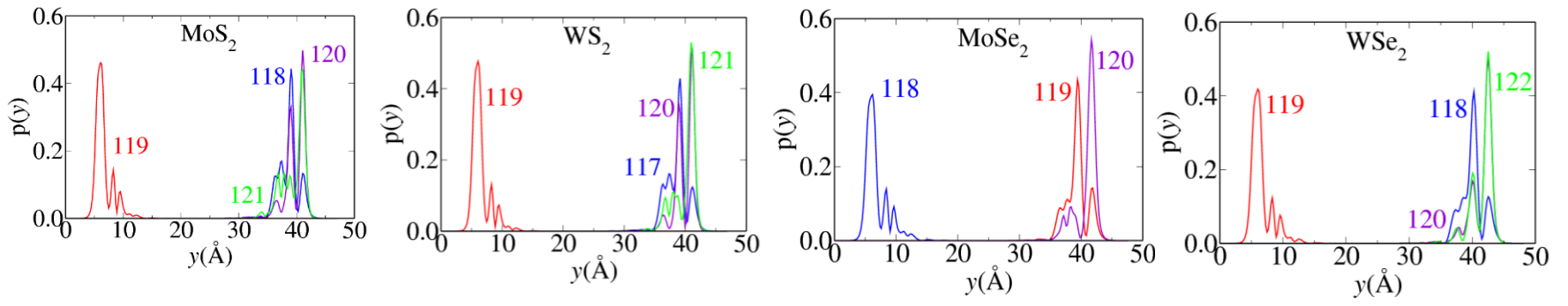
Saturated TMD nanoribbons with two chalcogen adatoms



Saturated TMD nanoribbons with three chalcogen adatoms



Saturated TMD nanoribbons with four chalcogen adatoms



REFERENCES

- [1] K. D. Bronsema, J. L. De Boer and F. Jellinek, *On the Structure of Molybdenum Diselenide and Disulfide*, Z. Anorg. Allg. Chem. 540/541, 15-17 (1986)
- [2] W. J. Schutte, J. L. De Boer and F. Jellinek, *Crystal Structures of Tungsten Disulfide and Diselenide*, J. Solid State Chem. 70, 207-209 (1987)
- [3] R. Roldan, J. A. Silva-Guillén, M. Pilar López-Sancho, F. Guinea, E. Cappelluti and P. Ordejón, *Electronic properties of single-layer and multilayer transition metal dichalcogenides MX_2 ($M=Mo, W$ and $X=S, Se$)*, Ann. Phys. 526, 347-357 (2014)
- [4] K. F. Mak, C. Lee, J. Hone, J. Shan and T. F. Heinz, *Atomically thin MoS_2 : a new direct – gap semiconductor*, Phys. Rev. Lett. 105, 136805 (2010)
- [5] A. Splendiani, L. Sun, Y. Zhang, T. Li, C.Y. Chim, G. Galli and F. Wang, *Emerging Photoluminescence in Monolayer MoS_2* , Nano Lett. 10, 1271-1275 (2010)
- [6] A. Kuc, N. Zibouche and T. Heine, *Influence of quantum confinement on the electronic structure of the transition metal sulfide TS_2* , Phys. Rev. B 83, 245213 (2011)
- [7] Y. Ding, Y. Wang, J. Ni, L. Shi, S. Shi and W. Tang, *First principles study of structural, vibrational and electronic properties of graphene-like MX_2 ($M=Mo, Nb, W, Ta$; $X=S, Se, Te$) monolayers*, Physica B 406, 2254-2260 (2011)
- [8] L. Liu, S. B. Kumar, Y. Ouyang and J. Guo, *Performance limits of monolayer transition metal dichalcogenide transistors*, IEEE Trans. Electron Devices 58, 3042-3047 (2011)
- [9] E. S. Kadantsev and P. Hawrylak, *Electronic structure of a single MoS_2 monolayer*, Solid State Comm. 152, 909-913 (2012)
- [10] A. E. Maniadaki, G. Kopidakis and I. N. Remediakis, *Strain engineering of electronic properties of transition metal dichalcogenide monolayers*, Solid State Commun. 227, 33-39 (2016)
- [11] S. Helveg, J. V. Lauristen, E. Lægsgaard, I. Stensgaard, J. K. Nørskov, B. S. Clausen, H. Topsøe and F. Besenbacher, *Atomic –Scale Structure of Single- Layer MoS_2 Nanoclusters*, Phys. Rev. Lett. 84, 951-954, (2000)
- [12] M. V. Bollinger, J. V. Lauristen, K. W. Jacobsen, J. K. Nørskov, S. Helveg and F. Besenbacher, *One-Dimensional Metallic Edge States in MoS_2* , Phys. Rev. Lett. 87, 196803, (2001)
- [13] M. V. Bollinger, K. W. Jacobsen and J. K. Nørskov, *Atomic and electronic structure of MoS_2 nanoparticles*, Phys. Rev. B 67, 085410, (2003)
- [14] E. Ridolfi, L. R. F. Lima, E. R. Mucciolo and C. H. Lewenkopf, *Electronic transport in disordered MoS_2 nanoribbons*, Phys. Rev. B 95, 035430 (2017)

- [15] G. Camacho-Bragado, J. Elechiguerra, A. Olivas, S. Fuentes, D. Galvan, and M. J. Yacaman, *Structure and catalytic properties of nanostructured molybdenum sulfides*, J. Catal. 234, 182 (2005).
- [16] Z. Wang, H. Li, Z. Liu, Z. Shi, J. Lu, K. Suenaga, S.-K. Joung, T. Okazaki, Z. Gu, J. Zhou, Z. Gao, G. Li, S. Sanvito, E. Wang, and S. Iijima, *Mixed Low-Dimensional Nanomaterial: 2D Ultranarrow MoS₂ Inorganic Nanoribbons Encapsulated in Quasi-1D Carbon Nanotubes*, J. Am. Chem. Soc. 132, 13840 (2010)
- [17] Y. Li, Z. Zhou, S. Zhang and Z. Chen, *MoS₂ nanoribbons: High Stability and Unusual Electronic and Magnetic Properties*, J. Am. Chem. Soc. 130, 16739-16744 (2008)
- [18] L. Kou, C. Tang, Y. Zhang, T. Heine, C. Chen, and T. Frauenheim, *Tuning Magnetism and Electronic Phase Transitions by Strain and Electric Field in Zigzag MoS₂ Nanoribbons* J. Phys. Chem. Lett. 3, 2934 (2012).
- [19] J. Kim, W. S. Yun, and J. D. Lee, *Optical Absorption of Armchair MoS₂ Nanoribbons: Enhanced Correlation Effects in the Reduced Dimension*, J. Phys. Chem. C 119, 13901 (2015).
- [20] M. Gibertini, G. Pizzi, and N. Marzari, *Engineering polar discontinuities in honeycomb lattices*, Nature Commun. 5, 5157 (2014).
- [21] M. Gibertini and N. Marzari, *Emergence of One-Dimensional Wires of Free Carriers in Transition-Metal-Dichalcogenide Nanostructures*, Nano Lett. 15, 6229 (2015).
- [22] D. Davelou, G. Kopidakis, G. Kioseoglou and I. N. Remediakis, *MoS₂ nanostructures: Semiconductors with metallic edges*, Solid State Communications 192, 42–46, (2014)
- [23] B. Hinnemann, P.G. Moses, J. Bonde, K.P. Jørgensen, J.H. Nielsen, S. Hørch, I. Chorkendorff and J.K. Nørskov, *Biomimetic Hydrogen Evolution: MoS₂ Nanoparticles as catalyst for Hydrogen Evolution*, J. Am. Chem. Soc. 127, 5308-5309 (2005)
- [24] B. Hinnemann, J. K. Nørskov, and H. Topsøe, *A Density Functional Study of the Chemical Differences between Type I and Type II MoS₂-Based Structures in Hydrotreating Catalysts*, J. Phys. Chem. B 109, 2245 (2005).
- [25] A. E. Maniadaki and G. Kopidakis, *Hydrogen on hybrid MoS₂/graphene nanostructures*, Phys. Status Solidi RRL. 10, 453 (2016)
- [26] C. Tsai, F. Abild-Pedersen, and J. K. Nørskov, *Tuning the MoS₂ Edge-Site Activity for Hydrogen Evolution via Support Interactions*, Nano Lett. 14, 1381 (2014).
- [27] S. Yu and W. Zheng, *Fundamental insights into the electronic structure of zigzag MoS₂ nanoribbons*, Phys. Chem. Chem. Phys. 18, 4675 (2016).

- [28] D. Cao, T. Shen, P. Liang, X. Chen, and H. Shu, *Role of Chemical Potential in Flake Shape and Edge Properties of Monolayer MoS₂*, J. Phys. Chem. C 119, 4294 (2015).
- [29] M. Chhowalla HS Shin, G. Eda, LJ Li, KP Loh and H. Zhang, *The chemistry of two-dimensional layered transition metal dichalcogenide nanosheets*, Nature Chemistry, Vol. 5 263-275, (2013)
- [30] Ralph W. G. Wyckoff, *Crustal structures, vol. I*, Interscience Publishers, Second Edition
- [31] A. H. Castro Neto, F. Guinea, N. M. R. Peres, K.S. Novoselov and A. K. Geim, *The electronic properties of graphene*, Rev. Mod. Phys. 81, 109-163 (2009)
- [32] V. Podzorov and M. E. Gershenson, *High-mobility field-effect transistors based on transition metal dichalcogenides*, Appl. Phys. Lett. 84, 3301, (2004)
- [33] K. K. Kam and B. A. Parkinson, *Detailed photocurrent spectroscopy of the semiconducting group – VI transition – metal dichalcogenides*, J. Phys. Chem. 86, 463-467 (1982)
- [34] M. Xu, T. Liang, M. Shi and H. Chen, *Graphene-like two-dimensional materials*, Chem. Rev., 113 (5), 3766–3798, (2013)
- [35] A. Kumar and P. K. Ahluwalia, *Electronic structure of transition metal dichalcogenides monolayers 1H-MX₂ (M=Mo, W; X=S, Se, Te) from ab initio theory: new direct gap semiconductors*, Eur. Phys. J. B 85, 186 (2012)
- [36] M. L. Tsai S. H. Su, J. K. Chang, C. H. Chen, C. I. Wu, L. J. Li, L. J. Chen and J.H He, *Monolayer MoS₂ Heterojunction Solar Cells*, ACS Nano, 8 (8), 8317–8322 (2014)
- [37] M. M. Furchi, A. Pospischil, F. Libisch, J. Burgdörfer and T. Mueller, *Photovoltaic Effect in Electrically Tunable van der Waals Heterojunction*, Nano Lett., 14, 4785–4791 (2014)
- [38] C. H. Lee, G.H Lee, A. M. van der Zande, W. Chen, Y. Li, M. Han, X. Cui, G. Arefe, C. Nuckolls, T. F. Heinz, J. Guo, J. Hone and P. Kim, *Atomically thin p-n junctions with van der Waals heterointerfaces*, Nat. Nanotechn. 9, 676–681 (2014)
- [39] M. A. Lukowski, A. S. Daniel, F. Meng, A. Forticaux, L. Li and S. Jin, *Enhanced Hydrogen Evolution Catalysis from Chemically Exfoliated Metallic MoS₂ Nanosheets*, J. Am. Chem. Soc. 135 (28), 10274–10277 (2013)
- [40] K. Iordanidou, M. Houssa, G. Poutrois, V. V. Afanasev and A. Stesmans, *Oxygen and hydroxyl adsorption on MS₂ (M=Mo, W, Hf) monolayers : a first – principles molecular dynamics study*, Phys. Status Solidi RRL 10 (11), 787-791 (2016)
- [41] K. Kalantar-Zadeh and J. Zhen Ou, *Biosensors based on Two Dimensional MoS₂*, ACS Sens., 1 (1), 5–16, (2016)

- [42] H. Wang, Z. Lu, S. Xu, D. Kong, J. J. Cha, G. Zheng, P. C. Hsu, K. Yan, D. Bradshaw, F. B. Prinz and Y. Cui, *Electrochemical tuning of vertically aligned MoS₂ nanofilms and its applications in improving hydrogen evolution reaction*, PNAS 110 (49), 19701-19706 (2013)
- [43] R. C. Vitoria, Y. Sayed-Ahmad-Baraza, M. Pelaez-Fernandez, R. Arenal, C. Bittencourt, C. P. Ewels and N. Tagmatarchis, *Functionalization of MoS₂ with 1,2 dithiolanes: toward donor – acceptor nanohybrids for energy conversion*, 2D Mater. Appl. 1, 13 (2017)
- [44] L. Majidi, P. Yasaei, R. E. Warburton, S. Fuladi, J. Cavin, X. Hu, Z. Hemmat, S. B. Cho, P. Abbasi, M. Vörös, L. Cheng, B. Sayahpour et.al, *New Class of Electrocatalysts Based on 2D Transition Metal Dichalcogenides in Ionic Liquid*, Adv. Mater. 31, 1804453 (2019)
- [45] S. Wu, Y. Zeng, X. Zeng, S. Wang, Y. Hu, W. Wang, S. Yin, G. Zhou, W. Jin, T. Ren, Z. Guo and J. Lu, *High – performance p – type MoS₂ field – effect transistor by toroidal – magnetic – field controlled oxygen plasma doping*, 2D Matter. 6, 025007 (2019)
- [46] J. Wu, M. Liu, K. Chatterjee, K. P. Hackenberg, J. Shen, X. Zou, Y. Yan, J. Gu, Y. Yang, J. Lou and P. M. Ajayan, *Exfoliated 2D Transition Metal Disulfides for Enhanced Electrocatalysis of Oxygen Evolution Reaction in Acidic Medium*, Adv. Mater. Interfaces 3, 1500669 (2016)
- [47] W. Chen, Y. Liu, Y. Li, J. Sun, Y. Qiu, C. Liu, G. Zhou and Y. Cui., *In Situ Electrochemically Derived Nanoporous Oxides from Transition Metal Dichalcogenides for Active Oxygen Evolution Catalysts*, Nano Lett. 16, 7588-7569 (2016)
- [48] M. Asadi, K. Kim, A. V. Addepalli, P. Abbasi, P. Yasaei, P. Phillips, A. Behranginia, J. M. Cerrato, R. Haasch, P. Zapol, B. Kumar, R. F. Klie, J. Abiade, L. A. Curtiss and A. Salehi-Khojin, *Nanostructured transition metal dichalcogenide electrocatalysts for CO₂ reduction in ionic liquid*, Science 353, 6298 (2016)
- [49] J. Yang and H. S. Shin, *Recent Advances in Layered Transition Metal Dichalcogenides for Hydrogen Evolution Reaction*, J. Mater. Chem. A 2, 5979-5985 (2014)
- [50] M. Asadi, B. Kumar, C. Liu, P. Phillips, P. Yasaei, A. Behranginia, P. Zapol, R. F. Klie, L. A. Curtis and A. Salehi-Khojin, *Cathode Based on Molybdenum Disulfide Nanoflakes for Lithium – Oxygen Batteries*, ACS Nano 10, 2, 2167-2175 (2016)
- [51] H. P. Komsa and A. V. Krasheninnikov, *Two – dimensional Transition Metal Dichalcogenide Alloys: Stability and Electronic Properties*, J. Phys. Chem. Lett. 3, 23, 3652-3656 (2012)
- [52] D. Dumcenco, D. Ovchinnikov, K. Marinov, P. Lazić, M. Gibertini, N. Marzari, O. L. Sanchez, Y. C. Kung, D. Krasnozov, M. W. Chen, S. Bertolazzi, P. Gillet, A. Fontcuberta i Morral, A. Radenovic and A. Kis, *Large – Area Epitaxial Monolayer MoS₂*, ACS Nano 9, 4, 4611-4620 (2015)

- [53] H. P. Komsa and A. V. Krasheninnikov, *Electronic structures and optical properties of realistic transition metal dichalcogenide heterostructures from first principles*, Phys. Rev. B 88, 085318 (2013)
- [54] R. Shidpour and M. Manteghian, *A density functional study of strong local magnetism creation on MoS₂ nanoribbon by sulfur vacancy*, Nanoscale 2, 1429-1435 (2010)
- [55] S. Susarla, A. Kutana, J. A. Hachtel, V. Kochat, A. Apte, R. Vajtai, J. C. Idrobo, B. I. Yakobson, C. S. Tiwary and P. M. Ajayan, *Quaternary 2D Transition Metal Dichalcogenides (TMDs) with Tunable Bandgap*, Adv. Mater. 29, 1702457 (2017)
- [56] Y. C. Lin, T. Björkman, H. P. Komsa, P. Y. Teng, C. H. Yeh, F. S. Huang, K. H. Lin, J. Jadcak, Y. S. Huang, P. W. Chiu, A. V. Krasheninnikov and K. Suenaga, *Three – fold rotational defects in two – dimensional transition metal dichalcogenides*, Nat. Commun. 6, 6736 (2015)
- [57] Y. Feldam, E. Wasserman, D. J. Srolovitz and R. Tenne, *High- rated, gas-phase growth of MoS₂ nested inorganic fullerenes and nanotubes*, Science 267,222 (1995)
- [58] X. Liu, T. Xu, X. Wu, Z. Zhang, J. Yu, H. Qiu, J. H. Hong, C. H. Jin, J. X. Li, X. R. Wang, L. T. Sun and W. Guo, *Top down fabrication of sub-nanometre semiconducting nanoribbons derived from molybdenum disulfide sheets*, Nat. Commun. 4, 1776 (2013)
- [59] H. Zhang, X. B. Li and L. M. Liu, *Tunable electronic and magnetic properties of WS₂ nanoribbons*, J. Appl. Phys. 114, 093710 (2013)
- [60] J. Lin, Z. Peng, G. Wang, D. Zakhidov, E. Larios, M. J. Yacaman and J. M. Tour, *Enhanced Electrocatalysis for Hydrogen Evolution Reaction from WS₂ Nanoribbons*, Adv. Energy Mater. 4, 1301875 (2014)
- [61] T. Wang, D. Gao, J. Zhuo, Prof. Z. Zhu, Prof. P. Papakonstantinou, Prof. Y. Li and Prof. M. Li, *Size – Dependent Enhancement of Electrocatalytic Oxygen – Reduction and Hydrogen – Evolution Performance of MoS₂ Particles*, Chem. Eur. J. 19, 11939-11948 (2013)
- [62] M. Asadi, B. Kumar, A. Behranginia, B. A. Rosen, A. Baskin, N. Reppin, D. Pisasale, P. Phillips, W. Zhu, R. Haasch, R. F. Klie, P. Král, J. Abiade and A. Slehi-Khojin, *Robust carbon dioxide reduction on molybdenum disulfide edges*, Nature Commun. 5, 4470 (2014)
- [63] N. Salami and A. A. Shokri, *Electronic properties of MoS₂ nanoribbons with disorder effects*, J. Phys. Chem. Sol. 90, 16-26 (2016)
- [64] A. A. Koós, P. Vancsó, G. Z. Magda, Z. Osváth, K. Kertész, G. Dobrik, C. Hwang, L. Tapasztó and L. Bíró, *STM study of the MoS₂ flakes grown on graphite: A model system for atomically clean 2D heterostructure interfaces*, Carbon 105, 408-415 (2016)
- [65] H. Rostami, R. Asgari and F. Guinea, *Edge modes in zigzag and armchair ribbons of monolayer MoS₂*, J. Phys.: Condensed Matter 28, 495001 (2016)

- [66] D.Davelou, G. Kopidakis, E. Kaxiras and I. N. Remediakis, Nanoribbon edges of transition – metal dichalcogenides : Stability and electronic properties, *Phys. Rev. B* 96, 165436 (2017)
- [67] C. Zhang, A. Johnson, C. L. Hsu, L. J. Li and C. K. Shih, *Direct Imaging of Band Profile in Single Layer MoS₂ on Graphite: Quasiparticle Energy Gap, Metallic Edge States and Edge Band Bending*, *Nano Lett.* 14, 2443-2447 (2014)
- [68] H. Pan and Y.W. Zhang, *Edge – dependent structural, electronic and magnetic properties of MoS₂ nanoribbons*, *J. Matter. Chem* 22, 7280 (2012)
- [69] J. V. Lauritsen, M. Nyberg, M. V. Bollinger, B. S. Clausen, H. Topsøe, K. W. Jacobsen, E. Lægsgaard, J. K. Nørskov and F. Besenbacher, *Chemistry of one – dimensional metallic edge states in MoS₂ nanoclusters*, *Nanotechnology* 14, 385-389 (2003)
- [70] P. Hohenberg and W. Kohn , *Inhomogeneous electron gas*, *Phys. Rev.* 136, 864, (1964)
- [71] W. Kohn and L. J. Sham, *Self – consistent equations including exchange and correlation effects*, *Phys. Rev.* 140, 1133, (1965)
- [72] J. P. Perdew, K. Burke, and M. Ernzerhof, *Generalized Gradient Approximation Made Simple*, *Phys. Rev. Lett.* 77, 3865, (1996).
- [73] Lauri Nykanen, *Computational studies of carbon chemistry on transition metal surfaces*, University of Jyväskylä, Finland (2012)
- [74] J. Enkovaara, C. Rostgaard, J. J. Mortensen, J.Chen, M. Dulak, L. Ferrighi, J. Gavnholt, C. Glinsvad, V. Haikola, H. Hansen, H. H. Kristoffersen, M. Kuisma, A. H. Larsen, L. Lehtovaara, M. Ljungberg, O. L. Acevedo, P. Moses, J. Ojanen, T. Olsen, and K. W. Jacobsen, *Electronic structure calculations with GPAW: a real-space implementation of the projector augmented-wave method*, *J. Phys. Condens. Matter* 22, 253202, (2010)
- [75] P. E. Blöchl, *Projector augmented-wave method*, *Phys. Rev. B* 50, 17953, (1994)
- [76] https://wiki.fysik.dtu.dk/gpaw/introduction_to_paw.html (retrieved June. 10, 2019)
- [77] The free software “Atomic Simulation Environment” can be found at:
<https://wiki.fysik.dtu.dk/ase/>
- [78] E. N. Oikonomou, *Solid State Physics*, Crete University Press, Heraklion, 249-271, (2010)
- [79] A. N. Andriotis, *Computational Physics Second Edition*, Athens, , 244-253 (2016)
- [80] E. Kaxiras, *Atomic and Electronic Structure of Solids*, Cambridge University Press, New York, , 121-139 (2003)
- [81] S. Fang, R. K. Defo, S. N. Shirodkar, S. Lieu, G. A. Tritsarlis and E. Kaxiras, *Ab initio tight – binding Hamiltonian for transition metal dichalcogenides*, *Phys. Rev. B* 92, 205108 (2015)
- [82] J. C. Slater and G. F. Koster, *Simplified LCAO Method for the Periodic Potential Problem*, *Phys. Rev.* 94, 6 (1954)

- [83] W. A. Harisson, *Electronic structure and properties of solids*, Dover Publications INC, New York, 46-54, (1989)
- [84] Ralph W. G. Wyckoff, *Crustal structures, vol.I*, Interscience Publishers, Second Edition
- [85] https://docs.scipy.org/doc/scipy/reference/generated/scipy.optimize.curve_fit.html (accessed Sept 20, 2019)
- [86] Data from www.webelements.com (accessed Nov 17, 2016)
- [87] D. Y. Qiu, F. H. da Jornada, and S. G. Louie, *Optical Spectrum of MoS₂: Many-Body Effects and Diversity of Exciton States*, Phys. Rev. Lett. 111, 216805 (2013)
- [88] A. Ramasubramaniam, *Large excitonic effects in monolayers of molybdenum and tungsten dichalcogenides*, Phys. Rev. B 86, 115409 (2012).
- [89] G. R. Bhimanapati, Z. Lin, V. Meunier, Y. Jung, J. Cha, S. Das, D. Xiao, Y. Son, M. S. Strano, V. R. Cooper, L. Liang, S. G. Louie, E. Ringe, W. Zhou, S. S. Kim, R. R. Naik, B. G. Sumpter, H. Terrones, F. Xia, Y. Wang, J. Zhu, D. Akinwande, N. Alem, J. A. Schuller, R. E. Schaak, M. Terrones, and J. A. Robinson, *Recent Advances in Two-Dimensional Materials beyond Graphene*, ACS Nano 9, 11509 (2015).
- [90] D. Y. Qiu, F. H. da Jornada, and S. G. Louie, *Screening and many-body effects in two-dimensional crystals: Monolayer MoS₂*, Phys. Rev. B 93, 235435 (2016).
- [91] L. S. Byskov, J. K. Nørskov, B. S. Clausen, and H. Topsøe, *Edge termination of MoS₂ and CoMoS catalyst particles*, Cat. Lett. 64, 95 (2000).
- [92] P. Cui, J.-H. Choi, W. Chen, J. Zeng, C.-K. Shih, Z. Li, and Z. Zhang, *Contrasting Structural Reconstructions, Electronic Properties, and Magnetic Orderings along Different Edges of Zigzag Transition Metal Dichalcogenide Nanoribbons*, Nano Lett. 17, 1097 (2017).
- [93] G. D. Barmparis and I. N. Remediakis, *Dependence on CO adsorption of shapes of multifaceted gold nanoparticles: A density functional theory*, Phys. Rev. B 86, 085457 (2012).
- [94] G. D. Barmparis, Z. Lodziana, N. Lopez, and I. N. Remediakis, *Nanoparticle shapes by using Wulff constructions and first-principle calculations*, Beilstein J. Nanotechnol. 6, 361 (2015).
- [95] W. Shockley, *On the surface states associated with a periodic potential*, Phys. Rev., 56:317-323 (1939)
- [96] I. Tamm, *Über eine mögliche Art der Elektronenbindung an Kristalloberflächen*. Zeitschrift für Physik , 76(11), 849-850 (1932)
- [97] A. Michaelides and M. Scheffler, *An introduction to the Theory of Crystalline Elemental Solids and their Surfaces. In Surface and Interface Science*. Wiley – VCH Verlag GmbH & Co. KGaA, pp 13-72 (2014)

- [98] B. Kollmann, Shockley Surface states calculated within Density Functional Theory, Master Thesis, Universität Graz (2014)
- [99] L. Qi, Y. Wang, L. Shen and Y. Wu, *Chemisorption-induced-n-doping of MoS₂ by oxygen*, Applied Phys. Lett, 108, 063103 (2016)
- [100] Santosh KC, R. C. Longo, R. M. Wallace and K. Cho, *Surface oxidation and kinetics on MoS₂ monolayer*, J. Appl. Phys. 117, 135301 (2015)
- [101] C. Ataca, H. Şahin and S. Ciraci, *Stable Single-Layer MX₂ Transition – Metal Oxides and Dichalcogenides in a Honeycomb – Like Structure*, J. Phys. Chem. 116, 8983-8999 (2012)
- [102] C. Ataca, H. Şahin, E. Aktürk and S. Ciraci, *Mechanical and Electronic Properties of MoS₂ Nanoribbons and their Defects*, J. Phys. Chem 115, 3934-3941 (2011)
- [103] L. S. Byskov et al., *Edge termination of MoS₂ and CoMoS catalyst particles*, Catalysis Letters 64, 95-99 (2000)
- [104] H. Liu, N. Han and J. Zhao, *Atomistic insight into the oxidation of monolayer transition metal dichalcogenides: from structure to electronic properties*, RSC Adv. 5, 17572-17581 (2015)
- [105] J. Gao, B. Li, J. Tan, P. Chow, T. M. Lu and N. Koratkar., *Aging of Transition Metal Dichalcogenide Monolayers*, ACS Nano 10, 2, 2628-2635 (2016)
- [106] J. Lu, A. Carvalho, X. K. Chan, H. Liu, B. Liu, E. S. Tok, K. P. Loh, A. H. Castro Neto and C. H. Sow, *Atomic healing of defects in transition metal dichalcogenides*, Nano Lett. 15, 5, 3524-3532 (2015)
- [107] W. Park, J. Park, J. Jang, H. Lee, H. Jeong, K. Cho, S. Hong and T. Lee, *Oxygen environmental and passivation effects on molybdenum disulfide field effect transistors*, Nanotechnology 24, 095202 (2013)
- [108] M. R. Islam, N. Kang, U. Bhanu, H. P. Paudel, M. Erementchouk, L. Tetard, M. N. Leuenberger and S. I. Khondaker, *Tuning the electrical property via defect engineering of single layer MoS₂ by oxygen plasma*, Nanoscale 6, 10033 (2014)
- [109] X. Chia, A. Y. Sheng Eng, A. Ambrosi, S. M. Tan and M. Pumera, *Electrochemistry of Nanostructured Layered Transition – Metal Dichalcogenides*, Chem. Rev. 115, 11941-11966 (2015)
- [110] M. Calligaris, *Stereochemical Aspects of Sulfoxides and Metal Sulfoxide Complexes*, CCACAA 72 (2-3), 147-169 (1999)
- [111] W. J. Orville – Thomas, *A Bond – Order/ Bond – Length Relation for Oxygen – Oxygen Bonds*, J. Mol. Spectr. 3, 588-591 (1958)